Cell Stem Cell

Article

A mitochondrial NADPH-cholesterol axis regulates extracellular vesicle biogenesis to support hematopoietic stem cell fate

Graphical abstract

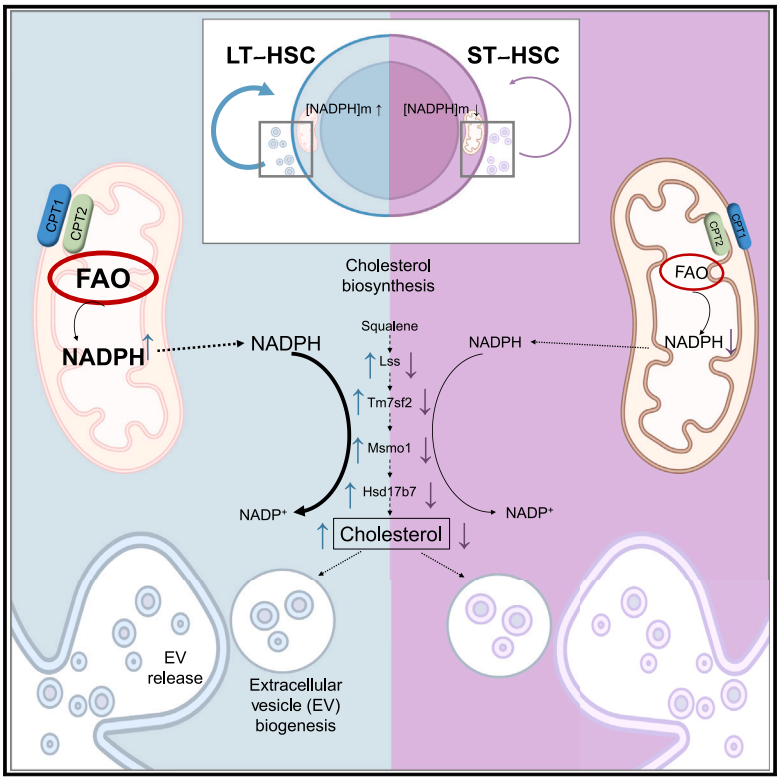

Highlights

- HSCs have high mitochondrial NADPH that fuels cholesterol biosynthesis
- High NADPH and cholesterol synthesis in HSCs are dependent on FAO
- The NADPH-cholesterol axis supports proper HSC self-renewal and homeostasis
- HSC cholesterol levels impact autocrine EV signaling

Authors

Massimo Bonora, Claudia Morganti, Nick van Gastel, ..., Chiara Romualdi, David T. Scadden, Keisuke Ito

Correspondence

keisuke.ito@einsteinmed.edu

In brief

Ito et al. investigate the mechanism by which mitochondrial metabolism controls hematopoietic stem cell (HSC) fate. They reveal that FAO (fatty acid oxidation)-generated NADPH fuels cholesterol biosynthesis in HSCs. A mitochondrial NADPH-cholesterol axis controls the biogenesis of extracellular vesicles that is required for proper HSC self-renewal and hematopoietic homeostasis.

Bonora et al., 2024, Cell Stem Cell *31*, 359–377
March 7, 2024
https://doi.org/10.1016/j.stem.2024.02.004

CellPress

Cell Stem Cell

CellPress
OPEN ACCESS

Article

A mitochondrial NADPH-cholesterol axis regulates extracellular vesicle biogenesis to support hematopoietic stem cell fate

Massimo Bonora,[1,2,3,23] Claudia Morganti,[1,2,3,23] Nick van Gastel,[4,5,6,23] Kyoko Ito,[1,2,3] Enrica Calura,[7] Ilaria Zanolla,[8] Letizia Ferroni,[9] Yang Zhang,[10] Yookyung Jung,[10,11,12] Gabriele Sales,[7] Paolo Martini,[13] Takahisa Nakamura,[14,15,16] Francesco Massimo Lasorsa,[17] Toren Finkel,[18] Charles P. Lin,[19] Barbara Zavan,[9,20,21] Paolo Pinton,[8,9,20] Irene Georgakoudi,[10] Chiara Romualdi,[7] David T. Scadden,[4,5] and Keisuke Ito[1,2,3,22,24,*]

[1]Ruth L. and David S. Gottesman Institute for Stem Cell and Regenerative Medicine Research, Albert Einstein College of Medicine, 1300 Morris Park Avenue, Bronx, NY 10461, USA
[2]Department of Cell Biology, Albert Einstein College of Medicine, Bronx, NY 10461, USA
[3]Departments of Oncology and Medicine, Albert Einstein College of Medicine-Montefiore Health System, Bronx, NY 10461, USA
[4]Department of Stem Cell and Regenerative Biology, Harvard Stem Cell Institute, Harvard University, Cambridge, MA, USA
[5]Center for Regenerative Medicine, Massachusetts General Hospital, Boston, MA, USA
[6]de Duve Institute, UCLouvain, 1200 Brussels, Belgium
[7]Department of Biology, University of Padova, 35121 Padua, Italy
[8]Department of Medical Sciences, University of Ferrara, 44121 Ferrara, Italy
[9]Maria Cecilia Hospital, GVM Care & Research, Cotignola, 48033 Ravenna, Italy
[10]Department of Biomedical Engineering, Tufts University, 4 Colby St, Medford, MA 02155, USA
[11]Department of Pathology, Albert Einstein College of Medicine, Bronx, NY 10461, USA
[12]Gruss-Lipper Biophotonics Center, Albert Einstein College of Medicine, Bronx, NY 10461, USA
[13]Department of Molecular and Translational Medicine, University of Brescia, 25121 Brescia, Italy
[14]Divisions of Endocrinology and Developmental Biology, Cincinnati Children's Hospital Medical Center, Cincinnati, OH 45229, USA
[15]Department of Pediatrics, University of Cincinnati College of Medicine, Cincinnati, OH 45229, USA
[16]Department of Metabolic Bioregulation, Institute of Development, Aging and Cancer, Tohoku University, Sendai 980-8575, Japan
[17]Department of Biosciences Biotechnologies and Environment University of Bari and Institute of Biomembranes Bioenergetics and Molecular Biotechnologies, Consiglio Nazionale delle Ricerche, 70125 Bari, Italy
[18]Aging Institute and Department of Medicine, University of Pittsburgh School of Medicine/University of Pittsburgh Medical Center, Pittsburgh, PA 15261, USA
[19]Center for Systems Biology and Wellman Center for Photomedicine, Massachusetts General Hospital, Harvard Medical School, Boston, MA 02114, USA
[20]Laboratory for Technologies of Advanced Therapies (LTTA), University of Ferrara, 44121 Ferrara, Italy
[21]Translational Medicine Department, University of Ferrara, 44121 Ferrara, Italy
[22]Montefiore Einstein Comprehensive Cancer Center and Diabetes Research Center, Albert Einstein College of Medicine, Bronx, NY 10461, USA
[23]These authors contributed equally
[24]Lead contact
*Correspondence: keisuke.ito@einsteinmed.edu
https://doi.org/10.1016/j.stem.2024.02.004

SUMMARY

Mitochondrial fatty acid oxidation (FAO) is essential for hematopoietic stem cell (HSC) self-renewal; however, the mechanism by which mitochondrial metabolism controls HSC fate remains unknown. Here, we show that within the hematopoietic lineage, HSCs have the largest mitochondrial NADPH pools, which are required for proper HSC cell fate and homeostasis. Bioinformatic analysis of the HSC transcriptome, biochemical assays, and genetic inactivation of FAO all indicate that FAO-generated NADPH fuels cholesterol synthesis in HSCs. Interference with FAO disturbs the segregation of mitochondrial NADPH toward corresponding daughter cells upon single HSC division. Importantly, we have found that the FAO-NADPH-cholesterol axis drives extracellular vesicle (EV) biogenesis and release in HSCs, while inhibition of EV signaling impairs HSC self-renewal. These data reveal the existence of a mitochondrial NADPH-cholesterol axis for EV biogenesis that is required for hematopoietic homeostasis and highlight the non-stochastic nature of HSC fate determination.

INTRODUCTION

Cellular metabolism in hematopoietic stem cells (HSCs) has recently become the focus of intense research interest.[1] Mitochondria participate in multiple cellular functions, including regulation of cell metabolism, through the tricarboxylic acid (TCA) cycle and the respiratory chain.[2,3] In this multifaceted biochemical process, the 4 respiratory complexes in the inner mitochondrial membrane transport electrons from nicotinamide adenine dinucleotide (NADH)/flavin adenine dinucleotide ($FADH_2$) to oxygen in an electron transport chain (ETC), which generates a proton gradient across the mitochondrial membrane.

Early evidence indicated that HSC mitochondria are functionally dispensable and activated only when commitment is demanded.[4,5] However, deeper investigation into HSC function has revealed its dependence on mitochondrial fatty acid oxidation (FAO)—the catabolism of fatty acids in the mitochondrial matrix that feeds the TCA cycle[6,7]—or the expression of subunits of respiratory complex III (*Uqcrfs1*) or complex II (*SdhD*).[8,9] Recent research has also highlighted the necessity of using a dye-independent method to improve the accuracy of assessment of HSC mitochondria,[10,11] and multiple studies have since confirmed that mitochondrial content and membrane potential in hematopoietic stem and progenitor cells (HSPCs) has been consistently underestimated in a manner that can correlate with assessments of stem cell function.[10–13]

FAO also produces metabolites required to re-model the lipid landscape of HSCs. Some lipid species such as sphingolipids, glycolipids, and sterols are known to contribute to hematopoiesis.[14] Genetic loss of cholesterol efflux transporter has been shown to regulate mobilization[15,16] and expansion[17] of the HSPC pool by enhancing the signaling for critical cytokines (e.g., interleukin-3[IL-3]/granulocyte-macrophage colony-stimulating factor [GM-CSF] receptor).[18]

These observations imply the possibility that mitochondria play previously unappreciated roles in HSC biology. How exactly mitochondrial respiration and FAO steer HSC fate decisions, however, remains unclear.

RESULTS

HSCs have high mitochondrial NADPH

FAO feeds mitochondrial metabolism, which reduces NADH, $FADH_2$, and nicotinamide adenine dinucleotide phosphate (NADPH) to drive redox reactions in the ETC and support multiple biosynthetic processes. We have observed that HSCs have limited expression of complex I while relying on complex II to support ETC activity,[19,20] supporting the idea that HSCs accumulate high levels of reduced cofactors.

Taking advantage of these spectral properties of NAD(P)H, we observed that NAD(P)H autofluorescence appeared brighter in $CD150^+CD48^-CD135^-Lin^-Sca\text{-}1^+c\text{-}Kit^+$ cells (hereafter, HSCs) and displayed a dimming trend with hematopoietic differentiation (Figures 1A and S1A). Fully differentiated myeloid cells apparently deviate from this trend. As these populations dramatically vary in size[21] (Figures S1B and S1C), we corrected NAD(P)H autofluorescence for forward scatter area (FSC-A, used as reporter of cell size, Figure S1B). The resulting readout of NAD(P)H density per cell (labeled as nNAD(P)H) confirms the dimming trend of NAD(P)H levels with differentiation, which reaches lower levels in fully differentiated cells (Figure S1D).

Higher autofluorescence was observed in more primitive $CD34^-$ HSCs compared to $CD34^+$ HSCs (Figures 1B and 1C), and endothelial protein C receptor (EPCR) positivity[22–24] correlated with higher NAD(P)H levels in both HSCs and $CD34^-$ HSCs (Figures S1E).

Co-staining with the mitochondrial marker tetramethylrhodamine, methyl ester (TMRM) confirmed the mitochondrial localization of NAD(P)H (Figure 1C). To assess whether the high mitochondrial NAD(P)H levels in primitive HSCs were mainly due to NADH or NADPH pools, we leverage the differing sensitivities of the NAD(P)H pool to the mitochondrial uncoupler carbonyl cyanide-p-trifluoromethoxyphenylhydrazone (FCCP), the oxidizer H_2O_2, and the ETC inhibitor rotenone.[25] This analysis suggests that $CD34^-$ HSCs have a significant enrichment of mitochondrial NADPH compared to $CD34^+$ HSCs (Figures S1J and S1L).

Fluorescence lifetime imaging (FLIM) has enabled the *in situ* determination of NAD(P)H lifetime pools in living cells, thanks to the different fluorescence time decay of NADPH and NADH.[25–27] FLIM assay confirmed that $CD34^-$ HSC mitochondria display a higher NADPH/NADH ratio than the mitochondria of $CD34^+$ HSCs (Figure S1M). Further, NADPH- and NADH-dependent bioluminescent enzymatic systems (Figures 1E and 1F) corroborated that cytosolic NADPH ($[NADPH]_c$) was comparable (Figure S1N), and no significant differences were observed in either mitochondrial or cytosolic NADH levels (Figures 1G and S1O).

Collectively, these data show that long-term HSCs ($CD34^-$ and/or $EPCR^+$) have significantly higher levels of mitochondrial NADPH than $CD34^+$ HSCs (and/or $EPCR^-$).

NAD(P)H autofluorescence marks HSC capacity

To assess the association between NADPH and HSC functions, $CD34^-$ HSCs were divided into two fractions reflecting high and low levels of NAD(P)H (Figures 1H and S2A and STAR Methods). Approximately 60% of $CD34^-$ HSCs were included in the $NAD(P)H^{Hi}$ gate, and a downward trend in NAD(P)H levels correlated with hematopoietic differentiation (Figure S2B). The percentage of $NAD(P)H^{Hi}$ cells was significantly higher in $EPCR^+$ HSCs or $EPCR^+CD34^-$ HSCs compared to $EPCR^-$ (Figures S2C). In agreement, $NAD(P)H^{Hi}$ bone marrow mononuclear cells (BMMNCs) displayed higher percentages of $cKit^+Sca\text{-}1^+$, $CD150^+CD48^-$, and $EPCR^+$ cells compared to the $NAD(P)H^{Lo}$ counterpart (Figures S2D).

Both $NAD(P)H^{Hi}$ and $NAD(P)H^{Lo}$ $CD34^-$ HSCs are quiescent as the two populations displayed no significant differences in the timing of first division (Figure S2E) or positivity for the proliferation marker ki67 (Figure S2F) or in the G0 fraction determined by Pyronin Y (Figure S2G). Interestingly, active (Pyronin Y^+) HSCs displayed a moderate reduction in NAD(P)H autofluorescence when compared to dormant (Pyronin Y^-) HSCs (Figure S2H). When HSCs are forced to exit quiescence by *in vivo* stimulation with pI:pC, we observed a reduction in NAD(P)H autofluorescence (Figure S2I), possibly reflecting the stimulation in mitochondrial maturation previously reported.[28]

Neither features of mitochondrial morphology such as volume, elongation, compactness, or ultrastructure (cristae content or

CellPress
OPEN ACCESS

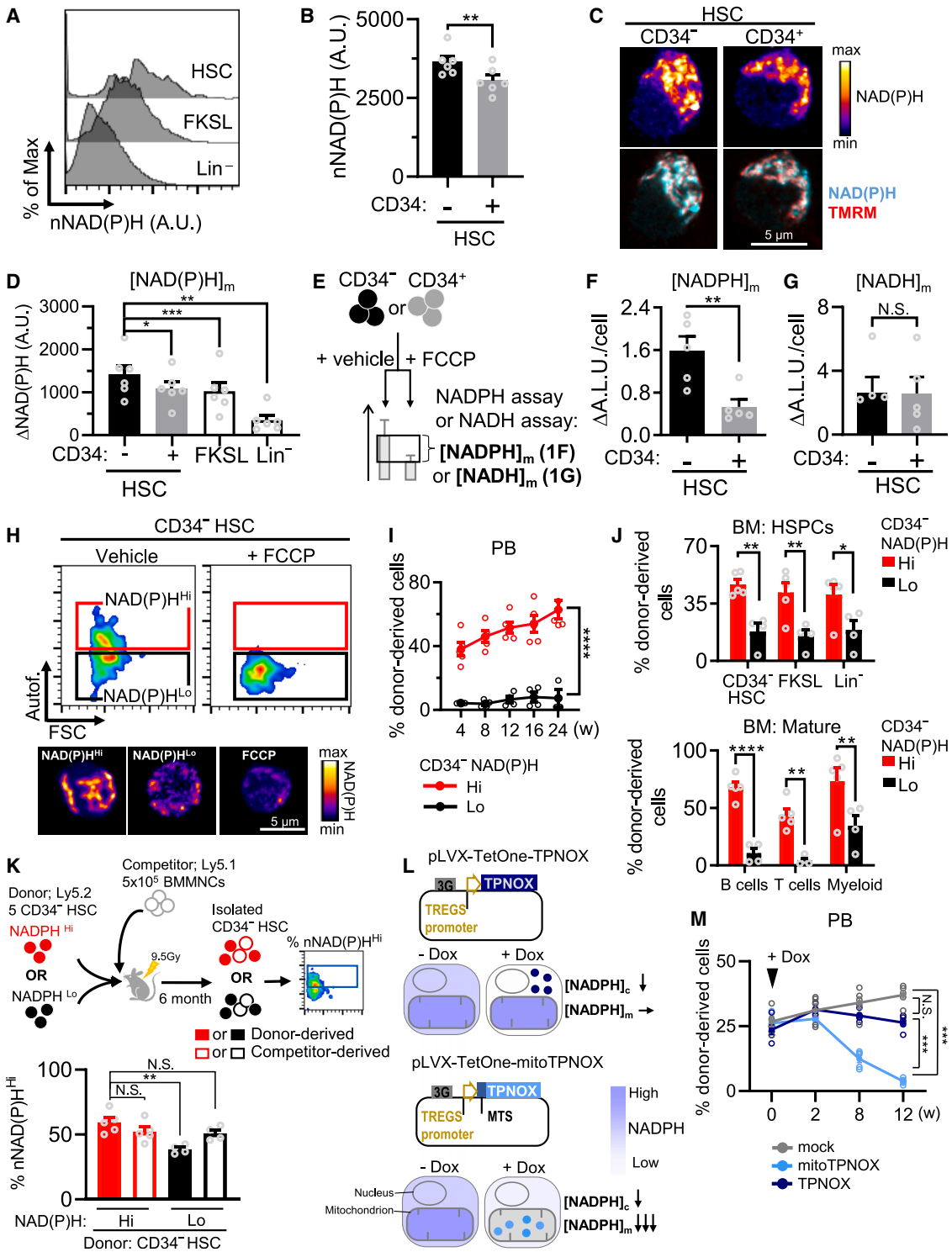

Figure 1. Mitochondrial NADPH levels mark stem cell capacity

(A) Flow cytometric histogram of the normalized NAD(P)H autofluorescence in HSCs, FKSL, and Lin⁻ cells (also see Figure S1A).

(B) Normalized NAD(P)H autofluorescence levels in CD34⁻ and CD34⁺ HSCs.

(C) Fluorescence microscopy images of NAD(P)H autofluorescence (top) and co-localization with the mitochondrial marker TMRM (bottom) obtained from CD34⁻ and CD34⁺ HSCs. Scale bar, 5µm.

(D) Mitochondrial NAD(P)H determined as the difference of NAD(P)H autofluorescence after exposure to FCCP 1 µM in the HSPC populations investigated.

© Experimental design for the enzymatic determination of mitochondrial NADPH and NADH. Sorted CD34⁻ or CD34⁺ HSCs were exposed *in vitro* to FCCP 1 µM to dissipate mitochondrial NAD(P)H.

(legend continued on next page)

morphology) nor reactive oxygen species (ROS) production were found to be altered in NAD(P)H^{Hi} versus NAD(P)H^{Lo} HSCs (Figures S2J–S2L), indicating that low levels of NAD(P)H are not dependent on the extra physiologic oxygen shock/stress induced in HSCs during isolation from bone marrow.[29]

In vitro long-term culture-initiating cell (LTC-IC) capacity was enriched in the NAD(P)H^{Hi} fraction (Figure S2M). In competitive bone marrow transplantation (BMT) settings, NAD(P)H^{Hi} CD34$^-$ HSCs exhibited higher reconstitution capacity compared to NAD(P)H^{Lo} CD34$^-$ HSCs (Figure 1I). NAD(P)H^{Hi} cells gave rise to higher levels of chimerism in HSPCs and Lin$^-$ cells as well as mature cells without lineage bias (B, T, and myeloid cells) (Figure 1J). Taken together, these results suggest that high NAD(P)H levels as measured by autofluorescence can serve as a marker for HSC capacity. Further, CD34$^-$ HSCs derived from NAD(P)H^{Hi} donors maintained a level of NAD(P)H autofluorescence comparable to that of competitor HSCs. In contrast, CD34$^-$ HSCs derived from NAD(P)H^{Lo} donors had much lower NAD(P)H levels when compared to both NAD(P)H^{Hi}-derived HSCs or competitor HSCs (Figure 1K). This indicates that NAD(P)H^{Lo} HSCs are defective in their reconstitution potential as well in the capacity to generate their physiological NAD(P)H pool.

To confirm the compartmentalization of NADPH, untargeted triphosphopyridine nucleotide oxidase (TPNOX), which decreases cytosolic NADPH, or mitochondria-targeted TPNOX (mitoTPNOX), which specifically consumes intra-mitochondrial NADPH, was utilized to manipulate cellular NADPH levels, a system under the control of the doxycycline (Dox)-inducible promoter[30] (Figures 1L, S2N, and S2O). Both TPNOX and mitoTPNOX decreased colony-replating capacity after long-term culture (Figure S2N, left). Critically, mitoTPNOX significantly decreased LTC-IC capacity *in vitro* and mitochondrial NAD(P)H autofluorescence (Figures S2N, right and S2O) to a much greater extent than TPNOX, suggesting that mitochondrial NADPH is critical to regulate HSC function. We thus tested *in vivo* expression of mitoTPNOX in a transplantation setting, where it was induced with Dox 3 weeks after BMT. The mitoTPNOX, but not TPNOX, reduced hematopoietic contributions of donor cells from 4 weeks after induction, while no significant changes in chimerism were found 2 weeks after induction in either case (Figure 1M). These data further support the important roles played by mitochondrial NADPH in hematopoietic homeostasis.

Mitochondrial NADPH segregation controls HSC fate determination

We next measured the kinetics of mitochondrial NAD(P)H levels in HSCs during cell division *in vitro*. Single CD34$^-$ HSCs were cultured and visually tracked until their first division. Corresponding daughter cells were stained with TMRM to perform 3D quantitation of NAD(P)H per single mitochondria (Figure 2A). We used a statistical approach to determine symmetric or asymmetric distribution of mitochondria between corresponding daughters (Figures 2A and S3A and STAR methods). With this strategy, 33% of divisions were labeled as asymmetric divisions, 36% as symmetric high, and the remaining 31% as symmetric low (Figure 2B), proportions similar to those obtained by paired daughter cell assays.[6,7]

We speculated that mitochondria can be asymmetrically inherited by daughter cells during HSC mitosis. NAD(P)H^{Hi} CD34$^-$ HSCs were isolated and subjected to cell-tracer staining followed by quantitative live imaging to track NAD(P)H inheritance during division. First division occurs at ~38 h from isolation (Figures S3B), consistent with cumulative division frequency analysis (Figures S2E). We observed that daughter cells can exhibit either the same NAD(P)H level as the mother or a significantly lower NAD(P)H level, but no daughter received a higher NAD(P)H level than its related mother cell (Figure 2C). We classified three distinct outputs of cell division (Figures 2D and S3C): a symmetric high where the two daughters have NAD(P)H comparable to the mother (41.5%); a symmetric low, with both daughters having lower NAD(P)H than the mother (28%); and an asymmetric output, where the daughters have different NAD(P)H levels (30.5%). The ratio of NAD(P)H intensity between two daughters confirmed the distribution pattern of NAD(P)H in those divisions' outputs determined as in Figure 2B (Figure S3D). A stochastic-segregation mitochondria during division should lead to cases of asymmetric segregation where one daughter cell has higher NADP(P)H than the mother cell. Critically, none of the daughter cells (236 cells) exhibited higher NAD(P)H than the mother at a level of statistical significance (Figures 2C and 2D), supporting the notion that asymmetry in NAD(P)H levels between corresponding daughter cells is the result of a regulated/non-stochastic process.

To further understand the significance of different levels of NADPH inherited by HSCs, we isolated daughter after first

(F and G) Enzymatic determination of levels of mitochondrial NADPH (F) and NADH (G) in CD34$^-$ and CD34$^+$ HSCs.
(H) Gating strategy to define NAD(P)H^{Hi} (red box) and NAD(P)H^{Lo} (black box) CD34$^-$ HSCs. Images of NAD(P)H autofluorescence of NAD(P)H^{Hi} CD34$^-$ HSCs, NAD(P)H^{Lo} CD34$^-$ HSCs, or FCCP-exposed CD34$^-$ HSCs are also shown (bottom). Scale bar, 5μm.
(I) Hematopoietic contribution of donor cells in peripheral blood of recipient mice during competitive BMT. Five NAD(P)H^{Hi} or NAD(P)H^{Lo} CD34$^-$ HSCs were isolated and then transplanted to the irradiated recipient mice with 4.0 × 10^5 competitor bone marrow mononuclear cells (BMMNCs).
(J) Percentages of donor-derived cells in the indicate fractions of the bone marrow of the recipient mice 6 months after BMT.
(K) Schematic representation (top) and quantitation (bottom) of the percentage of nNAD(P)H^{Hi} cells in donor-derived (filled bars) and competitor-derived (open bars) CD34$^-$ HSCs, 6 months after BMT.
(L) Schematic representation of the plasmid encoding for tetracycline (TET)-inducible expression of TPNOX or mitoTPNOX and their effect on cytoplasmic or mitochondrial NADPH after the induction with doxycycline (Dox).
(M) *In vivo* repopulation capacity of mitoTPNOX-infected HSPCs. 1,000 KSL (Ly5.2) infected with mitoTPNOX (light blue), TPNOX (dark blue), or empty vector (gray) was transplanted into the irradiated recipient mice (Ly5.1) with competitor cells (4.0 × 10^5 BMMNCs). Percentage of donor-derived cells in the peripheral blood the indicated weeks after Dox induction (black arrow) were shown. HSCs, Lin$^-$Sca-1$^+$c-Kit$^+$CD135$^-$CD150$^+$CD48$^-$; KSL, c-Kit$^+$Sca-1$^+$Lin$^-$; FKSL, CD135$^-$c-Kit$^+$Sca-1$^+$Lin$^-$; A.U., arbitrary unit; A.L.u., arbitrary luminescent units; MTS, mitochondrial targeting sequence; PB, peripheral blood; w, week. Bar graphs represent means ± SEM, circles represent each replicate. (B), (F), and (G): Student's paired t test. (I), (J), and (M): two-way ANOVA with Sidak's multiple comparison test. (K): one-way ANOVA with Dunnet's multiple comparison test. ****, $p < 0.0001$; ***, $0.0001 \leq p < 0.001$; **, $0.001 \leq p < 0.01$; *, $0.01 \leq p < 0.05$; N.S., not significant, $p \geq 0.05$. See also Figures S1 and S2.

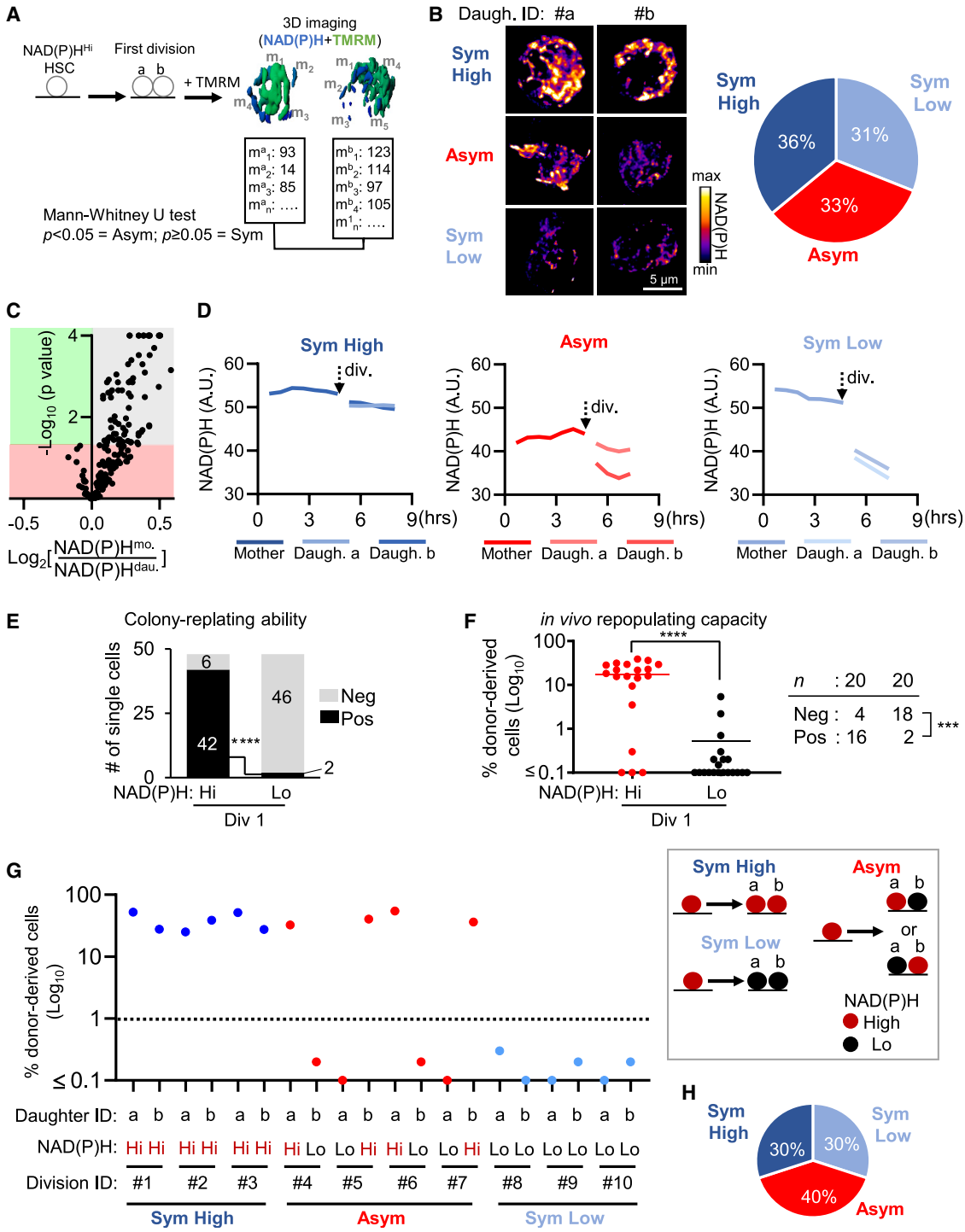

Figure 2. Mitochondrial NADPH levels mark HSC fate determination

(A) Experimental strategy for the determination of symmetric or asymmetric segregation of mitochondrial NAD(P)H after first division in the cultured CD34⁻ HSCs. Fluorescence microscopic analysis was performed to determine NAD(P)H autofluorescence intensity in the individual mitochondrion of each daughter cell. NAD(P)H intensities were subsequently compared between paired daughter cells by Mann-Whitney U test. (also see Figure S3A).

(B) Proportion of distribution of mitochondrial NAD(P)H after first division of the cultured CD34⁻ HSCs (n = 36, right). Images of NAD(P)H of the corresponding daughter cells are also shown (left). Scale bar, 5μm.

(C and D) Determination of NAD(P)H segregation by live imaging.

(legend continued on next page)

division that displayed NAD(P)H^{Hi} or NAD(P)H^{Lo} cells and performed functional assays. After first division (Div 1), the self-renewal capacity, measured by single-cell colony-replating ability after *in vitro* long-term culture (Figure 2E) and reconstitution capacity after single-cell transplantation (Figure 2F), was significantly enriched in NAD(P)H^{Hi} cells, supporting that NAD(P)H^{Hi} acts as a marker of HSC capacity during HSC division.

In vivo paired daughter cell (PDC) assay can determine the division patterns of HSCs retrospectively by assessing the reconstitution capacity of each daughter cell (Figure 2G).[6,7,31] PDC assay revealed that daughter cells receiving symmetrically high NAD(P)H levels exhibited significant reconstitution potential, indicative of a symmetric division (30%). Division where NAD(P)H levels differ from between the two daughters also returned asymmetric reconstitution (40%). Ultimately, daughters that shared a low NAD(P)H level also shared a defective repopulation capacity (symmetric commitment, 30%). The percentage of the division patterns calculated by PDC assay overlapped with those obtained by live imaging of NAD(P)H (Figure 2H). Overall, these confirmed that NAD(P)H segregation upon Div 1 corresponds to the segregation of HSC function and their fate determination.

The intensity of TMRM was comparable in both NAD(P)H^{Hi} or NAD(P)H^{Lo} daughters, suggesting no major alterations in their respiration (Figure S3E) and corroborating the initial hypothesis that NAD(P)H levels in HSCs depend on FAO. Rate-limiting steps in FAO are represented by carnitine O-palmitoyltransferases 1 and 2 (Cpt1 and Cpt2).[32] HSC daughters who retained NAD(P)H^{Hi} (Div 1) not only had higher expression of *Cpt1a* compared to NAD(P)H^{Lo} but also had no observed alterations of gene expression for *Ndufv1*, the subunit of respiratory complex I responsible for NADH binding (Figure S3F). Most strikingly, *Cpt1a* enabled us to clearly distinguish NAD(P)H^{Hi} cells from NAD(P)H^{Lo} cells at a single-cell level (Figure S3F). This observation indicates that during HSC division, daughter cells can differentially segregate their FAO capacity, which ultimately results in the asymmetry of NAD(P)H levels.

NADPH sustains cholesterol biosynthesis in HSCs

To identify biochemical pathways supported by NADPH in HSCs, we used 3 public datasets to investigate gene expression variation between mouse CD34$^-$ and CD34$^+$ HSCs[33–35] (Figures S4A and S4B). We identified 77 NADPH-related pathways and compared their gene expression levels by Reactome database (Figure 3A). Then we used the protein-metabolite Graphite networks[36] to retain NADPH metabolites in pathway-derived graphs. The resulting list of the NADPH-dependent pathways enriched in HSCs included the detoxification of ROS and linoleic acid metabolism, pathways already considered relevant for HSC maintenance (Figure 3B).

We selected the cholesterol biosynthesis pathway as that of greatest interest.[15,18,37] Four genes involved in this pathway (*Lss*, *Tm7sf2*, *Msmo1*, and *Hsd17b7*) had significantly higher expression in CD34$^-$ compared to CD34$^+$ HSCs, with 3 of them catalyzing NADPH-dependent reactions (Figures 3B, 3C, and S4C). We confirmed the increased expression of *Tm7sf2*, *Msmo1*, and *Hsd17b7* in sorted CD34$^-$ compared to CD34$^+$ HSCs (Figure 3D).

To confirm the bioinformatic predictions, untargeted metabolomic analysis was performed. Metabolic pathway enrichment analysis highlighted the differential contribution of pathways linked to lipid synthesis (especially phospholipid and phosphatidylcholine biosynthesis), carbohydrate metabolism, and others (Figure S5A and Table S3). Steroid synthesis is also found among the enriched pathways, although it is not one of most prominent. This is most likely because we performed our untargeted metabolomics on the polar phase, while sterols are non-polar metabolites.

To overcome this limitation, we subjected the non-polar metabolite extracts of separated NAD(P)H^{Hi} and NAD(P)H^{Lo} CD34$^-$ HSCs to a sterol analysis by gas chromatography-coupled mass spectrometry. We detected cholesterol and 12 other sterol species. We clustered 2 groups based on their specific sterol signature by partial least squares-discriminant analysis (PLS-DA) (Figure 4A, left). The levels of cholesterol were significantly lower in NAD(P)H^{Lo} compared to NAD(P)H^{Hi} CD34$^-$ HSCs (Figure 4A, right; Table S4).

We used staining of fixed cells with filipin III (hereafter referred to as filipin) and flow cytometry to confirm cholesterol levels.[38] CD34$^-$ HSCs showed higher intensity of filipin compared to CD34$^+$ HSCs (Figure S5B). Further, fluorescence microscopy analysis of sorted HSCs indicated that NAD(P)H^{Hi} CD34$^-$ HSCs have higher filipin intensity than NAD(P)H^{Lo} CD34$^-$ HSCs (Figure 4B). Enzymatic determination of total intracellular cholesterol confirmed its enrichment in NAD(P)H^{Hi} CD34$^-$ HSCs compared to NAD(P)H^{Lo} (Figure 4C). Consistently, long-term HSC purification based on EPCR positivity displayed the same trend (Figure S5C).

(C) Volcano plot relating the difference in NAD(P)H intensity between each daughter and its mother. (n = 3 independent experiments). Red box: daughters with not statistically different from the mother; gray box: daughter with NAD(P)H significantly lower than the mother; green box: daughter with NAD(P)H significantly higher than the mother.

(D) Timelapse traces of NAD(P)H intensity for each class of division. Cytokinesis is marked by a black arrow; the x axis represents hours of time-lapse imaging since the start of tracking of each mother cell.

(E and F) HSC capacity is enriched in NAD(P)H^{Hi} cells of Div 1 cells. 36 h after *in vitro* culture of CD34$^-$ HSCs, single NAD(P)H^{Hi} or NAD(P)H^{Lo} Div 1 cells were isolated onto 96-well plate (also see Figure 2A) then followed by a long-term cultu©(E) or single-cell transplantation with 4.0 × 10^5 competitor BMMNCs (F). Colony replating capacity of these single cells (E, n = 48 cells) and the frequency of successful engraftment (>1% donor contribution in multi-lineage hematopoiesis) (F, n = 20) were determined.

(G and H) Percentages of hematopoietic contribution in peripheral blood of recipient mice transplanted with paired daughter cells. Single CD34$^-$ HSC division was identified *in vitro* and then each daughter was imaged to determine NAD(P)H levels and individually transplanted with 2 × 10^5 competitor BMMNCs into irradiated recipient mice. Chimerism was evaluated at 4 months after BMT (10 divisions, for a total of 20 daughter cells analyzed). The division patterns of the investigated division based on donor contribution (H).

BMMNCs, bone marrow mononuclear cells; HSC, Lin$^-$Sca-1$^+$c-Kit$^+$CD135$^-$CD150$^+$CD48$^-$. (E): Student's paired t test. (F): nonparametric Kolmogorov-Smirnov test. ****, $p < 0.0001$; *, $0.01 \leq p < 0.05$; N.S., not significant, $p \geq 0.05$. See also Figure S3.

Farnesyl pyrophosphate, an intermediate of the cholesterol pathway, can be a substrate for protein prenylation as well.[39] Results obtained from NAD(P)H^{Hi} and NAD(P)H^{Lo} CD34$^-$ HSCs indicate that high NAD(P)H correlates with high levels of protein farnesylation (Figure S5D), confirming the higher flux through the mevalonate pathway. Finally, sorted NAD(P)H^{Hi} CD34$^-$ HSCs exposed to FCCP or H_2O_2 display a cholesterol content comparable to the NAD(P)H^{Lo} counterparts (Figure S5E).

Next, we isolated HSPCs and then induced TPNOX and mitoTPNOX expression as previously described (Figures 1L, S2N, and S2O). After 2 weeks of culture, filipin staining indicates that mitoTPNOX, but not cytosolic TPNOX, significantly reduces cholesterol levels (Figure 4D).

Cholesterol biosynthesis requires cytosolic acetyl-CoA as a carbon source. We speculated that in HSCs, FAO supports cholesterol biosynthesis also by providing acetyl-CoA. Mitochondrial acetyl-CoA is transported to the cytosol in form of citrate by the mitochondrial citrate transport protein (CTP, coded by *Slc25a1*), which is then converted to acetyl CoA by ATP citrate lyase (ACLY).[40,41] CD34$^-$ HSCs displayed significantly higher expression of *Slc25a1* compared to CD34$^+$ HSCs (Figure S5F), and NAD(P)H^{Hi} CD34$^-$ HSCs, exposed *in vitro* to inhibitors of SLC25A1 or ACLY (BTC and BMS-303141, respectively), reduced cholesterol synthesis (Figure S5G). Similar to *Cpt1* levels, single-cell qPCR has confirmed that *Slc25a1* expression correlates with NAD(P)H levels in single HSC daughter cells (Figures S3F and S5H). These results suggest that NAD(P)H production (via FAO) and citrate shuttling undergo the same mechanism of segregation during HSC division.

Both the *in vitro* administration of BIBB-515 (inhibitor of 2,3-oxidosqualene cyclase [OSC], catalyst of a mandatory step of cholesterol biosynthesis)[42] and the exposure to methyl-β-cyclodextrin (MBCD, an oligosaccharide able to extract cholesterol from the plasma membrane)[43] significantly reduced LTC-IC capacity of NAD(P)H^{Hi} but not NAD(P)H^{Lo} CD34$^-$ HSCs (Figures S5I and S5J).

These data prompted us to test cholesterol inhibition on an *in vivo* setting. Statins are inhibitors of β-hydroxy β-methylglutaryl-CoA (HMG-CoA)-synthase widely tested in mice and humans. The *in vitro* treatment with lovastatin reduced filipin intensity in NAD(P)H^{Hi} CD34$^-$ HSCs to levels comparable to those of NAD(P)H^{Hi} CD34$^-$ HSCs exposed to MBCD or NAD(P)H^{Lo} CD34$^-$ HSCs (Figure 4E). Low dosage of lovastatin reduced *in vitro* LTC-IC capacity of NAD(P)H^{Hi} CD34$^-$ HSCs (Figure S5K) and significantly impaired the *in vivo* reconstitution capacity of NAD(P)H^{Hi} CD34$^-$ HSCs in competitive reconstitution assays (Figures 4F and 4G). Further, HSC cholesterol deprivation via MBCD also significantly impaired the *in vivo* reconstitution capacity of NAD(P)H^{Hi} CD34$^-$ HSCs (Figures 4F and 4G). The incubation with cholesterol-saturated MBCD (MBCD:Chol) increases cholesterol content in NAD(P)H^{Lo} CD34$^-$ HSCs[44] (Figure 4H), leading to enhanced colony-replating capacity of CD34$^-$ HSCs after long-term culture (Figure 4I).

The observations prompted us to test the impact of media composition on the NADPH-FAO-cholesterol axis. Reference media was supplemented with 1% BSA and 50 ng/mL stem cell factor (SCF)/thrombopoietin (TPO) (see STAR Methods and Figure S5L), and we tested the dilution or substitution of BSA as well as lowered the concentration of SCF/TPO to 1 ng/ml (Figure S5L). In sorted CD34$^-$ Lin$^-$Sca-1$^+$c-Kit$^+$ (KSL) cells, only low BSA concentration or its substitution with polyvinyl alcohol (PVA) potentiated the NADPH-cholesterol axis (Figures S5M and S5N). These observations are consistent with previous data showing that a low BSA concentration in the media supports HSC maintenance *in vitro*[45,46] and stimulates the synthesis of cholesterol and fatty acids.[45]

Altogether, these data indicate that *in vitro* manipulation of cholesterol levels directly impacts the function of HSCs.

FAO sustains NADPH and cholesterol synthesis

We hypothesized that most of the electrons required to reduce the NAD(P)H pool in NAD(P)H^{Hi} CD34$^-$ HSCs are derived from FAO.[47] In agreement, NAD(P)H^{Hi} CD34$^-$ HSCs exposed *in vitro* to the Cpt1 inhibitor etomoxir display reduced cholesterol levels (Figure 5A). We thus decided to genetically inactivate FAO. Cpt1 is reported to be sensitive to adenosine monophosphate-activated protein kinase (AMPK) activity,[48] a known regulator of HSCs,[49–51] and pharmacological inhibition of Cpt1 can induce oligomerization of the pro-apoptotic members of the Bcl-2 family Bax and Bak.[52,53] Because of these connections between Cpt1 and factors external to FAO that could bias the data interpretation, we decided to develop *Cpt2* conditional knockout mice (*Cpt2$^{f/f}$ Vav-iCre$^+$* or *Cpt2* cKO). At steady state, *Cpt2$^{f/f}$ Vav-iCre$^+$* mice displayed a reduced frequency of CD34$^-$ HSCs (Figure S6A) and a significantly diminished proportion of CD34$^-$ in the NADPH^{Hi} gate (Figure 5B), while no alterations of mitochondrial mass (Figure S6B) were detected. Reduced intensity of filipin staining was also found in CD34$^-$ HSCs from *Cpt2$^{f/f}$ Vav-iCre$^+$* mice (Figure 5C). Enrichment of cholesterol by MBCD:Chol restores the colony-forming capacity of *Cpt2*-deleted HSCs after long-term culture (Figures 5D and 5E). We then tested the self-renewal capacity of HSCs from *Cpt2* cKO mice. We first analyzed the cell fate impact of NAD(P)H per single mitochondria segregation on the first division of single NAD(P)H^{Hi} CD34$^-$ HSCs from *Cpt2$^{f/f}$ Vav-iCre$^-$* and *Vav-iCre$^+$* mice, as described in Figure 2A. The proportions of asymmetric, symmetric high, and symmetric low distribution in NAD(P)H^{Hi} CD34$^-$ *Cpt2$^{f/f}$ Vav-iCre$^-$* were comparable to that observed in control mice (Figures 2B and 5F). Interestingly, no symmetric high division was observed for NAD(P)H^{Hi} CD34$^-$ HSCs from *Cpt2$^{f/f}$ Vav-iCre$^+$* (0 out of 23), while the proportion of symmetric low rose from 36% (8 out of 22) in the *Cpt2$^{f/f}$ Vav-iCre$^-$* to 70% (16 out of 23) upon deletion of *Cpt2*. Consistently, competitive reconstitution and serial transplantation assays confirmed reconstitution impairment in recipients of HSCs from *Cpt2* cKO mice (Figures S5G–S5I and S6C).

Cholesterol synthesis regulated by PPAR-FAO contributed to HSC capacity

Peroxisome proliferator-activated receptor-delta (PPARδ)-specific agonist GW501516, which enhances FAO, was utilized to assess the impact of targeting the FAO-NADPH-cholesterol axis on HSC capacity. Exposure to GW501516 can potently increase cholesterol levels in NAD(P)H^{Lo} CD34$^-$ HSCs (Figure S6D). We then assessed cKO mice for Ppar gamma coactivator 1-alpha (*Ppargc1a*) in hematopoietic tissues. The *Ppargc1a* gene (or *Pgc1a*) is a co-activator stimulating PPAR factors to induce mitochondrial biogenesis and favor multiple catabolic

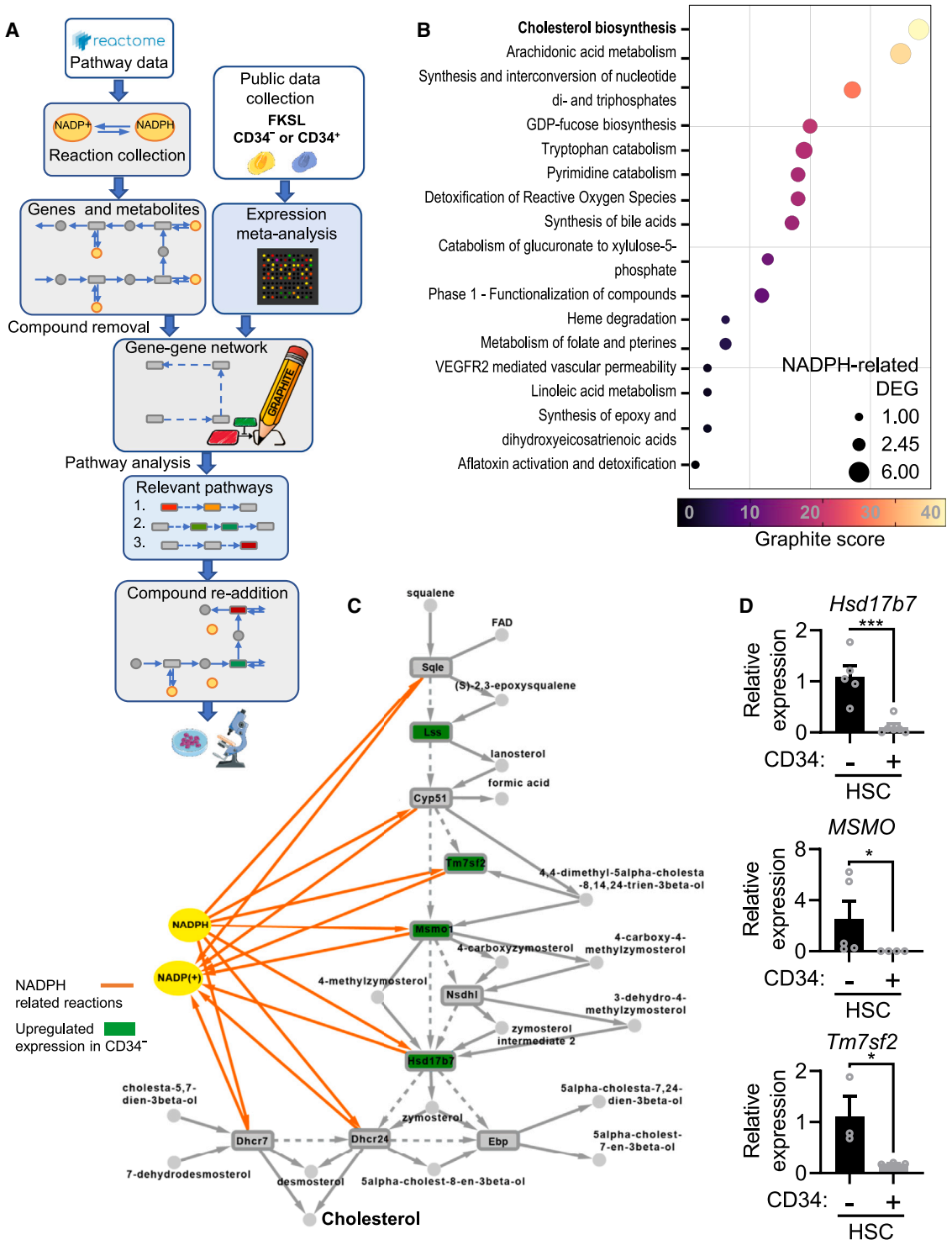

Figure 3. Identification of NADPH-dependent pathways in HSCs

(A) Flow diagram of the pathway analysis used to identify NADPH-dependent reactions differentially regulated in CD34$^+$ compared to CD34$^-$ HSCs.

(B) NADPH-dependent pathway enriched in the CD34$^-$ HSCs and ranked after their Graphite score. Dot size represents the number of NADPH-related differentially expressed genes (DEGs) identified.

(C) Schematic representation of the cholesterol biosynthesis pathway derived from the pathway analysis. Green nodes are differentially expressed genes (all upregulated in CD34$^-$ compared to CD34$^+$ HSCs). Orange arrows highlight NADPH-dependent reactions.

(D) Levels of *Hsd17b7*, *MSMO*, and *Tm7sf2* in sorted CD34$^-$ and CD34$^+$ HSCs quantified by qPCR relative to *ActB*. HSC, Lin$^-$Sca-1$^+$c-Kit$^+$ CD135$^-$CD150$^+$CD48$^-$; DEG, differentially expressed genes. Bar graphs represent means ± SEM, circles represent each replicate. (D): unpaired Student's t test. ***, $0.0001 \leq p < 0.001$; *, $0.01 \leq p < 0.05$. See also Figure S4.

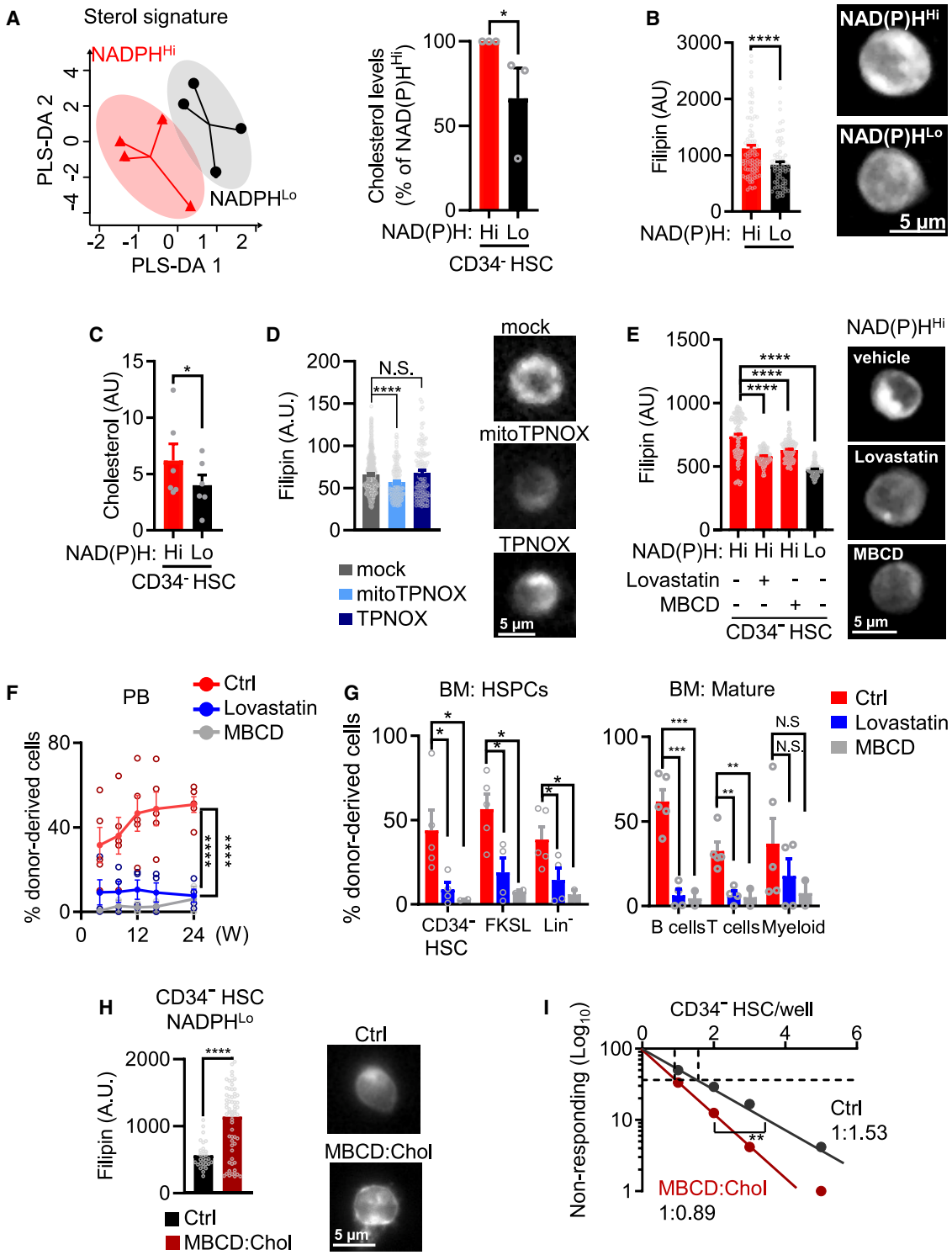

Figure 4. NADPH sustains cholesterol biosynthesis in HSC

(A) Partial least squares-discriminant analysis (PLS-DA) of sterol signature (left) and relative quantitation of cholesterol (right) identified by mass spectrometry in NAD(P)H^{Hi} or NAD(P)H^{Lo} CD34$^-$ HSCs (n = 4). Ellipses display confidence level at 95%.

(B) Quantitation (left) and staining (right) of the cholesterol sensitive dye filipin in NAD(P)H^{Hi} and NAD(P)H^{Lo} CD34$^-$ HSCs (n = NAD(P)H^{Hi}: 85 cells, NADPH^{Lo}: 67 cells).

(C) Enzymatic detection of total intracellular cholesterol in sorted NAD(P)H^{Hi} or NAD(P)H^{Lo} CD34$^-$ HSCs.

(legend continued on next page)

reactions.[54,55] *Pgc1a* deletion induces significant reduction of FAO rates, which can be rescued by administration of GW501516.[56] Although *Ppargc1a*$^{f/f}$ *Vav-iCre*$^{+}$ mice showed no alterations in bone marrow composition or mitochondria numbers (Figures S6E and S6F), CD34^{-} HSCs from *Ppargc1a*$^{f/f}$ *Vav-iCre*$^{+}$ mice showed lower NAD(P)H autofluorescence and cholesterol levels than littermate controls (Figures S6G and S6H). *In vitro* GW501516 exposure restored the cholesterol content of *Pgc1a*-depleted HSCs, an effect overcome by forcing NADPH consumption via co-exposure to both FCCP or H_2O_2 (Figures S6H). In a competitive BMT setting (Figure S6I), *Pgc1a*-deleted HSCs showed impaired reconstitution capacity, which was partially but significantly rescued by GW501516 (Figure S6I).

NADPH supports the biogenesis of EVs in HSCs

Our results indicate that proper levels of NADPH support the synthesis of cholesterol, suggesting a role for NADPH in the biogenesis of the plasma membrane or other components of the endomembrane system. Because NAD(P)H^{Hi} and NAD(P)H^{Lo} CD34^{-} HSCs are both quiescent (Figures S2E–S2G), indicating no demand for membrane biogenesis to support cell division, we hypothesized that higher cholesterol synthesis would be required for the biogenesis of extracellular vesicles (EVs).[57]

Thus, we cultured HSCs in fetal bovine serum (FBS)-free media to allow the enrichment in the media of any spontaneously released EVs. Nanoparticle tracking analysis (NTA) identifies a significant amount of EVs released by HSCs, with an average diameter of ~95 nm (Figure 6A) confirmed by a tunable resistive pulse-sensing (TRPS) system (median diameter of ~112 nm) (Figure S7A). Finally, we used transmission electron microscopy to confirm that EVs from HSCs exhibit a cup-like morphology typical of exosomes (Figure S7B).

Next, we tested whether HSCs could produce transferable EVs using PKH26, a lipid-specific fluorescent marker, which incorporates with double-layered membranes and is retained by EVs after their release (Figure 6B, top). As a negative control, the same number of compensation beads (with no EV release) were processed in parallel (Figure 6B, bottom). HSCs exposed to PKH26-stained EVs only displayed a marked PKH26 signal at the cell edge and in the cytosol (Figure 6C).

NTA further showed that other bone marrow populations, including Nestin^{+} mesenchymal stem cells (MSCs), could also produce EVs (Figure S7C).

To determine the impact of defects in the NADPH-cholesterol axis on EV biogenesis, CD34^{-} HSCs were isolated from *Cpt2*$^{f/f}$ *Vav-iCre*$^{-}$ or *Vav-iCre*$^{+}$ mice and cultured for 48 h. The conditional deletion of *Cpt2* significantly affected the number of EVs retrieved, but this was partially recovered by exposure of HSCs to MBCD:Chol (Figure 6D). The diameter of these EVs was not affected (Figure S7D).

Tetraspanins are a family of transmembrane proteins found in EVs that participate in their biogenesis and cargo selection.[58] Cholesterol metabolism supports the cycling of tetraspanins (including CD9 and CD63) within the endomembrane system, and inhibition of cholesterol biosynthesis impairs tetraspanin loading into EVs.[59–62] Thus, we investigated the expression of CD63 and CD9 on EVs derived from *Cpt2*-deleted HSCs using a flow cytometry and immunomagnetic beads-based methodology. We confirmed that genetic inactivation of FAO resulted in the drastic reduction of CD63 and CD9 in EVs from HSCs (Figures S7E and S7F), and these defects can be reverted by the replenishment of intracellular cholesterol (Figures S7E and S7F).

Magnetic enrichment of EVs cannot resolve marker expression for single EVs but rather provides its expression for the whole EV population. To test the content of EV markers at single EV levels, we used enhanced super-resolution radial fluctuations (eSRRF) microscopy that has been demonstrated to resolve structure close to 100 nm.[63] We used commercially available fluorescent beads, which confirmed that eSRRF imaging is in a resolution domain compatible with EV investigation (Figures S7G and S7H). Next, HSC-derived EVs were immunostained for CD63 and imaged using eSRRF microscopy (Figure S7I).

This single-EV technique suggests that conditional *Cpt2* deletion affects CD63 levels in EVs, which were partially recovered by the replenishment of intracellular cholesterol (Figure 6E). Finally, we use a recently developed high-resolution single-particle platform, NanoFCM NanoAnalyzer (nFCM), to investigate the expression of CD63 on HSC-derived EVs.[64] The nFCM analysis confirmed that CD63 loading into EVs is dependent on the FAO-cholesterol axis and that external supplementation of cholesterol can partially recover CD63 loading in FAO-deficient HSCs (Figure 6F).

Because HSCs actively produce EVs and their biology depends on FAO and cholesterol, we investigated the impact of EVs on HSC function. We measured NAD(P)H levels and mitochondrial mass of CD34^{-} HSCs cultured in the presence of

(D) Quantitation (left) and images (right) of filipin staining in the cultured KSL expressing TPNOX, mitoTPNOX, or empty vector (mock) after 2 weeks of culture with doxycycline (mock, n = 551 cells; TPNOX, n = 119 cells; mitoTPNOX, n = 140 cells).
(E) Quantitation (left) and images of filipin (right) in sorted NAD(P)H^{Hi} and NAD(P)H^{Lo} CD34^{-} HSCs then cultured for 24 h with 37.5 nM lovastatin, an inhibitor of cholesterol synthesis, or for 2 h after cholesterol sequestration by 1.5 mM methyl-β-cyclodextrin (NAD(P)H^{Hi}, n = 141 cells; NAD(P)H^{Hi} + Lovastatin, n = 137 cells; NAD(P)H^{Hi} + MBCD, n = 102 cells; NAD(P)H^{Lo}, n = 107 cells).
(F and G) Analysis of BMT of five NAD(P)H^{Hi} CD34^{-} HSCs exposed to 37.5 nM lovastatin (for 24 h *in vitro*), 1.5 mM MBCD (2 h *in vitro*) or Vehicle (Ctrl), with 4.0 × 10^{5} competitor BMMNCs. (F) Percentages of donor-derived cells in the peripheral blood of recipient mice. (G) Percentages of donor-derived cells in HSPCs (left) or mature cells (right) from the bone marrow of recipient mice at 6 months after BMT.
(H) Quantitation (left) and images (right) of filipin staining in NAD(P)H^{Lo} CD34^{-} HSCs exposed to cholesterol-saturated MBCD. n ≥ 12 replicates, 3 independent experiments. (I) LTC-IC capacity of CD34^{-} HSCs exposed to cholesterol-saturated MBCD (Ctrl, n = 29, MBCD:Chol, n = 64). PLS-DA, Partial least squares-discriminant analysis; Lov, Lovastatin; HSC, Lin^{-}Sca-1^{+}c-Kit^{+}CD135^{-}CD150^{+}CD48^{-}; MBCD, methyl-β-cyclodextrin. Scale bars, 5μm. Bar graphs represent means ± SEM, circles represent each replicate. (A): nonparametric Mann-Whitney U test. (B) and (H): unpaired Student's t test. (C) and (I): Student's paired t test. (D) and (E): one-way ANOVA with Dunnet's multiple comparison test. (F) and (G): two-way ANOVA with Sidak's multiple comparison test. ****, $p < 0.0001$; ***, $0.0001 \leq p < 0.001$; **, $0.001 \leq p < 0.01$; *, $0.01 \leq p < 0.05$; N.S., not significant, $p > 0.05$. See also Figure S5.

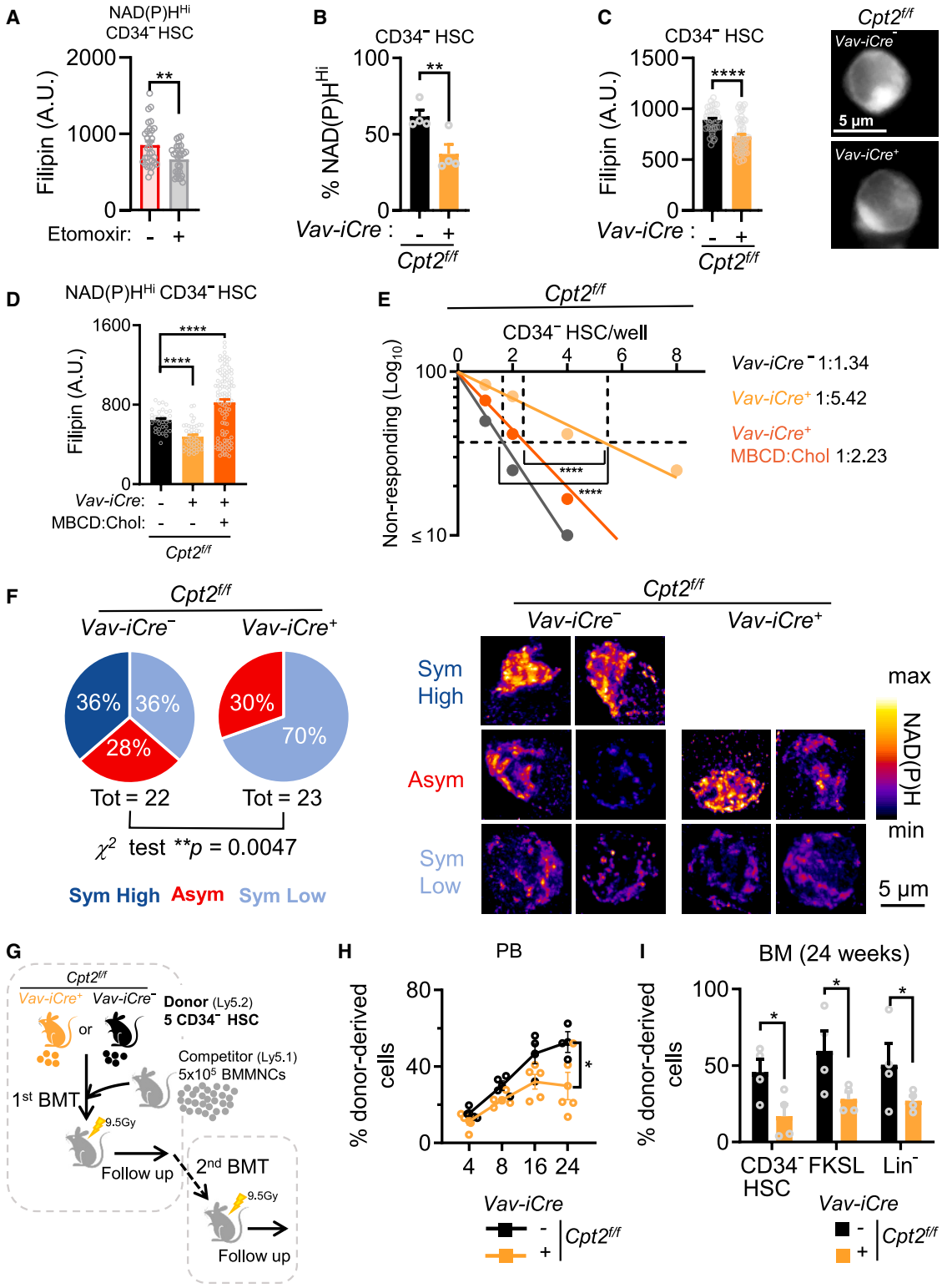

Figure 5. FAO sustains NADPH and cholesterol axis

(A) Quantitation of filipin staining in NAD(P)H^{Hi} CD34^{-} HSCs exposed to etomoxir for 24 h *in vitro* (vehicle, n = 30 cells; etomoxir, n = 31 cells).

(B) Proportion of NAD(P)H^{Hi} cells in CD34^{-} HSCs from *Cpt2* $^{f/f}$ *Vav-iCre*$^{-}$ and *Vav-iCre*$^{+}$ mice. NAD(P)H^{Hi} gate was defined as in Figure 1H.

(C) Quantitation (left) and images (right) of filipin staining in CD34^{-} HSCs from *Cpt2*$^{f/f}$ *Vav-iCre*$^{-}$ and *Vav-iCre*$^{+}$ mice (*Vav-iCre*$^{-}$, n = 40 cells; *Vav-iCre*$^{+}$, n = 56).

(legend continued on next page)

HSC-derived EVs or compensation bead-derived negative controls. EV exposure elevates NAD(P)H levels in acceptor HSCs while lowering their mitochondrial mass (Figures S7J and S7K), two features of mitochondrial physiology that distinguish HSCs from committed progenitors, as indicated by our observation (Figures 1A–1J) and multiple reports.[7,10,65] In addition, the exposure of HSCs to HSC-derived EVs significantly increased the expression of SCF. This effect was not observed when EVs were obtained from committed progenitor (FKSL or Lin$^-$) cells or MSCs (Figures S7L), although HSCs do appear to actively take up EVs from these other origins (Figures S7L and S7M).

We then test whether EV supplementation regulated HSC function by measuring the reconstitution potential *in vivo*. CD34$^-$ HSCs were isolated and cultured for 48 h with HSC-derived EVs or vehicle and then subjected to competitive BMT (Figure 6G, left). Strikingly, HSCs supplemented with EVs displayed a higher capacity to reconstitute the hematopoietic system without lineage bias compared to HSCs receiving vehicle in both peripheral blood (Figure 6G) and bone marrow (Figure 6H). These results confirm that HSCs can stimulate their self-renewal potential in an autocrine manner through EV-mediated signaling.

To confirm this new paradigm, we inhibited EV formation *in vitro* by treating HSPCs with GW4869 (inhibitor of neutral sphingomyelinase, widely used to block EV generation)[66] and then measuring their colony-forming capacity upon serial replating. While vehicle-treated HSPCs were able to produce colonies after three re-platings, cells treated with GW4869 only formed colonies in the first two re-platings, indicating loss of self-renewal (Figure S7N).

Rab27a regulates EV secretion by promoting multivesicular endosome docking at the plasma membrane.[67] To confirm *in vivo* the inhibition of EV formation on HSC function, we used a Dox-inducible short hairpin RNA (shRNA) for Rab27a, able to reduce the production of EVs *in vitro* (Figure S7O). Sorted FKSL cells were infected *in vitro* and selected with G418 (1 μg/mL) before undergoing competitive BMT (Figure 6I, left). Dox induction (performed 2 weeks after BMT) resulted in a dramatic loss of reconstitution potential without lineage bias in both peripheral blood (Figure 6I) and bone marrow (Figure 6J) 2 weeks after Dox administration and remained stable up to 18 weeks. These findings prompted us to investigate the impact of Rab27a downregulation on HSPCs. We replicated the competitive BMT with infected FKSL cells (as in Figure 6I), focusing the follow-up during the first 3 weeks of Dox induction. In peripheral blood, the effect was visible a week after and became progressively more obvious in the following weeks (Figure S7P). After 3 weeks of Dox induction, mice were euthanized, and defective reconstitution was observed in all the populations tested (Figure S7Q). These results imply that downregulation of Rab27a had a specific impact not only on HSCs but also potentially on the function of progenitor cells.

HSCs reside in a special microenvironment in the bone marrow called the HSC niche (or the niche) that maintains hematopoietic homeostasis through interactions between various niche cells/factors and HSCs.[68] It has been proposed that EVs participate in this complex microenvironment.[69–71] Although our data propose that HSC-derived EVs stimulate HSC function in an autocrine manner, we hypothesized that this process could also involve the participation of supporting stromal cells.

Thus, we isolated EVs from HSCs, FKSL cells, and Lin$^-$ cells stained with PKH26, as described in Figure 6B. Fluorescently labeled EVs were next administered to bone marrow stromal cells *in vitro*, and the uptake of EVs was evaluated by fluorescence microscopy. Stromal cells preferentially take up EVs released by HSCs compared to those obtained from committed progenitors (Figure S7R). Interestingly, EVs derived from HSCs, but not from committed bone marrow progenitors, were able to potently stimulate SCF expression in stromal cells (Figure S7S). This suggests that EV-mediated signaling instructs stromal cells to provide a microenvironment favorable for HSC maintenance.

To finally corroborate this model, we measured the colony-forming ability of CD34$^-$ HSCs after 6 weeks of co-culture with stromal cells in the presence of GW4869. We observed that GW4869 significantly impairs HSC maintenance *in vitro*, confirming the importance of EV biogenesis in hematopoietic homeostasis (Figure S7T).

Overall, these data show that an NADPH-cholesterol axis controls the biogenesis of EVs in HSCs that participate in HSC maintenance through both autocrine- and paracrine-signaling mechanisms.

DISCUSSION

In the current study, we propose that mitochondria can directly support cholesterol synthesis under specific non-respiratory conditions in HSCs. Cholesterol is not synthesized in mitochondria, but we expect that the elevation of TCA cycle metabolites

(D and E) Quantification of filipin staining in NAD(P)H^{Hi} CD34$^-$ HSCs (D; *Cpt2*$^{f/f}$ *Vav-iCre*$^-$, n = 34, *Cpt2*$^{f/f}$ *Vav-iCre*$^+$, n = 47, *Cpt2*$^{f/f}$ *Vav-iCre*$^+$ MBCD:Chol, n = 99) and LTC-IC capacity of CD34$^-$ HSCs from the indicated genotyped mice (E, n ≥ 12 replicates, 3 independent experiments) exposed to cholesterol-saturated MBCD.

(F) Proportion of symmetric high (Sym High), asymmetric (Asym), or symmetric low (Sym low) distribution of mitochondrial NAD(P)H after first division of the cultured CD34$^-$ HSCs from *Cpt2*$^{f/f}$ *Vav-iCre*$^-$ and *Cpt2*$^{f/f}$ *Vav-iCre*$^+$ mice (left). Asymmetric distribution of NAD(P)H was determined as in Figure 2G (*Vav-iCre*$^-$, n = 22; *Vav-iCre*$^+$, n = 23). Images of TMRM and NAD(P)H of pair daughter cells are also shown (right).

(G) Experimental design for serial transplantation with *Cpt2*$^{f/f}$ *Vav-iCre*$^-$ and *Vav-iCre*$^+$ CD34$^-$ HSCs. Five CD34$^-$ HSCs from *Cpt2*$^{f/f}$ *Vav-iCre*$^-$ or *Vav-iCre*$^+$ were transplanted into lethally irradiated Ly5.1 recipient mice together with 5x10^5 competitor BMMNCs (1st BMT). After 6 months of follow up, BMMNC were isolated from each recipient mouse with positive reconstitution and transplanted into secondary recipient mice (1 x 10^6 BMMNCs/secondary recipient mouse). The hematopoiesis of the recipient mice was followed for 16 weeks.

(H and F) Percentages of donor-derived cells in peripheral blood (H) or bone marrow HSPCs (F) of recipient mice at the indicated weeks after 1st BMT (also see Figure S6C).

BMT, bone marrow transplantation. Scale bar, 5μm. Bar graphs represent means ± SEM, circles represent each replicate. (A) and (E): Student's paired t test. (B) and (C): unpaired Student's t test. (D): one-way ANOVA with Dunnet's multiple comparison test. (F), χ^2 test. (H) and (I): two-way ANOVA with Sidak's multiple comparison test. ****, $p < 0.0001$; ***, $0.0001 \leq p < 0.001$; **, $0.001 \leq p < 0.01$; *, $0.01 \leq p < 0.05$; N.S., not significant, $p > 0.05$. See also Figure S6.

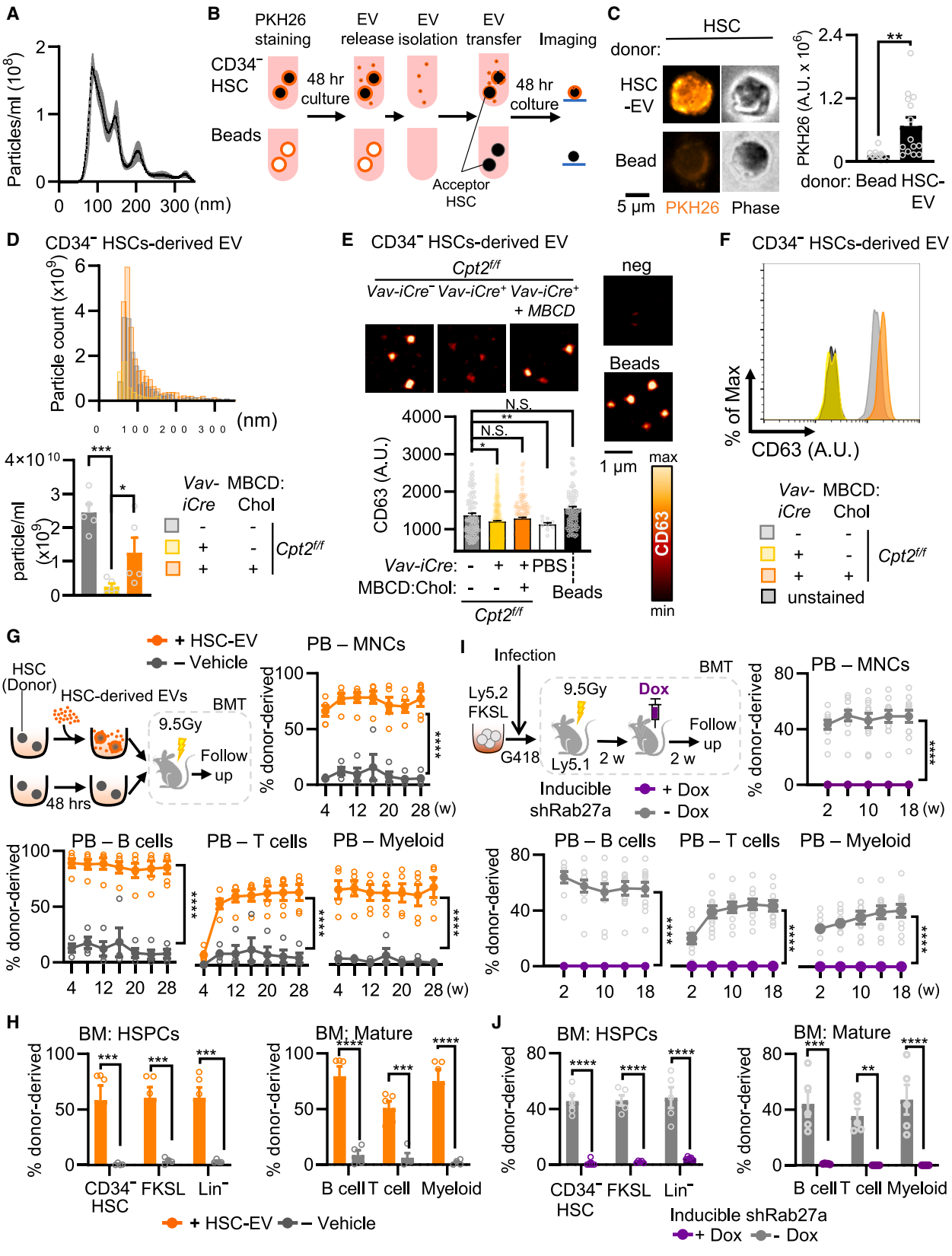

(legend on next page)

and mitochondrial NADH (driven by the high rate of FAO in HSCs) promote the elevation of NADPH through mitochondrial shuttle systems and the redundant reactions that keep NADH and NADPH in equilibrium.[72] Mitochondrial metabolism in HSCs may generate an outward flux of reduced nicotinamide cofactors and metabolites (e.g., citrate), which would then become available for the synthesis of cholesterol in the cytosol and the endoplasmic reticulum (ER) membrane. Exchange of NADPH between the mitochondria and ER could be favored by their sites of close association, which have been reported to be enriched in cholesterol.[73] Also, genetic lowering of these contacts has been shown to affect HSC self-renewal capacity.[74]

A recent study described the impact of citrate conversion to acetyl-CoA in HSCs after 5-fluorouracil (5-FU) induced myeloablation in mouse.[75] In this report, in the first days after 5-FU administration, HSCs undergo expansion, and in a subsequent phase, they change fate toward differentiation. In this setting, citrate-derived acetyl-CoA supports both self-renewal and differentiation by regulating the histone acetylation landscape and gene transcription.[75] Our study offers a deeper insight into this mechanism, reporting that in HSCs, citrate and acetyl-CoA derived from FAO are required for cholesterol synthesis (Figure S5G), which is instrumental for self-renewal. This also implies that regulation of histone acetylation might be relevant for HSC differentiation more than self-renewal. In support, our data show that inhibition of the mevalonate pathway by lovastatin or BIBB-515 (expected to boost acetyl-CoA levels) causes HSC exhaustion, strongly deteriorating long-term reconstitution capacity rather than supporting self-renewal capacity (Figures 4F, 4G, S5I, and S5J).

Previous reports have indicated that cholesterol efflux regulates HSC maintenance and that elevation of cholesterol plasmatic levels or inhibition of its efflux induces proliferation and mobilization of HSCs and progenitor cells via increased expression of the IL-3/GM-CSF receptor[18] or the production of G-CSF.[76] Despite these reports, cholesterol levels in purified HSCs and their functional role had yet to be determined. Here, we define that HSCs exhibit high cholesterol synthesis, which favors their self-renewal through a cell-autonomous function. Our results suggest, however, that this is (at least in part) mediated by an NADPH-cholesterol axis supporting the biogenesis of EVs, most likely exosomes.

EVs regulate cell-to-cell communication,[77] and multiple evidences indicate that some EVs can promote HSC maintenance by several mechanisms.[78,79] We discovered that HSCs actively release EVs and that EV biogenesis supports the proper maintenance of HSC capacity in concert with the NADPH-cholesterol axis. Most interestingly, we observed that the NADPH-cholesterol axis is required for the proper loading of CD9 and CD63 into HSC-derived EVs. This speculation is confirmed by an early study reporting asymmetric partitioning of the tetraspanins CD53 and CD63 in human cord blood-derived HSCs upon cell division *in vitro*[80] and is further supported by a recent study that demonstrated that murine HSCs have heterogeneous levels of CD63. The long-term *in vivo* repopulation capacities are enriched in CD63-high HSCs when compared to their CD63-low counterparts.[81]

Together with our *in vitro* findings, this evidence suggests that EVs released from HSCs support self-renewal via an autocrine-signaling mechanism. In addition, we observed that other bone marrow populations can produce EVs at levels comparable to HSCs. These include progenitor cells (FKSL), more differentiated precursor cells (Lin^-), and MSCs. We showed that while HSCs can take up EVs released from all these cells, only HSC-derived EVs can significantly stimulate the expression of SCF in HSCs. Critically, we found that bone marrow stromal cells also preferentially take up EVs isolated from HSCs compared to the ones isolated from more differentiated cells, again inducing a potent expression of SCF. This observation opens the possibility

Figure 6. NADPH supports the biogenesis of extracellular vesicles (EVs) in HSC

(A) Distribution of the diameter of EVs derived from HSCs determined by nanoparticle tracking analysis (NTA).

(B) Experimental strategy of EV transfer between donor and acceptor HSCs. Donor $CD34^-$ HSCs (black) or compensation beads (white) were sorted into FBS-free media, and stained with the lipid marker, PKH26 (orange). EVs were isolated and supplemented to freshly isolated acceptor HSCs, then EV-related PKH26 signal (orange) was determined by fluorescence microscopy.

(C) Images (left) and quantitation (right) of PKH26 staining in acceptor $CD34^-$ HSCs exposed to HSC-derived EVs (HSC-EV) or negative control (bead) (HSC-EV, n = 14 cells; bead, n = 11 cells).

(D) Particle size distributions of EVs from $CD34^-$ HSCs, measured by TRPS system. $CD34^-$ HSCs isolated from *Cpt2*$^{f/f}$ *Vav-iCre*$^-$ and *Vav-iCre*$^+$ mice were cultured *in vitro* for 48 h. A fraction of cells from *Cpt2*$^{f/f}$ *Vav-iCre*$^+$ mice were exposed to cholesterol-enriched methyl-β-cyclodextrin (MBCD:Chol). EVs were isolated and analyzed by TRPS (n = 5 independent experiments), frequency distribution of the diameter (top) and average concentration (bottom) are shown.

(E) The expression of EV marker CD63 at single EV level was determined by enhanced super-resolution radial fluctuation (eSRRF). Images of CD63 in $CD34^-$ HSCs-derived EVs (top) and quantitation of CD63 (bottom) in each (*Cpt2*$^{f/f}$ *Vav-iCre*$^-$, n = 87; *Cpt2*$^{f/f}$ *Vav-iCre*$^+$, n = 332; *Cpt2*$^{f/f}$ *Vav-iCre*$^+$ + MBCD:Chol, n = 138; PBS, n = 10; beads, n = 83). See also Figures S7G–S7I.

(F) Nanometric flow cytometry analysis of HSC-derived EVs immunostained for CD63 and investigated by NanoFCM NanoAnalyzer.

(G) Experimental design (left) and percentages of donor-derived cells (right) in various lineages of peripheral blood of recipient mice transplanted with HSCs supplemented with HSC-derived EVs. Per each recipient mouse, 25 $CD34^-$ HSCs were sorted and cultured for 48 h. During this period, HSCs were supplemented with HSC-derived EVs (+HSC-EV; 1.5×10^6 EV per single HSC). EV-free PBS was used as a vehicle. After 48 h of culture, the whole culture was transplanted into lethally irradiated Ly5.1 recipient mice together with 4×10^5 competitor BMMNCs.

(H) Percentages of donor-derived cells in the indicate fractions of the bone marrow of the recipient mice 28 weeks after BMT.

(I) Experimental design (left) and percentages of donor-derived cells (right) in various lineages of peripheral blood of recipient mice after Rab27a interfering. After infection and selection with G418, 2,000 live FKSL cells were transplanted into lethally irradiated Ly5.1 recipient mice together with 1×10^6 competitor BMMNCs. Doxycycline was supplemented in water starting at week 2 after BMT. The x axis represents weeks after doxycycline administration.

(J) Percentages of donor-derived cells in the indicated fractions of the bone marrow of the recipient mice 20 weeks after BMT.

EV, extracellular vesicles; HSC-EV, HSC-derived extracellular vesicles; FKSL, $CD135^-c\text{-}Kit^+Sca\text{-}1^+Lin^-$. Scale bar, 5μm. Bar graphs represent means ± S.E.M, circles represent each replicate. (C): Unpaired Student's t test. (D) and (E): one-way ANOVA with Dunnet's multiple comparison test. (G), (H), (I), and (J): two-way ANOVA with Sidak's multiple comparison test. ****, $p < 0.0001$; ***, $0.0001 \leq p < 0.001$; **, $0.001 \leq p < 0.01$; *, $0.01 \leq p < 0.05$; N.S., not significant, $p > 0.05$. See also Figure S7.

that HSC-derived EVs might regulate HSC self-renewal also by activating paracrine signaling within the complex bone marrow environment where HSCs reside.[68,82,83] EV-mediated communications among bone marrow cells could lead distinct outcomes influenced by the administration of GW4869. For instance, the study by Hurwitz et al.[84] focused primarily on HSPCs and short-term exposure to GW4869 and reported that short-term *ex vivo* exposure of HSPCs to GW4869 had an impact on multipotent progenitor (MPP) expansion and potentiated *in vivo* reconstitution (although this was biased toward myeloid lineages).[84] Our study likewise demonstrated that *ex vivo* exposure of HSPCs to GW4869 increased the number of colonies after initial replating. However, we found that prolonged exposure to GW4869 affected HSC activity, and the GW4869-treated colonies exhausted more rapidly than those produced by vehicle-treated cells, resulting in reduced numbers of colonies formed in subsequent replatings. We speculate that the discrepancies between the experimental designs and the observed results may highlight the existence of EV-mediated communications impacting MPP and possibly HSC function.

In summary, we propose that mitochondria maintain a pool of reduced NADPH in HSCs, which sustains cholesterol biosynthesis and EV biogenesis for proper HSC fate decision and homeostasis. Further studies will evaluate the potential application of this concept to HSC-related diseases and the improvement of HSC-transplantation techniques.

Limitations of the study

The pharmacological or genetic inhibition of EV biogenesis (by means of GW4869 or Rab27a downregulation, respectively) demonstrated the importance of proper EV biogenesis in the maintenance of HSCs and its potential impacts on the function of progenitor cells. We therefore cannot fully exclude the possibility that GW4869- or Rab27a-mediated EVs from HSCs may affect not only HSCs but also the function of progenitor cells or differentiated blood cells. Our experiments likewise cannot exclude that GW4869 exposure or knockdown of Rab27a affects the EV supply from committed hematopoietic cells. Rab27a and the target of GW4869 (neutral sphingomyelinase) are widely recognized as tools for blocking EV biogenesis[67,85–88]; however, Rab27a is also a regulator of the late endocytic pathway, while neutral sphingomyelinase is important in lipidome regulation. Our data cannot fully exclude a cell-intrinsic role for Rab27a or neutral sphingomyelinase in HSC function. However, we reached the same conclusions from multiple experimental settings/conditions that produced results supporting a positive correlation between EV levels and HSC function. Importantly, the effects of GW4869 and EV supplementation are mediated by mechanisms that are distinct from those of Rab27a inhibition. We expect that future mechanistic exploration of cargo selection in HSCs and progenitor cells will yield new insights at the single-cell level into the specific communications (e.g., autocrine, and paracrine) involved in HSC retention and/or self-renewal capacity within the physiological microenvironment.

STAR★METHODS

Detailed methods are provided in the online version of this paper and include the following:

SUPPLEMENTAL INFORMATION

Supplemental information can be found online at https://doi.org/10.1016/j.stem.2024.02.004.

ACKNOWLEDGMENTS

The authors would like to thank all members of the Ito laboratory and the Einstein Stem Cell Institute for their comments and the Einstein Flow Cytometry and Analytical Imaging core facilities (funded by National Cancer Institute grant P30 CA013330) and the FAS Small Molecule Mass Spectrometry Facility at Harvard University for their help in carrying out the experiments. This work was supported by the NIH (R01DK98263, R01DK115577, R01HL148852, and R01HL069438 to Ke. I., R01 DK123181 to T.N., S10OD021624 to I.G., U54CA193461 to D.T.S., and R01EB030061 to G.I.), the New York State Department of Health (C029154 to Ke. I., as Core Director of Einstein Single-Cell Genomics/Epigenomics), Leukemia and Lymphoma Society (DGP-24224-23 to Ke. I.), a fellowship from Alex's Lemonade Stand Foundation and Tap Cancer Out (to N.v.G.), Italian Association for Cancer Research (MFAG 2019 23522 to C.E.), Progetti di Rilevante Interesse Nazionale grants PRIN2017E5L5P3 (to P.P.), and Harvard Stem Cell Institute (to C.P.L.). Ke. I. is a Research Scholar of the Leukemia and Lymphoma Society (1360-19).

AUTHOR CONTRIBUTIONS

M.B., C.M., N.v.G., Ky. I., I.Z., Y.Z., L.F., and Y.J. contributed to the performance of the experiments and/or analysis of the data. E.C., G.S., and P.M. developed the bioinformatic algorithm and performed bioinformatics assays. N.v.G. performed metabolomics assays. T.N., F.M.L., T.F., C.P.L., B.Z., P.P., I.G., C.R., and D.T.S. provided advice and interpreted data. Ke. I. conceived and directed the study. M.B., C.M., N.v.G., and Ke. I. wrote the manuscript. All the authors contributed to the design of experiments, discussed the results, and commented on the manuscript.

DECLARATION OF INTERESTS

T.F. is a founder and equity holder in Generian Pharmaceuticals and Coloma Therapeutics. D.T.S. is a director and equity holder of Agios Pharmaceuticals, Magenta Therapeutics, Editas Medicines, Clear Creek Bio, and LifeVaultBio; he is a founder of Fate Therapeutics and Magenta Therapeutics and a consultant to FOG Pharma, VcanBio, and Flagship Pioneering.

Received: January 28, 2023
Revised: November 16, 2023
Accepted: February 8, 2024
Published: March 7, 2024

REFERENCES

1. Ito, K., and Ito, K. (2018). Hematopoietic stem cell fate through metabolic control. Exp. Hematol. *64*, 1–11. https://doi.org/10.1016/j.exphem.2018.05.005.
2. Lackner, L.L. (2019). The Expanding and Unexpected Functions of Mitochondria Contact Sites. Trends Cell Biol. *29*, 580–590. https://doi.org/10.1016/j.tcb.2019.02.009.
3. Bonora, M., Giorgi, C., and Pinton, P. (2022). Molecular mechanisms and consequences of mitochondrial permeability transition. Nat. Rev. Mol. Cell Biol. *23*, 266–285. https://doi.org/10.1038/s41580-021-00433-y.
4. Ito, K., Bonora, M., and Ito, K. (2019). Metabolism as master of hematopoietic stem cell fate. Int. J. Hematol. *109*, 18–27. https://doi.org/10.1007/s12185-018-2534-z.
5. Chandel, N.S., Jasper, H., Ho, T.T., and Passegué, E. (2016). Metabolic regulation of stem cell function in tissue homeostasis and organismal ageing. Nat. Cell Biol. *18*, 823–832. https://doi.org/10.1038/ncb3385.
6. Ito, K., Carracedo, A., Weiss, D., Arai, F., Ala, U., Avigan, D.E., Schafer, Z.T., Evans, R.M., Suda, T., Lee, C.H., and Pandolfi, P.P. (2012). A PML-PPAR-delta pathway for fatty acid oxidation regulates hematopoietic stem cell maintenance. Nat. Med. *18*, 1350–1358. https://doi.org/10.1038/nm.2882.
7. Ito, K., Turcotte, R., Cui, J., Zimmerman, S.E., Pinho, S., Mizoguchi, T., Arai, F., Runnels, J.M., Alt, C., Teruya-Feldstein, J., et al. (2016). Self-renewal of a purified Tie2+ hematopoietic stem cell population relies on mitochondrial clearance. Science *354*, 1156–1160. https://doi.org/10.1126/science.aaf5530.
8. Ansó, E., Weinberg, S.E., Diebold, L.P., Thompson, B.J., Malinge, S., Schumacker, P.T., Liu, X., Zhang, Y., Shao, Z., Steadman, M., et al. (2017). The mitochondrial respiratory chain is essential for haematopoietic stem cell function. Nat. Cell Biol. *19*, 614–625. https://doi.org/10.1038/ncb3529.
9. Bejarano-García, J.A., Millán-Uclés, Á., Rosado, I.V., Sánchez-Abarca, L.I., Caballero-Velázquez, T., Durán-Galván, M.J., Pérez-Simón, J.A., and Piruat, J.I. (2016). Sensitivity of hematopoietic stem cells to mitochondrial dysfunction by SdhD gene deletion. Cell Death Dis. *7*, e2516. https://doi.org/10.1038/cddis.2016.411.
10. Bonora, M., Ito, K., Morganti, C., Pinton, P., and Ito, K. (2018). Membrane-potential compensation reveals mitochondrial volume expansion during HSC commitment. Exp. Hematol. *68*, 30–37.e1. https://doi.org/10.1016/j.exphem.2018.10.012.
11. de Almeida, M.J., Luchsinger, L.L., Corrigan, D.J., Williams, L.J., and Snoeck, H.W. (2017). Dye-Independent Methods Reveal Elevated Mitochondrial Mass in Hematopoietic Stem Cells. Cell Stem Cell *21*, 725–729.e4. https://doi.org/10.1016/j.stem.2017.11.002.
12. Takihara, Y., Nakamura-Ishizu, A., Tan, D.Q., Fukuda, M., Matsumura, T., Endoh, M., Arima, Y., Chin, D.W.L., Umemoto, T., Hashimoto, M., et al. (2019). High mitochondrial mass is associated with reconstitution capacity and quiescence of hematopoietic stem cells. Blood Adv. *3*, 2323–2327. https://doi.org/10.1182/bloodadvances.2019032169.
13. Mansell, E., Sigurdsson, V., Deltcheva, E., Brown, J., James, C., Miharada, K., Soneji, S., Larsson, J., and Enver, T. (2021). Mitochondrial Potentiation Ameliorates Age-Related Heterogeneity in Hematopoietic Stem Cell Function. Cell Stem Cell *28*, 241–256.e6. https://doi.org/10.1016/j.stem.2020.09.018.
14. Pernes, G., Flynn, M.C., Lancaster, G.I., and Murphy, A.J. (2019). Fat for fuel: lipid metabolism in haematopoiesis. Clin. Transl. Immunology *8*, e1098. https://doi.org/10.1002/cti2.1098.
15. Gu, Q., Yang, X., Lv, J., Zhang, J., Xia, B., Kim, J.D., Wang, R., Xiong, F., Meng, S., Clements, T.P., et al. (2019). AIBP-mediated cholesterol efflux instructs hematopoietic stem and progenitor cell fate. Science *363*, 1085–1088. https://doi.org/10.1126/science.aav1749.
16. Westerterp, M., Gourion-Arsiquaud, S., Murphy, A.J., Shih, A., Cremers, S., Levine, R.L., Tall, A.R., and Yvan-Charvet, L. (2012). Regulation of hematopoietic stem and progenitor cell mobilization by cholesterol efflux pathways. Cell Stem Cell *11*, 195–206. https://doi.org/10.1016/j.stem.2012.04.024.
17. Yvan-Charvet, L., Pagler, T., Gautier, E.L., Avagyan, S., Siry, R.L., Han, S., Welch, C.L., Wang, N., Randolph, G.J., Snoeck, H.W., and Tall, A.R. (2010). ATP-binding cassette transporters and HDL suppress hematopoietic stem cell proliferation. Science *328*, 1689–1693. https://doi.org/10.1126/science.1189731.
18. Murphy, A.J., Akhtari, M., Tolani, S., Pagler, T., Bijl, N., Kuo, C.L., Wang, M., Sanson, M., Abramowicz, S., Welch, C., et al. (2011). ApoE regulates hematopoietic stem cell proliferation, monocytosis, and monocyte accumulation in atherosclerotic lesions in mice. J. Clin. Invest. *121*, 4138–4149. https://doi.org/10.1172/JCI57559.
19. Morganti, C., Bonora, M., Ito, K., and Ito, K. (2019). Electron transport chain complex II sustains high mitochondrial membrane potential in hematopoietic stem and progenitor cells. Stem Cell Res. *40*, 101573. https://doi.org/10.1016/j.scr.2019.101573.
20. Morganti, C., Cabezas-Wallscheid, N., and Ito, K. (2022). Metabolic Regulation of Hematopoietic Stem Cells. Hemasphere *6*, e740. https://doi.org/10.1097/HS9.0000000000000740.
21. Lengefeld, J., Cheng, C.W., Maretich, P., Blair, M., Hagen, H., McReynolds, M.R., Sullivan, E., Majors, K., Roberts, C., Kang, J.H., et al. (2021). Cell size is a determinant of stem cell potential during aging. Sci. Adv. *7*, eabk0271. https://doi.org/10.1126/sciadv.abk0271.
22. Lin, D.S., and Trumpp, A. (2023). Differential expression of endothelial protein C receptor (EPCR) in hematopoietic stem and multipotent progenitor cells in young and old mice. Cells Dev. *174*, 203843. https://doi.org/10.1016/j.cdev.2023.203843.
23. Iwasaki, H., Arai, F., Kubota, Y., Dahl, M., and Suda, T. (2010). Endothelial protein C receptor-expressing hematopoietic stem cells reside in the perisinusoidal niche in fetal liver. Blood *116*, 544–553. https://doi.org/10.1182/blood-2009-08-240903.
24. Anjos-Afonso, F., Buettner, F., Mian, S.A., Rhys, H., Perez-Lloret, J., Garcia-Albornoz, M., Rastogi, N., Ariza-McNaughton, L., and Bonnet, D. (2022). Single cell analyses identify a highly regenerative and homogenous human CD34+ hematopoietic stem cell population. Nat. Commun. *13*, 2048. https://doi.org/10.1038/s41467-022-29675-w.
25. Blacker, T.S., Mann, Z.F., Gale, J.E., Ziegler, M., Bain, A.J., Szabadkai, G., and Duchen, M.R. (2014). Separating NADH and NADPH fluorescence in live cells and tissues using FLIM. Nat. Commun. *5*, 3936. https://doi.org/10.1038/ncomms4936.

26. Liu, Z., Pouli, D., Alonzo, C.A., Varone, A., Karaliota, S., Quinn, K.P., Münger, K., Karalis, K.P., and Georgakoudi, I. (2018). Mapping metabolic changes by noninvasive, multiparametric, high-resolution imaging using endogenous contrast. Sci. Adv. *4*, eaap9302. https://doi.org/10.1126/sciadv.aap9302.

27. Quinn, K.P., Bellas, E., Fourligas, N., Lee, K., Kaplan, D.L., and Georgakoudi, I. (2012). Characterization of metabolic changes associated with the functional development of 3D engineered tissues by non-invasive, dynamic measurement of individual cell redox ratios. Biomaterials *33*, 5341–5348. https://doi.org/10.1016/j.biomaterials.2012.04.024.

28. Bonora, M., Ito, K., Morganti, C., Pinton, P., and Ito, K. (2018). Membrane-potential compensation reveals mitochondrial volume expansion during HSC commitment. Exp. Hematol. *68*, 30–37.. https://doi.org/10.1016/j.exphem.2018.10.012.

29. Mantel, C.R., O'Leary, H.A., Chitteti, B.R., Huang, X., Cooper, S., Hangoc, G., Brustovetsky, N., Srour, E.F., Lee, M.R., Messina-Graham, S., et al. (2015). Enhancing Hematopoietic Stem Cell Transplantation Efficacy by Mitigating Oxygen Shock. Cell *161*, 1553–1565. https://doi.org/10.1016/j.cell.2015.04.054.

30. Cracan, V., Titov, D.V., Shen, H., Grabarek, Z., and Mootha, V.K. (2017). A genetically encoded tool for manipulation of NADP(+)/NADPH in living cells. Nat. Chem. Biol. *13*, 1088–1095. https://doi.org/10.1038/nchembio.2454.

31. Yamamoto, R., Morita, Y., Ooehara, J., Hamanaka, S., Onodera, M., Rudolph, K.L., Ema, H., and Nakauchi, H. (2013). Clonal analysis unveils self-renewing lineage-restricted progenitors generated directly from hematopoietic stem cells. Cell *154*, 1112–1126. https://doi.org/10.1016/j.cell.2013.08.007.

32. Kerner, J., and Hoppel, C. (2000). Fatty acid import into mitochondria. Biochim. Biophys. Acta *1486*, 1–17. https://doi.org/10.1016/s1388-1981(00)00044-5.

33. Fabregat, A., Sidiropoulos, K., Garapati, P., Gillespie, M., Hausmann, K., Haw, R., Jassal, B., Jupe, S., Korninger, F., McKay, S., et al. (2016). The Reactome pathway Knowledgebase. Nucleic Acids Res. *44*, D481–D487. https://doi.org/10.1093/nar/gkv1351.

34. Liu, Y., Zhang, C., Li, Z., Wang, C., Jia, J., Gao, T., Hildebrandt, G., Zhou, D., Bondada, S., Ji, P., et al. (2017). Latexin Inactivation Enhances Survival and Long-Term Engraftment of Hematopoietic Stem Cells and Expands the Entire Hematopoietic System in Mice. Stem Cell Rep. *8*, 991–1004. https://doi.org/10.1016/j.stemcr.2017.02.009.

35. de Graaf, C.A., Choi, J., Baldwin, T.M., Bolden, J.E., Fairfax, K.A., Robinson, A.J., Biben, C., Morgan, C., Ramsay, K., Ng, A.P., et al. (2016). Haemopedia: An Expression Atlas of Murine Hematopoietic Cells. Stem Cell Rep. *7*, 571–582. https://doi.org/10.1016/j.stemcr.2016.07.007.

36. Sales, G., Calura, E., Martini, P., and Romualdi, C. (2013). Graphite Web: Web tool for gene set analysis exploiting pathway topology. Nucleic Acids Res. *41*, W89–W97. https://doi.org/10.1093/nar/gkt386.

37. Alomari, M., Almohazey, D., Almofty, S.A., Khan, F.A., Al Hamad, M., and Ababneh, D. (2019). Role of Lipid Rafts in Hematopoietic Stem Cells Homing, Mobilization, Hibernation, and Differentiation. Cells *8*, 630. https://doi.org/10.3390/cells8060630.

38. Ginsbach, C., and Fahimi, H.D. (1987). Labeling of cholesterol with filipin in cellular membranes of parenchymatous organs. Standardization of incubation conditions. Histochemistry *86*, 241–248. https://doi.org/10.1007/bf00490254.

39. Chang, H.Y., Cheng, T.H., and Wang, A.H.J. (2021). Structure, catalysis, and inhibition mechanism of prenyltransferase. IUBMB Life *73*, 40–63. https://doi.org/10.1002/iub.2418.

40. Wise, D.R., Ward, P.S., Shay, J.E.S., Cross, J.R., Gruber, J.J., Sachdeva, U.M., Platt, J.M., DeMatteo, R.G., Simon, M.C., and Thompson, C.B. (2011). Hypoxia promotes isocitrate dehydrogenase-dependent carboxylation of alpha-ketoglutarate to citrate to support cell growth and viability. Proc. Natl. Acad. Sci. USA *108*, 19611–19616. https://doi.org/10.1073/pnas.1117773108.

41. Du, J., Yanagida, A., Knight, K., Engel, A.L., Vo, A.H., Jankowski, C., Sadilek, M., Tran, V.T.B., Manson, M.A., Ramakrishnan, A., et al. (2016). Reductive carboxylation is a major metabolic pathway in the retinal pigment epithelium. Proc. Natl. Acad. Sci. USA *113*, 14710–14715. https://doi.org/10.1073/pnas.1604572113.

42. Stancu, C., and Sima, A. (2001). Statins: mechanism of action and effects. J. Cell Mol. Med. *5*, 378–387. https://doi.org/10.1111/j.1582-4934.2001.tb00172.x.

43. Besenicar, M.P., Bavdek, A., Kladnik, A., Macek, P., and Anderluh, G. (2008). Kinetics of cholesterol extraction from lipid membranes by methyl-beta-cyclodextrin–a surface plasmon resonance approach. Biochim. Biophys. Acta *1778*, 175–184. https://doi.org/10.1016/j.bbamem.2007.09.022.

44. Zidovetzki, R., and Levitan, I. (2007). Use of cyclodextrins to manipulate plasma membrane cholesterol content: evidence, misconceptions and control strategies. Biochim. Biophys. Acta *1768*, 1311–1324. https://doi.org/10.1016/j.bbamem.2007.03.026.

45. Kobayashi, H., Morikawa, T., Okinaga, A., Hamano, F., Hashidate-Yoshida, T., Watanuki, S., Hishikawa, D., Shindou, H., Arai, F., Kabe, Y., et al. (2019). Environmental Optimization Enables Maintenance of Quiescent Hematopoietic Stem Cells Ex Vivo. Cell Rep. *28*, 145–158.e9. https://doi.org/10.1016/j.celrep.2019.06.008.

46. Wilkinson, A.C., Ishida, R., Kikuchi, M., Sudo, K., Morita, M., Crisostomo, R.V., Yamamoto, R., Loh, K.M., Nakamura, Y., Watanabe, M., et al. (2019). Long-term ex vivo haematopoietic-stem-cell expansion allows nonconditioned transplantation. Nature *571*, 117–121. https://doi.org/10.1038/s41586-019-1244-x.

47. Carracedo, A., Cantley, L.C., and Pandolfi, P.P. (2013). Cancer metabolism: fatty acid oxidation in the limelight. Nat. Rev. Cancer *13*, 227–232. https://doi.org/10.1038/nrc3483.

48. Hardie, D.G. (2020). AMPK as a direct sensor of long-chain fatty acyl-CoA esters. Nat. Metab. *2*, 799–800. https://doi.org/10.1038/s42255-020-0249-y.

49. Nakada, D., Saunders, T.L., and Morrison, S.J. (2010). Lkb1 regulates cell cycle and energy metabolism in haematopoietic stem cells. Nature *468*, 653–658. https://doi.org/10.1038/nature09571.

50. Gurumurthy, S., Xie, S.Z., Alagesan, B., Kim, J., Yusuf, R.Z., Saez, B., Tzatsos, A., Ozsolak, F., Milos, P., Ferrari, F., et al. (2010). The Lkb1 metabolic sensor maintains haematopoietic stem cell survival. Nature *468*, 659–663. https://doi.org/10.1038/nature09572.

51. Gan, B., Hu, J., Jiang, S., Liu, Y., Sahin, E., Zhuang, L., Fletcher-Sananikone, E., Colla, S., Wang, Y.A., Chin, L., and Depinho, R.A. (2010). Lkb1 regulates quiescence and metabolic homeostasis of haematopoietic stem cells. Nature *468*, 701–704. https://doi.org/10.1038/nature09595.

52. Samudio, I., Harmancey, R., Fiegl, M., Kantarjian, H., Konopleva, M., Korchin, B., Kaluarachchi, K., Bornmann, W., Duvvuri, S., Taegtmeyer, H., and Andreeff, M. (2010). Pharmacologic inhibition of fatty acid oxidation sensitizes human leukemia cells to apoptosis induction. J. Clin. Invest. *120*, 142–156. https://doi.org/10.1172/JCI38942.

53. Gugiatti, E., Tenca, C., Ravera, S., Fabbi, M., Ghiotto, F., Mazzarello, A.N., Bagnara, D., Reverberi, D., Zarcone, D., Cutrona, G., et al. (2018). A reversible carnitine palmitoyltransferase (CPT1) inhibitor offsets the proliferation of chronic lymphocytic leukemia cells. Haematologica *103*, e531–e536. https://doi.org/10.3324/haematol.2017.175414.

54. Fernandez-Marcos, P.J., and Auwerx, J. (2011). Regulation of PGC-1alpha, a nodal regulator of mitochondrial biogenesis. Am. J. Clin. Nutr. *93*, 884S–890S. https://doi.org/10.3945/ajcn.110.001917.

55. Handschin, C., and Spiegelman, B.M. (2006). Peroxisome proliferator-activated receptor gamma coactivator 1 coactivators, energy homeostasis, and metabolism. Endocr. Rev. *27*, 728–735. https://doi.org/10.1210/er.2006-0037.

56. Dimopoulos, N., Watson, M., Green, C., and Hundal, H.S. (2007). The PPARdelta agonist, GW501516, promotes fatty acid oxidation but has no direct effect on glucose utilisation or insulin sensitivity in rat L6 skeletal muscle cells. FEBS Lett. *581*, 4743–4748. https://doi.org/10.1016/j.febslet.2007.08.072.

57. Kalluri, R., and LeBleu, V.S. (2020). The biology, function, and biomedical applications of exosomes. Science *367*, eaau6977. https://doi.org/10.1126/science.aau6977.

58. Andreu, Z., and Yáñez-Mó, M. (2014). Tetraspanins in extracellular vesicle formation and function. Front. Immunol. *5*, 442. https://doi.org/10.3389/fimmu.2014.00442.

59. Cuesta-Geijo, M.Á., Chiappi, M., Galindo, I., Barrado-Gil, L., Muñoz-Moreno, R., Carrascosa, J.L., and Alonso, C. (2016). Cholesterol Flux Is Required for Endosomal Progression of African Swine Fever Virions during the Initial Establishment of Infection. J. Virol. *90*, 1534–1543. https://doi.org/10.1128/JVI.02694-15.

60. Israels, S.J., and McMillan-Ward, E.M. (2007). Platelet tetraspanin complexes and their association with lipid rafts. Thromb. Haemost. *98*, 1081–1087.

61. Kobayashi, T., Vischer, U.M., Rosnoblet, C., Lebrand, C., Lindsay, M., Parton, R.G., Kruithof, E.K., and Gruenberg, J. (2000). The tetraspanin CD63/lamp3 cycles between endocytic and secretory compartments in human endothelial cells. Mol. Biol. Cell *11*, 1829–1843. https://doi.org/10.1091/mbc.11.5.1829.

62. Silvie, O., Charrin, S., Billard, M., Franetich, J.F., Clark, K.L., van Gemert, G.J., Sauerwein, R.W., Dautry, F., Boucheix, C., Mazier, D., and Rubinstein, E. (2006). Cholesterol contributes to the organization of tetraspanin-enriched microdomains and to CD81-dependent infection by malaria sporozoites. J. Cell Sci. *119*, 1992–2002. https://doi.org/10.1242/jcs.02911.

63. Laine, R.F., Heil, H.S., Coelho, S., Nixon-Abell, J., Jimenez, A., Galgani, T., Stubb, A., Follain, G., Webster, S., Goyette, J., et al. (2022). High-fidelity 3D live-cell nanoscopy through data-driven enhanced super-resolution radial fluctuation. Preprint at bioRxiv. https://doi.org/10.1101/2022.04.07.487490.

64. Fortunato, D., Mladenović, D., Criscuoli, M., Loria, F., Veiman, K.L., Zocco, D., Koort, K., and Zarovni, N. (2021). Opportunities and Pitfalls of Fluorescent Labeling Methodologies for Extracellular Vesicle Profiling on High-Resolution Single-Particle Platforms. Int. J. Mol. Sci. *22*, 10510. https://doi.org/10.3390/ijms221910510.

65. Ho, T.T., Warr, M.R., Adelman, E.R., Lansinger, O.M., Flach, J., Verovskaya, E.V., Figueroa, M.E., and Passegué, E. (2017). Autophagy maintains the metabolism and function of young and old stem cells. Nature *543*, 205–210. https://doi.org/10.1038/nature21388.

66. Catalano, M., and O'Driscoll, L. (2020). Inhibiting extracellular vesicles formation and release: a review of EV inhibitors. J. Extracell. Vesicles *9*, 1703244. https://doi.org/10.1080/20013078.2019.1703244.

67. Ostrowski, M., Carmo, N.B., Krumeich, S., Fanget, I., Raposo, G., Savina, A., Moita, C.F., Schauer, K., Hume, A.N., Freitas, R.P., et al. (2010). Rab27a and Rab27b control different steps of the exosome secretion pathway. Nat. Cell Biol. *12*. 19–13. https://doi.org/10.1038/ncb2000.

68. Torres, L.S., Asada, N., Weiss, M.J., Trumpp, A., Suda, T., Scadden, D.T., and Ito, K. (2022). Recent advances in "sickle and niche" research - Tribute to Dr. Paul S Frenette. Stem Cell Rep. *17*, 1509–1535. https://doi.org/10.1016/j.stemcr.2022.06.004.

69. Goldberg, L.R. (2021). Extracellular Vesicles and Hematopoietic Stem Cell Aging. Arterioscler. Thromb. Vasc. Biol. *41*, e399–e416. https://doi.org/10.1161/ATVBAHA.120.314643.

70. Kulkarni, R., Bajaj, M., Ghode, S., Jalnapurkar, S., Limaye, L., and Kale, V.P. (2018). Intercellular Transfer of Microvesicles from Young Mesenchymal Stromal Cells Rejuvenates Aged Murine Hematopoietic Stem Cells. Stem Cell. *36*, 420–433. https://doi.org/10.1002/stem.2756.

71. Karnas, E., Sekuła-Stryjewska, M., Kmiotek-Wasylewska, K., Bobis-Wozowicz, S., Ryszawy, D., Sarna, M., Madeja, Z., and Zuba-Surma, E.K. (2021). Extracellular vesicles from human iPSCs enhance reconstitution capacity of cord blood-derived hematopoietic stem and progenitor cells. Leukemia *35*, 2964–2977. https://doi.org/10.1038/s41375-021-01325-y.

72. Bradshaw, P.C. (2019). Cytoplasmic and Mitochondrial NADPH-Coupled Redox Systems in the Regulation of Aging. Nutrients *11*, 504. https://doi.org/10.3390/nu11030504.

73. Fujimoto, M., Hayashi, T., and Su, T.P. (2012). The role of cholesterol in the association of endoplasmic reticulum membranes with mitochondria. Biochem. Biophys. Res. Commun. *417*, 635–639. https://doi.org/10.1016/j.bbrc.2011.12.022.

74. Luchsinger, L.L., de Almeida, M.J., Corrigan, D.J., Mumau, M., and Snoeck, H.W. (2016). Mitofusin 2 maintains haematopoietic stem cells with extensive lymphoid potential. Nature *529*, 528–531. https://doi.org/10.1038/nature16500.

75. Umemoto, T., Johansson, A., Ahmad, S.A.I., Hashimoto, M., Kubota, S., Kikuchi, K., Odaka, H., Era, T., Kurotaki, D., Sashida, G., and Suda, T. (2022). ATP citrate lyase controls hematopoietic stem cell fate and supports bone marrow regeneration. EMBO J. *41*, e109463. https://doi.org/10.15252/embj.2021109463.

76. Oguro, H. (2019). The Roles of Cholesterol and Its Metabolites in Normal and Malignant Hematopoiesis. Front. Endocrinol. *10*, 204. https://doi.org/10.3389/fendo.2019.00204.

77. Yang, E., Wang, X., Gong, Z., Yu, M., Wu, H., and Zhang, D. (2020). Exosome-mediated metabolic reprogramming: the emerging role in tumor microenvironment remodeling and its influence on cancer progression. Signal Transduct. Target. Ther. *5*, 242. https://doi.org/10.1038/s41392-020-00359-5.

78. Ratajczak, J., Miekus, K., Kucia, M., Zhang, J., Reca, R., Dvorak, P., and Ratajczak, M.Z. (2006). Embryonic stem cell-derived microvesicles reprogram hematopoietic progenitors: evidence for horizontal transfer of mRNA and protein delivery. Leukemia *20*, 847–856. https://doi.org/10.1038/sj.leu.2404132.

79. Gu, H., Chen, C., Hao, X., Wang, C., Zhang, X., Li, Z., Shao, H., Zeng, H., Yu, Z., Xie, L., et al. (2016). Sorting protein VPS33B regulates exosomal autocrine signaling to mediate hematopoiesis and leukemogenesis. J. Clin. Invest. *126*, 4537–4553. https://doi.org/10.1172/JCI87105.

80. Beckmann, J., Scheitza, S., Wernet, P., Fischer, J.C., and Giebel, B. (2007). Asymmetric cell division within the human hematopoietic stem and progenitor cell compartment: identification of asymmetrically segregating proteins. Blood *109*, 5494–5501. https://doi.org/10.1182/blood-2006-11-055921.

81. Hu, M., Lu, Y., Wang, S., Zhang, Z., Qi, Y., Chen, N., Shen, M., Chen, F., Chen, M., Yang, L., et al. (2022). CD63 acts as a functional marker in maintaining hematopoietic stem cell quiescence through supporting TGFbeta signaling in mice. Cell Death Differ. *29*, 178–191. https://doi.org/10.1038/s41418-021-00848-2.

82. Pinho, S., and Frenette, P.S. (2019). Haematopoietic stem cell activity and interactions with the niche. Nat. Rev. Mol. Cell Biol. *20*, 303–320. https://doi.org/10.1038/s41580-019-0103-9.

83. Asada, N., Kunisaki, Y., Pierce, H., Wang, Z., Fernandez, N.F., Birbrair, A., Ma'ayan, A., and Frenette, P.S. (2017). Differential cytokine contributions of perivascular haematopoietic stem cell niches. Nat. Cell Biol. *19*, 214–223. https://doi.org/10.1038/ncb3475.

84. Hurwitz, S.N., Jung, S.K., Kobulsky, D.R., Fazelinia, H., Spruce, L.A., Pérez, E.B., Groen, N., Mesaros, C., and Kurre, P. (2023). Neutral sphingomyelinase blockade enhances hematopoietic stem cell fitness through an integrated stress response. Blood *142*, 1708–1723. https://doi.org/10.1182/blood.2023022147.

85. Théry, C., Witwer, K.W., Aikawa, E., Alcaraz, M.J., Anderson, J.D., Andriantsitohaina, R., Antoniou, A., Arab, T., Archer, F., Atkin-Smith, G.K., et al. (2018). Minimal information for studies of extracellular vesicles 2018 (MISEV2018): a position statement of the International Society for Extracellular Vesicles and update of the MISEV2014 guidelines. J. Extracell. Vesicles *7*, 1535750. https://doi.org/10.1080/20013078.2018.1535750.

86. Webber, J.P., Spary, L.K., Sanders, A.J., Chowdhury, R., Jiang, W.G., Steadman, R., Wymant, J., Jones, A.T., Kynaston, H., Mason, M.D., et al. (2015). Differentiation of tumour-promoting stromal myofibroblasts by cancer exosomes. Oncogene *34*, 290–302. https://doi.org/10.1038/onc.2013.560.

87. Bobrie, A., Krumeich, S., Reyal, F., Recchi, C., Moita, L.F., Seabra, M.C., Ostrowski, M., and Théry, C. (2012). Rab27a supports exosome-dependent and -independent mechanisms that modify the tumor microenvironment and can promote tumor progression. Cancer Res. *72*, 4920–4930. https://doi.org/10.1158/0008-5472.CAN-12-0925.

88. Hoshino, A., Mita, Y., Okawa, Y., Ariyoshi, M., Iwai-Kanai, E., Ueyama, T., Ikeda, K., Ogata, T., and Matoba, S. (2013). Cytosolic p53 inhibits Parkin-mediated mitophagy and promotes mitochondrial dysfunction in the mouse heart. Nat. Commun. *4*, 2308. https://doi.org/10.1038/ncomms3308.

89. Nomura, M., Liu, J., Rovira, I.I., Gonzalez-Hurtado, E., Lee, J., Wolfgang, M.J., and Finkel, T. (2016). Fatty acid oxidation in macrophage polarization. Nat. Immunol. *17*, 216–217. https://doi.org/10.1038/ni.3366.

90. Méndez-Ferrer, S., Michurina, T.V., Ferraro, F., Mazloom, A.R., Macarthur, B.D., Lira, S.A., Scadden, D.T., Ma'ayan, A., Enikolopov, G.N., and Frenette, P.S. (2010). Mesenchymal and haematopoietic stem cells form a unique bone marrow niche. Nature *466*, 829–834. https://doi.org/10.1038/nature09262.

91. Painter, M.W., Davis, S., Hardy, R.R., Mathis, D., and Benoist, C.; Immunological Genome Project Consortium (2011). Transcriptomes of the B and T lineages compared by multiplatform microarray profiling. J. Immunol. *186*, 3047–3057. https://doi.org/10.4049/jimmunol.1002695.

92. Schindelin, J., Arganda-Carreras, I., Frise, E., Kaynig, V., Longair, M., Pietzsch, T., Preibisch, S., Rueden, C., Saalfeld, S., Schmid, B., et al. (2012). Fiji: an open-source platform for biological-image analysis. Nat. Methods *9*, 676–682. https://doi.org/10.1038/nmeth.2019.

93. Gustafsson, N., Culley, S., Ashdown, G., Owen, D.M., Pereira, P.M., and Henriques, R. (2016). Fast live-cell conventional fluorophore nanoscopy with ImageJ through super-resolution radial fluctuations. Nat. Commun. *7*, 12471. https://doi.org/10.1038/ncomms12471.

94. McQuin, C., Goodman, A., Chernyshev, V., Kamentsky, L., Cimini, B.A., Karhohs, K.W., Doan, M., Ding, L., Rafelski, S.M., Thirstrup, D., et al. (2018). CellProfiler 3.0: Next-generation image processing for biology. PLoS Biol. *16*, e2005970. https://doi.org/10.1371/journal.pbio.2005970.

95. Xia, J., Psychogios, N., Young, N., and Wishart, D.S. (2009). MetaboAnalyst: a web server for metabolomic data analysis and interpretation. Nucleic Acids Res. *37,* W652–W660. https://doi.org/10.1093/nar/gkp356.

96. Patterson, G.H., Knobel, S.M., Arkhammar, P., Thastrup, O., and Piston, D.W. (2000). Separation of the glucose-stimulated cytoplasmic and mitochondrial NAD(P)H responses in pancreatic islet beta cells. Proc. Natl. Acad. Sci. USA *97*, 5203–5207. https://doi.org/10.1073/pnas.090098797.

97. Ollion, J., Cochennec, J., Loll, F., Escudé, C., and Boudier, T. (2013). TANGO: a generic tool for high-throughput 3D image analysis for studying nuclear organization. Bioinformatics *29*, 1840–1841. https://doi.org/10.1093/bioinformatics/btt276.

98. Cardona, A., Saalfeld, S., Schindelin, J., Arganda-Carreras, I., Preibisch, S., Longair, M., Tomancak, P., Hartenstein, V., and Douglas, R.J. (2012). TrakEM2 software for neural circuit reconstruction. PLoS One *7*, e38011. https://doi.org/10.1371/journal.pone.0038011.

99. Corona, M.L., Hurbain, I., Raposo, G., and van Niel, G. (2023). Characterization of Extracellular Vesicles by Transmission Electron Microscopy and Immunolabeling Electron Microscopy. Methods Mol. Biol. *2668*, 33–43. https://doi.org/10.1007/978-1-0716-3203-1_4.

100. Yang, Y., Li, C.W., Chan, L.C., Wei, Y., Hsu, J.M., Xia, W., Cha, J.H., Hou, J., Hsu, J.L., Sun, L., and Hung, M.C. (2018). Exosomal PD-L1 harbors active defense function to suppress T cell killing of breast cancer cells and promote tumor growth. Cell Res. *28*, 862–864. https://doi.org/10.1038/s41422-018-0060-4.

101. Johnson, W.E., Li, C., and Rabinovic, A. (2007). Adjusting batch effects in microarray expression data using empirical Bayes methods. Biostatistics *8*, 118–127. https://doi.org/10.1093/biostatistics/kxj037.

102. Martini, P., Sales, G., Massa, M.S., Chiogna, M., and Romualdi, C. (2013). Along signal paths: an empirical gene set approach exploiting pathway topology. Nucleic Acids Res. *41*, e19. https://doi.org/10.1093/nar/gks866.

103. Calura, E., Martini, P., Sales, G., Beltrame, L., Chiorino, G., D'Incalci, M., Marchini, S., and Romualdi, C. (2014). Wiring miRNAs to pathways: a topological approach to integrate miRNA and mRNA expression profiles. Nucleic Acids Res. *42*, e96. https://doi.org/10.1093/nar/gku354.

104. Rider, M.A., Hurwitz, S.N., and Meckes, D.G., Jr. (2016). ExtraPEG: A Polyethylene Glycol-Based Method for Enrichment of Extracellular Vesicles. Sci. Rep. *6*, 23978. https://doi.org/10.1038/srep23978.

105. Parsons, M.E.M., McParland, D., Szklanna, P.B., Guang, M.H.Z., O'Connell, K., O'Connor, H.D., McGuigan, C., Ní Áinle, F., McCann, A., and Maguire, P.B. (2017). A Protocol for Improved Precision and Increased Confidence in Nanoparticle Tracking Analysis Concentration Measurements between 50 and 120 nm in Biological Fluids. Front. Cardiovasc. Med. *4*, 68. https://doi.org/10.3389/fcvm.2017.00068.

STAR★METHODS

KEY RESOURCES TABLE

REAGENT or RESOURCE	SOURCE	IDENTIFIER
Antibodies		
CD11b-biotin	BD Biosciences	Cat# 553782 ; RRID: AB_394773
CD19-biotin	BD Biosciences	Cat# 553784; RRID: AB_395048
CD45R/B220-biotin	BD Biosciences	Cat# 553086; RRID: AB_394615
CD4-biotin	BD Biosciences	Cat# 553045; RRID: AB_394581
NK-1.1-biotin	BD Biosciences	Cat# 553163; RRID: AB_394675
TER-119-biotin	BD Biosciences	Cat# 553672; RRID: AB_394985
CD117 (c-kit)-APC/CY7	Biolegend	Cat# 105826; RRID: AB_1626278
CD117 (c-kit)-PE	Biolegend	Cat# 105808; RRID: AB_313217
CD150 (SLAM)-PerCp/Cy5.5	Biolegend	Cat# 115922; RRID: AB_2303663
CD48-Pacific Blue	Biolegend	Cat# 103418; RRID:AB_756140
Ly6G/Ly6C (Gr-1)-biotin	Biolegend	Cat# 108404; RRID: AB_313369
CD127-biotin	eBioscience	Cat# 13-1271-85; RRID: AB_466588
CD135 (Flt3)-biotin	eBioscience	Cat# 13-1351-82; RRID: AB_466599
CD34-APC	eBioscience	Cat# 50-0341-82; RRID: AB_10596826
CD34-FITC	eBioscience	Cat# 11-0341-85; RRID: AB_465022
CD3e-biotin	eBioscience	Cat# 13-0031-85; RRID: AB_466320
CD48-APC	eBioscience	Cat# 17-0481-82; RRID: AB_469408
CD63-APC	Life Technologies	Cat# A15712; RRID: AB_2534492
CD8a-biotin	eBioscience	Cat# 13-0081-85; RRID: AB_466347
CD201 (EPCR)-APC	eBioscience	Cat# 17-2012-82; RRID: AB_10717805
Ly-6A/E (Sca-1)-PE/Cy7	eBioscience	Cat# 25-5981-81; RRID: AB_469668
Mouse IgM-biotin	eBioscience	Cat# 13-5790-85; RRID: AB_466676
Streptavidin-APC	eBioscience	Cat# 17-4317-82
Streptavidin-Pacific Blue	eBioscience	Cat# 48-4317-82
CD45-biotin	BD Biosciences	Cat# 553077; RRID: AB_394608
Streptavidin-PE	Biolegend	Cat# 405203
CD31-APC	Biolegend	Cat# 102409; RRID: AB_312905
CD45.1-PE	Biolegend	Cat# 110707; RRID: AB_313497
CD45.2-PE-Cy7	Biolegend	Cat# 109830; RRID: AB_1186098
CD3e-APC	Biolegend	Cat# 100312; RRID: AB_312677
B220-PacificBlue	Biolegend	Cat# 103227; RRID: AB_492876
CD11b-FITC	Ebioscience	Cat# 53-0112-82; RRID: AB_469901
Gr-1-FITC	Biolegend	Cat# 108405; RRID: AB_313371
CD63 magnetic beads	Thermo Fisher Scientific	Cat# 10606D
PE mouse anti-human CD63	eBioscience	Cat# 12-0639-42; RRID: AB_2572565
PerCP/Cyanine5.5 anti-human CD9	BioLegend	Cat# 312109; RRID: AB_2728251
Anti-CD63	Abcam	Cat# ab134045; RRID: AB_2800495
Anti-Farnesyl	Sigma-Aldrich	Cat# 341286
Anti- Ki-67 (D3B5)	Cell Signaling	Cat# 9129; RRID: AB_2687446
Goat anti-Rabbit IgG-Alexa Fluor 488	Thermo Fisher Scientific	Cat# A32731; RRID: AB_2633280
Goat anti-Rabbit IgG-Alexa Fluor 594	Thermo Fisher Scientific	Cat# A11037; RRID: AB_2534095
Chemicals, peptides, and recombinant proteins		
Animal-Free Recombinant Murine TPO	PeproTech	Cat# AF-315-14
BIBB 515	Cayman Chemical	CAS: 10010517

(*Continued on next page*)

Continued

REAGENT or RESOURCE	SOURCE	IDENTIFIER
Bovine Serum Albumin	Sigma-Aldrich	Cat# A4503
BMS-303141	Merk	Cat# SML0784; CAS: 943962-47-8
BTC	Merk	Cat# 115983; CAS: 2672-58-4
Etomoxir	Merk	Cat# E1905; CAS: 828934-41-4
FCCP (carbonilcyanide *p*-triflouromethoxy-phenylhydrazone)	Millipore-Sigma	Cat# C2920; CAS: 370-86-5
Fetal bovine serum exosome-depleted	Capricorn scientific	Cat# FBS-ED-12F
GW4869	Merk	Cat# D1692; CAS: 6823-69-4
GW-501516	Santa Cruz Biotechnology	Cat# sc-202642< CAS: 317318-70-0
Hydrogen peroxide (H_2O_2)	Millipore-Sigma	Cat# H1009; CAS: 7722-84-1
ITSX	Thermo Fisher Scientific	Cat# 51500056
Lovastatin	United State Pharmacopoea	Cat# 1370600 CAS: 73573-88-3
MethoCult GF M3434	STEMCELL Technologies	Cat# 03434
Methyl-beta-cyclodextrin (MBCD)	Millipore-Sigma	Cat# 332615; CAS: 128446-36-6
Rotenone	Cayman Chemical	Cat# 13995 CAS: 83-79-4
Poly(vinyl alcohol)	Sigma-Aldrich	Cat# 341584; CAS: 9002-89-5
Recombinant Murine SCF	PeproTech	Cat# 250-03
StemSpan™ SFEM	STEMCELL Technologies	Cat# 09600
Tetramethylrhodamine, Methyl Ester, Perchlorate (TMRM)	Thermo Fisher Scientific	Cat# T668
Verapamil	Millipore-Sigma	Cat# V4629; CAS: 152-11-4
Pyronin Y	Merk	Cat# 213519; CAS: 92-32-0
PEG 8000	Merk	Cat# 89510; CAS: 25322-68-3
PKH26	Sigma-Aldrich	Cat# MINI26-1KT
Critical commercial assays		
RNAeasy Mini kit	QIAGEN	Cat# 74104
Cholesterol Assay Kit (Cell based)	Abcam	Cat# ab133116
Total Cholesterol Assay Kits	Cell Biolabs	Cat# STA-384
NADP/NADPH-Glo	Promega	Cat# G9081
NAD/NADH-Glo	Promega	Cat# G9071
SPHERO™ Particle Size Standard Kit #PPS-6K	Spherotech	Cat# PPS-6K
Experimental models: Cell lines		
OP-9	ATCC	ATCC: CRL-2749
Deposited data		
Mendeley data	Source data	https://data.mendeley.com/preview/3g6snt5yzr?a=67b3935a-4810-4a22-af31-7336351b6dcf
MetaboLights	Raw metabolomic data	MTBLS6401
Experimental models: Organisms/strains		
B6.SJL-Ptprca Pepcb/BoyJ	The Jackson lab	JAX: 002014
B6N.Cg-Commd10Tg(Vav1-iCre)A2Kio/J	The Jackson lab	JAX: 008610
B6N.129(FVB)-Ppargc1atm2.1Brsp/J	The Jackson lab	JAX: 009666
C57BL/6	The Jackson lab	JAX: 000664
C57BL/6 Cpt2f/f	T. Finkel Lab, University of Pittsburgh Nomura et al.[89]	n.a.
Nes-*Gfp* transgenic mice	S. Frenette Lab, Albert Einstein College of Medicine Mendez-Ferrer et al.[90]	n.a.
Recombinant DNA		
pLKO-Tet-On-shRab27a	Yang et al.[91]	Addgene 120930
pUC57-TPNOX	Cracan et al.[30]	Addgene 87853

(*Continued on next page*)

Continued		
REAGENT or RESOURCE	SOURCE	IDENTIFIER
pUC57-mitoTPNOX	Cracan et al.[30]	Addgene 87854
Oligonucleotides		
Scf F- CCTCTCGCAATGCAAAGAAGG	This paper	N/A
Scf R- GAGGTCGGTAGCATATTTGGAAG	This paper	N/A
Msmo1 F- AAACAAAAGTGTTGGCGTGTTC	This paper	N/A
Msmo1 R- AAGCATTCTTAAAGGGCTCCTG	This paper	N/A
Tm7sf2 F- GTCGCGGCTTTACTGATCCT	This paper	N/A
Tm7sf2 R- CAGGCAGATAGGCCGGTAG	This paper	N/A
Hsd17b7 F- CCTCTCGCAATGCAAAGAAGG	This paper	N/A
Hsd17b7 R- GAGGTCGGTAGCATATTTGGAAG	This paper	N/A
ActB F- GGCTGTATTCCCCTCCATCG	This paper	N/A
ActB R- CCAGTTGGTAACAATGCCATGT	This paper	N/A
Software and algorithms		
GraphPad Prism	GraphPad	https://www.graphpad.com/
Fiji - ImageJ	Schindelin et al.[92]	Fiji (imagej.net)
NanoJ-eSRRF	Gustafsson et al.[93]	https://github.com/HenriquesLab/NanoJ-eSRRF
CellProfiler	McQuin et al.[94]	https://cellprofiler.org/
Graphite	Sales et al.[36]	Graphite Web (unipd.it)
FlowJo	BD	https://www.flowjo.com/
L-CALC	STEMCELL Technologies	https://www.stemcell.com/l-calc-software.html
Olympus - scanR	EVIDENT scientific	https://lifescience.evidentscientific.com.cn/en/video/scanr-product-overview/
Compound Discoverer 3.0	ThermoFisher Scientific	https://thermo.flexnetoperations.com/control/thmo/login
MetaboAnalyst	Xia et al.[95]	https://www.metaboanalyst.ca/
Izon Control Suite Software (V3.4)	Izon Science	https://support.izon.com/qnano-control-suite-software

RESOURCE AVAILABILITY

Lead contact

Further information and requests for resources and reagents (including mouse strains, cell lines and plasmids) should be directed to and will be fulfilled by the lead contact, Keisuke Ito (keisuke.ito@einsteinmed.edu).

Materials availability

This study did not generate new unique reagents.

Data and code availability

Source data have been deposited to Mendeley Data and are available at https://data.mendeley.com/preview/3g6snt5yzr?a=67b3935a-4810-4a22-af31-7336351b6dcf. The raw metabolomics data are deposited to MetaboLights (reference number MTBLS6401). Any additional information required to reanalyze the data reported in this paper is available from the lead contact upon request.

EXPERIMENTAL MODELS AND STUDY PARTICIPANT DETAILS

C57BL/6 mice (B6-CD45.2, or Ly5.2), B6N.Cg-Commd10Tg(Vav1-iCre)A2Kio/J (*Vav-iCre*), B6N.129(FVB)-Ppargc1atm2.1Brsp/J (*Ppargc1af/f*) and B6.SJL-Ptprca Pepcb/BoyJ (B6-CD45.1, or Ly5.1) were purchased from The Jackson Laboratory. C57BL/6 *Cpt2f/f* were kindly gifted by Dr. Finkel.[89] Nes-*Gfp* transgenic mice were kindly gifted by Dr. Frenette.[90] GW-501516 was administered at 5 mg per kg body weight per day by oral gavage.[7] All animal experiments were approved by the Institutional Animal Care and Use Committee of the Albert Einstein College of Medicine. All mice were 2–4 month old at the time of their utilization. Both male and female mice were used.

METHOD DETAILS

Flow cytometry and cell sorting

Bone marrow mononuclear cells (BMMNCs) were isolated by the flushing technique. Briefly, bone marrow from the femora and tibia was flushed in FACS buffer (PBS +2% FBS). After red blood cells lysis with ACK Lysing Buffer (Gibco), the bone marrow was filtered using 75mm cell-strainer cap (Falcon). After isolation, BMMNCs were incubated with the following mix of monoclonal antibodies against lineage: Ly6G/Ly6C (Gr-1)-biotin (Cat# 108404) from Biolegend; CD11b-biotin (Cat# BDB553309), CD19-biotin (Cat# BDB553784), CD45R/B220-biotin (Cat# BDB553086), CD4-biotin (Cat# BDB553782), NK-1.1-biotin (Cat# BDB553163) and TER-119-biotin (Cat# BDB553672) from Fisher Scientific; CD135 (Flt3)-biotin (Cat# 13-1351-82) from eBioscience; CD127-biotin (Cat# 13-1271-85), CD3e-biotin (Cat# 13-0031-85), CD8a-biotin (Cat# 13-0081-85), Mouse IgM-biotin (Cat# 13-5790-85) from Life Technologies, and then resuspended in 2% FBS-PBS for 30 min in ice. Lineage antibody staining was followed by incubation with antibody mix for the following HSPC markers: CD117 (c-kit)-APC/CY7 (Cat# 105826) or CD117 (c-kit)-PE (Cat# 105808), CD150 (SLAM)-PerCp/Cy5.5 (Cat# 115922), CD48-Pacific Blue (Cat# 103418) from Biolegend; CD201(EPCR)- APC (17-2012-82), CD34-APC (Cat# 50-0341-82) or CD34-FITC (Cat# 11-0341-85), CD48-APC (Cat# 17-0481-82), Ly-6A/E (Sca-1)-PE/Cy7 (Cat# 25-5981-81), Streptavidin-APC (Cat# 17-4317-82) or Streptavidin-Pacific Blue (Cat# 48-4317-82) from eBioscience; resuspended in 2% FBS-PBS for 30 min in ice. All antibodies were used at a 1:100 dilution.

Samples were acquired on an LSR II flow cytometer (Becton Dickinson) then data was analyzed using FlowJo 10 (Becton Dickinson). For Pyronin Y, freshly isolated BM stained for surface markers were stained with Pyronin Y 1 μM (Sigma-Aldrich) at 37°C for 20 min and analyzed by flow cytometry. For cell sorting, BMMNCs stained with antibody mix were sorted directly into StemSpan SFEM (STEMCELL Technologies, Cat# 09600). Stem and progenitors cell fractions were isolated from lineage-depleted samples, as necessary. Cell sorting of $CD34^-$ HSC was performed on a BD FACSARIA II (Becton Dickinson). To sort $NAD(P)H^{Hi}$ versus $NAD(P)H^{Lo}$ $CD34^-$ HSC were sorted using MoFlo XDP (Beckman Coulter). Briefly, BMMNCs stained for surface markers were subdivided into two aliquots then incubated for 5 min at 37°C in 2% FBS-PBS in presence or absence of FCCP 1μM. To ensure the consistency of our strategy, we confirmed that this gating process identified <2% of FCCP-exposed $CD34^-$ HSCs as $NAD(P)H^{Hi}$ (Figures 1H and S2A), while ~60% of untreated $CD34^-$ HSCs were included in the $NAD(P)H^{Hi}$ gate.

For MSC sorting, BM primary cells were isolated from femurs and tibia of Nes-*Gfp* transgenic mice. BM were crushed and digested with 2 mg/mL Collagenase type IV (Gibco, 17104-019) and 4 mg/mL Dispase (Gibco, 17105-041) in HBSS (Gibco) for 30 min at 37°C, following erythrocyte lysis. For flow cytometry sorting, cells were stained and enriched by immunomagnetic depletion using anti-biotin magnetic beads (Miltenyi Biotec) binding CD45-biotin (BD Biosciences, 553077) and Ter119-biotin (BD Biosciences, 553672), according to the manufacturer's recommendations. Cells were stained by Streptavidin-PE (Biolegend, 405203), CD31-APC (Biolegend, 102409), and sorted on a FACSAria (BD) to >95% purity using Nes-*Gfp* as MSC marker.[90]

NAD(P)H analysis by flow cytometry

BMMNCs were isolated and stained for surface markers as described above. After staining, samples were subdivided in 3–5 fractions, each of them was incubated for 5 min at 37°C in 2% FBS-PBS in presence of FCCP 1μM, or H_2O_2 100 μM or rotenone 100 nM. After incubation, samples were recorded at LSRII, NAD(P)H autofluorescence was detected in the Indo-Violet channel (excitation laser at 350 nm, band-pass emission 450/50 nm). When indicated, samples exposed with FCCP or H_2O_2 were eventually incubated with H_2O_2 100μM or rotenone 100nM (respectively) at 37°C for additional 5 min then acquired at LSRII. To compensate for artifact related to cell size, autofluorescence intensity was normalized on FSC-A values, then scaled by multiplying for 10^4. This index was utilized as a reporter of NAD(P)H concentration (Figure S1D). The use of size calibration beads (SPHERO Particle Size Standard Kit #PPS-6K, Spherotech, Lake Forest, IL, USA) confirms that the FSC-A can be used as a readout of cell size.

HSCP culture conditions

Sorted HSC or KSL were cultured in StemSpan SFEM (STEMCELL Technologies, Cat# 09600) supplemented with SCF (PeproTech, Cat# 250-03) and TPO (PeproTech, Cat# AF-315-14) at 50 ng/mL unless otherwise described. According to the experimental need, the media could be supplemented with one of the following chemicals: Etomoxir 10 μM (Merk, #Cat E1905), Lovastatin 37.5 nM (United State Pharmacopoea, #Cat 1370600), GW4869 10 μM (Merk, #Cat D1692), GW501516 0.1 μM (Santa Cruz Biotechnology, #Cat sc-202642), BIBB 515 12.5 μM (Cayman Chemical, #Cat 10010517), BTC 5 mM (Merk, #Cat 115983), BMS-303141 1 mM (Merk, #Cat SML0784), MBCD 1.5mM (Sigma- Aldrich, #Cat 332615). For media testing (Figure S5L-S5N) sorted $CD34^-$ KSL were cultured with a handmade media adapted from.[46] Briefly the media was composed of F12, 1% ITSX, 1% (Thermo Fisher Scientific, Cat# 51500056), 10 mM HEPES, 1% P/S/G. This base media was further supplemented with bovine serum albumin (1% or 0.1%; Sigma-Aldrich, Cat# A4503), or poly(vinyl alcohol) 0.1% (Sigma-Aldrich, Cat# 341584), or exosome free-FBS 1% (Capricorn scientific, Cat# FBS-ED-12F), and SCF and TPO (50 ng/mL or 1 ng/mL).

Imaging of mitochondrial markers

Sorted cells were centrifuged at 400 g for 3 min at 4°C, resuspended in 30 μl of StemSpan SFEM, then seeded on a Lab-Tek II Chamber Slide (Thermo Fisher Scientific, Cat # 154534PK) coated with Retronectin (Takahara Bio, Cat# T100B), stained with TMRM 2 nM, and incubated for 60 min to let cells adhere.

Each cell was acquired on a Delta Vision Core (GE Healthcare Life Sciences) epifluorescence microscope equipped with a 60X oil immersion lens (NA 1.4). The nicotinamide moiety of NADH absorbs light at approximately 340 nm, and emits fluorescence at 460 nm.[96] The intensity of this fluorescence reflects NADH and/or NADPH (cumulatively referred to as NAD(P)H hereafter) and it was collected using excitation filter 377/50nm and emission filter 447/60 nm. For NAD(P)H analysis in Figure S7J, single planes were acquired. After flat field correction and background subtraction, the average intensity of NAD(P)H for each cell was collected. For 3D imaging in Figures 1C, 1H, 2A, 2B, 5F, S2J, S6B, and S6E z stack were acquired with a z spacing of 0.3 μm and pixel size of 107nm. After acquisition, stacks were reconstructed by digital deconvolution using the Richardson-Lucy algorithm implemented in the DeconvolutionLab2 plugin available for Fiji.[92] PSFs were manually measured by imaging PS-Speck Microscope Point Source Kit (Thermo Fisher Scientific, Cat# P7220).

After deconvolution, TMRM and Autofluorescence signals were segmented to identify mitochondria using a custom macro for Fiji. Briefly, to compensate for variation in expression levels, the histogram was stretched setting a maximal value for the top 0.1% of the original values. TMRM signal was emphasized by a 3D Top Hat filter (kernel 8 × 8 × 2 pixel), then thresholded using Yen algorithm. Segmentation objects were identified and measured for fluorescence intensities and shape using the 3D suite.[97] Representative image renderings were obtained by Fiji.

3D imaging of mitochondrial NAD(P)H symmetry between daughter cells

Single CD34$^-$ HSC were sorted and cultured as above mentioned. At 24 h after sorting, cells were visually inspected on an hourly basis for the occurrence of first division. Daughter cells were then moved to a RetroNectin-coated 35 mm glass bottom dish (Thermo Fisher Scientific, Cat# 150680), resuspended in 50 μL of StemSpan SFEM media supplemented with TMRM 2 nM and verapamil 50 μM. After 60 min of incubation 3D images were acquired, processed, and quantified as previously described. Average autofluorescence intensities for each mitochondrial particle were grouped for each daughter and compared with the values obtained from the paired daughter by Mann-Whitney U test. This offered a statistical comparison of mitochondrial autofluorescence distribution between paired daughters. Those pairs whose test provided a p value <0.05 were considered the result of an asymmetric segregation. The remaining were labeled symmetric. Those symmetric paired daughters whose median NAD(P)H intensity was above the median value of the whole dataset were considered symmetric high, on opposite, those symmetric paired daughters whose median NAD(P)H intensity was below the median value of the whole dataset were considered symmetric low (Figure S3A). The proportion of division between the genetic background described in Figure 5F was evaluated for statistical significance using χ^2 test.

Live NAD(P)H imaging during HSC first division

For NAD(P)H imaging in Figures 2C and 2D, and 3B-3D CD34$^-$ HSC were sorted, and culture as described above. At 24 h from isolation, cells were imaged on a Delta Vision Core using a 40x/1.35 oil immersion lens (UAPON40XO340-2, Olympus) under controlled environmental conditions (temperature at 37°C and CO2 at 5%). Images were acquired every ~40 min to minimize toxicity, for approximately 20 h. For every time point brightfield images were acquired to correct focus drifts. Images were corrected for shading and background, then cell divisions were manually tracked. NAD(P)H images were thresholded to collect only mitochondrial signal then average intensity was collected per each cell at each time point. Image processing and quantitation was obtained via FIJI software.[92] The NAD(P)H intensity of each tracked daughter and its related mother was compared by 1-way ANOVA. Divisions where only one daughter was significantly different from the mother was classified as asymmetric. Those divisions with both daughters significantly different from mother were classified as symmetric low, and the remaining division were classified as symmetric high.

Enzymatic NADH and NADPH assay

4000-5000 CD34$^-$ and CD34$^+$ HSC were sorted as aforementioned. Samples were centrifuged at 400g for 3 min, deprived of the supernatant, then washed once in ice-cold PBS. After washing samples were split into two parts, and one exposed to FCCP 1μM, NADPH and NADH were analyzed using the NADP/NADPH-Glo or NAD/NADH-Glo enzymatical kit (Promega, Cat# G9081, and Cat# G9071) as described by the manufacturer. Final luminometric readings were normalized on the number of cells sorted for each sample.

FLIM analysis

Images were acquired using a Leica TCS SP8 confocal microscope equipped with a tunable (680–1300 nm) femtosecond laser (InSight Deep See; Spectra-Physics) and an oil-immersion 40× objective (NA 1.3). TPEF images of the TMRM signal (1024 x 1024 pixels, 290.6 × 290.6 μm) from the fractions of interest were acquired at 720 nm excitation and 624 ± 20 nm emission ranges. Location co-registered NAD(P)H lifetime data were then acquired at 720 nm excitation and 460 ± 25 nm emission ranges with 2 min integration time (512 x 512 pixels) using a Picoquant Picoharp 300 time-correlated single photon counter and SymPhoTime analysis software. A combination of two-dimensional (2D) discrete Fourier transform and power spectral density (PSD) methods were applied on binarized images to segment out the whole cell regions.[27] Roundness (4*pi*area/perimeter2) of each segmented object was calculated and only the ones that above 0.6 were considered as cells to avoid taking debris or cell fragments into account. Afterward, for each cell, a three-level global Otsu's threshold was applied on the TMRM intensity images, and the pixels above the second threshold level were considered as mitochondria regions. Binary masks for whole cell region and mitochondria region were then saved for the following lifetime analyses. FLIMJ (ImageJ plugin) and MATLAB were used for lifetime analysis. A kernel size of four and an MLE (maximum likelihood estimation) noise model were used for pixel-wised 2-component lifetime curve fittings in the FLIMJ. The

resultant longer lifetime τ bound maps were calculated and exported. The pixel-wise NADPH/NADH ratio values were calculated based on method previously published.[25] For each cell, the averaged NADPH/NADH ratio values from all pixels in the mitochondria and whole cell regions were calculated in MATLAB based on the corresponding segmented binary masks.

Transmission electron microscopy

For mitochondrial analysis, 5000 sorted stem and progenitor cells were fixed in 2.5% glutaraldehyde, 2% paraformaldehyde in sodium cacodylate buffer 0.1 M, pH 7.4 for 3 h at 4°C. Samples were post-fixed in 1.0% aqueous osmium tetroxide (pH 7.4) followed by 1% uranyl acetate, dehydrated in a graded series of ethanol, and embedded in Lx112 resin (LADD Research Industries). Ultrathin (80nm) sections were cut on a Leica UC7, contrasted with uranyl acetate followed by lead citrate, and viewed on a JEOL 1200EX transmission electron microscope (Jeol Ltd.) at 80 kV. Images were manually segmented by the TrakEM2 plugin available on Fiji.[98]

For isolated EVs. EVs were deposited on carbonated grids, fixed in 2% PFA and stained with a contrasting solution of methyl-cellulose – as reported by Corona M.L. and colleagues.[99] Samples were then imaged with a TEM Zeiss EM 910 microscope (Zeiss).

Competitive reconstitution assay

Sorted HSC fractions from Ly5.2 donor were transplanted into lethally irradiated Ly5.1 congenic mice in competition with BMMNC. Reconstitution of donor (Ly5.2) cells and repopulation of donor myeloid and lymphoid cells were monitored by staining blood cells with antibodies against CD45.1-PE (Biolegend, Cat# 110707), CD45.2-PE-Cy7 (Biolegend, Cat# 109830), CD3e-APC (for T cell, Biolegend, Cat# 100312), B220-PacificBlue (Biolegend, Cat# 560472), CD11b-FITC and Gr-1-FITC (for myeloid cells, Ebioscience, Cat# 53-0112-82, and Biolegend, Cat# 108405 respectively). Analysis of chimerism in HSPC and fully differentiated hematopoietic cells in the bone marrow was obtained at 24 weeks after BMT. Isolation, staining and analysis of BMMNC at this stage was obtained as described in the 'flow cytometry and cell sorting' section.

To assess the roles of mitochondrial NADPH in a transplantation setting (Figure 1M), KSL (Ly5.2) cells were infected with mitoTPNOX, TPNOX or vector control. After puromycin selection, the infected 1000 KSL cells were transplanted into the irradiated recipient mice (Ly5.2) with $4x10^5$ competitor BMMNCs (Ly5.1). Then after 3 weeks after transplantation, mice were kept with Doxycycline (1% in 5% sucrose water) to induce transgene expression. In some experiments, donor contribution in the immature hematopoietic lineages was also evaluated. For the serial transplantation assay, donor-derived cells were collected from recipient mice 6 months after BMT and transplanted into the recipient mice.[6,7]

To assess EV functionality *in vivo* (Figure 6G), 125 sorted $CD34^-$HSC (Ly5.2) were cultured *in vitro* in StemSpan SFEM media supplemented with SCF and TPO (both at 50 ng/mL). Immediately after sorting, cells were supplemented with a bolus of HSC-derived EV (+HSC-EV). After 24 h of culture a second bolus of HSC-derived EV was administered to the same cultured HSC. Each bolus contained $0.4x10^9$ EV resuspended in 10 μL of filtered PBS, so to have approximately $1.5x10^6$ EV per HSC. In parallel, a second group of HSCs were treated with the same volume of filtered PBS free from EV (vehicle). After 48 h from sorting the culture of donor cells was split into 5 parts, and each of them (estimated 45 donor cells) transplanted into one lethally irradiated Ly5.1 recipient mouse together with $4x10^5$ competitor BMMNCs (Ly5.1).

To confirm *in vivo* the effect of the inhibition of EV formation on HSC function (Figure 6I), we used a Doxycycline inducible shRNA for Rab27a. Sorted FKSL (Ly5.2) cells were cultured in StemSpan SFEM media supplemented with SCF and TPO (both at 50 ng/mL) and infected with shRab27a inducible lentivirus (diluted 1:500). After 48 h of G418 (1 mg/ml) selection, 2000 live FKSL/mouse were transplanted in lethality irradiated recipient mice in competition with $1x10^6$ BMMNCs (Ly5.1). After 2 weeks from BMT, mice were kept with 1% Doxycycline to induce transgene expression.

Lentiviral particle production and infection

pUC57-TPNOX and pUC57-mitoTPNOX were gifted from Vamsi Mootha (Addgene plasmid # 87853; http://n2t.net/addgene:87853; RRID:Addgene_87853 and plasmid # 87854; http://n2t.net/addgene:87854; RRID:Addgene_87854).[30] For expression in mammalian cells synthetic TPNOX and mitoTPNOX genes were subcloned into a pLVX-TetOne vector (Clontech, Cat# 631844) using BamHI and AgeI restriction sites. pLKO-Tet-On-shRab27a was a gift from Mien-Chie Hung (Addgene plasmid # 120930; http://n2t.net/addgene:120930; RRID:Addgene_120930).[100]

For particles production, $5 x10^6$ HEK293T cells were seeded in a 10 cm dish 24 h before transfection and cultured in DMEM medium. Cells were then transfected with 3 μg of VSVG, 5 μg of pMDL, 2.5 μg of pRev, and 10 μg of Transfer Plasmid with 30 μL of lipofectamine 2000 (Thermo Fisher Scientific, Cat# 11668019). At 24 h after transfection media was refreshed and supplemented with sodium butyrate 1mM. At 24 h after media change, the lentivirus-enriched media was collected and filtered through a 0.45 μM filter and stored at −80°C. the procedure as repeated twice.

Collected media was ultracentrifuged at 90000 x g at 4°C in an SW40 Ti rotor (Beckman Coulter, Cat# 331301) for 90 min. After spinning, the supernatant was discarded, and the pellet gently resuspended in 300 μL of PBS for 16 h at 4°C upon gentle shaking. Lentiviral particle batches were all stored at −80°C.

Optimal infection was experimentally determined for each lentiviral batch. 1000 FKSL cells were sorted into StemSpan SFEM and infected with 50; 25; 12.5; or 6.12 μL of lentiviral preparation. At 24 h after infection cell toxicity was determined by trypan blue incorporation. The maximum amount of lentiviral preparation with minimal toxicity was chosen for subsequent experiments. Infected cells used then selected with puromycin (1 μg/mL) or G418 (1 mg/mL) for 48h before BMT.

Colony-forming assays

Frequencies of LTC-ICs were calculated using a limiting-dilution method (maximum likelihood from the proportion of negative wells measured for each input dilution of cells assessed). In each experiment, at least 12 (LTC-IC) replicates of each dilution were performed, and a split-plot analysis of variance was used to investigate the difference between the two conditions. The analysis was performed using L-CALC software (STEMCELL Technologies, https://www.stemcell.com/l-calc-software.html). 12.5 μM BIBB 515 and 1.5mM MBCD (Sigma- Aldrich, 332615, 2 h exposure/week) was added to the media where indicated.

The colony formation assay was performed using MethoCult GF M3434 (STEMCELL Technologies, Cat# 03434) according to the manufacturer's instructions. Briefly, Lin–Sca-1+c-Kit+ cells (300 cells/plate, triplicate culture) were sorted and seeded into methylcellulose-based medium. Colonies were counted under microscope after 7 days incubation at 37C°, 5% CO_2. For replating assay with infected cells, sorted KSL were seeded in StemSpan SFEM to run infection and selection as described above before seeding into MethoCult GF M3434.Where indicated liquid or semisolid media were supplemented with reagents to induce Tet-On system (Dox 300 ng/mL) or manipulating cholesterol or exosome biogenesis.

Paired daughter cell assays

Single $CD34^-$ HSC were sorted and cultured to track first division as described above. Daughter cells derived from a single parent cell were separated and were subjected to the competitive transplantation assay.[6,7,31] After initial division, daughter cells from the same parent cell were separated, and NAD(P)H intensity was determined by fluorescence microscopy. After checking NAD(P)H intensity, a single daughter cell (Ly5.2) was transplanted into lethally irradiated recipient mice (Ly5.1) in a competitive assay. Donor chimerism was analyzed periodically. Long-term repopulation was achieved when more than 1% of the contribution in the peripheral blood of recipient mice was observed at the indicated time after transplantation.

Identification of NADPH dependent pathways

Initially, all mouse pathways containing NADPH (CHEBI: 16474; 57783; 77177; 77312) were collected from the Reactome database.[33] Topological pathway analysis was used to analyze the 77 collected NADPH pathways and compare the gene expression in ST and LT-HSCs. For this purpose, 3 public expression datasets were collected and re-analyzed (GSE94663,[34] GSE77098,[35] GSE15907[91]). Datasets were chosen by similarity of sample preparation. Only genes common to all 3 datasets were considered, with a resulting matrix of 17592 genes of which 3737 displayed significant variations. Gene expression was corrected to avoid batch effects using the ComBat method.[101]

Normalized expression matrix was used to screen the NADPH pathways using Clipper methods, (details in[102];[103]) and protein-metabolite Graphite networks[36] modified to retain NADPH metabolites in pathway-derived graphs. The results of this analysis were *(i)* a new pathway (represented in Figures 3C and S4C), obtained by merging all the chains of reactions involving NADPH that are differentially regulated between the two class of samples ($CD34^+$ and $CD34^-$), and *(ii)* a rank of the studied chains of reactions utilizing their clipper max score (Figure 3B). Differentially expressed genes were identified with the Samr package in R software once the data were normalized and mapped on the network with different node colors.

Metabolomic analysis

10000 to 20000 NAD(P)H^{Hi} and NAD(P)H^{Lo} $CD34^-$ HSC were sorted directly into 500 μL 80% ice-cold methanol supplemented with 13C-labeled cholesterol (400nM 23,24,25,26,27-13C5-cholesterol, Cambridge Isotope Laboratories, Cat# CLM-9587). Polar and non-polar metabolites were extracted using methanol-chloroform phase separation.

For untargeted metabolomics analysis, polar phases were dried under nitrogen gas, resuspended in 120 μL 70% acetonitrile in water containing 2.5 mM of an internal standard (13C-, 15N-labeled amino acid mix; Cambridge Isotope Laboratories, Cat# CLM-9587), transferred to glass vial with microinserts, re-dried and finally resuspended in 25 μL 70% acetonitrile in water. Samples were run on a ThermoFisher Q-Exactive Orbitrap mass spectrometer equipped with Zic-pHILIC column (150 × 2.1 mm, 5 μm; Merck). A volume of 5 μL was injected and metabolites were monitored in full-scan, polarity-switching, mode (0–45 min, resolution 70,000, AGC target $3x10^6$, m/z range 66.7–1000). Mobile phase A for chromatography consisted of 20 mM ammonium carbonate, 0.1% ammonium hydroxide, in water and mobile phase B of 97% acetonitrile in water. A pooled sample was created from all samples and used for MS/MS runs. Metabolite measurements were normalized to the internal 13C/15N-labelled amino acid standard. Data were processed with Compound Discoverer 3.0 (ThermoFisher Scientific), among all detected compounds (2965), 100 were identified based on their mass spectra using the mzCloud database. Another 643 could be putatively identified using their molecular weight by searching the Human Metabolome database and Kyoto Encyclopedia of Genes and Genomes (KEGG) Compound database (Table S1). The metabolomics data were then further analyzed using the MetaboAnalyst software. Statistically, 32 compounds differed significantly between the groups (t-test, $p < 0.01$; Table S2).

For sterol analysis, the non-polar phases were dried under nitrogen gas and resuspended in 500 μL transesterification solution (methanol:acetyl chloride in a 9:1 ratio). 300 μL hexane was added, samples were vortexed and incubated at 95°C for 10 min. Samples were then supplemented with 1 mL water and 500 μL hexane, vortexed for 1 min and centrifuged at 14,000 x g for 15 min. The upper phase was transferred in a glass vial, dried under nitrogen gas, resuspended in 500 μL of −20°C chloroform, vortexed for 1 min and centrifuged. The bottom phase was then transferred to a new glass vial, and samples were extracted in chloroform a second time and re-dried. Samples were finally resuspended in 25 μL hexane to which 25 μL derivatization agent (N-Methyl-N-(trimethylsilyl) trifluoroacetamide +1% trimethylchlorosilane) was added, vortexed for 1 min and incubated at 80°C for 40 min. Samples were

transferred to glass inserts and analyzed on a Q-Exactive mass spectrometer (Thermo Fisher Scientific) equipped with an Agilent DB-5MS 30m, 0.25mm, 0.25μm column. Injection parameters: automatic injection, 1 μL, 300°C, splitless for 1.5 min before purge at 50 mL/min. Gas chromatography parameters: oven at 60°C for 5 min, then to 300 °C at 16 °C/min, final temperature for 30 min; column in constant flow mode at 1 mL/min, all transfer lines at 350°C. Mass spectrometry parameters: EI + ion source at 350°C, full MS, 60,000 resolution, AGC target 1e6, autoIT, scan range 66.7–1000 m/z, 7.5 min solvent delay. Data were analyzed in Compound Discoverer (version 3.0) and normalized to the 13C-labeled cholesterol internal standard. Of the sterols identified, only those specific to animal cells and detectable in all replicates were kept for analysis.

Filipin staining

Sorted NAD(P)H^{Hi} and NAD(P)H^{Lo} CD34^{-} cells were centrifuged at 400 g for 3 min at 4°C, resuspended in 30 μl of StemSpan SFEM then seeded on Lab-Tek II Chamber Slide (Thermo Fisher Scientific, Cat# 154526) coated with Fibronectin (Sigma-Aldrich, Cat# F1141) and incubated for 30 min to let cells adhere. After incubation cells were fixed and stained with filipin according to the Cholesterol Assay Kit (Cell based) (Abcam, Cat# ab133116) protocol. Stained cells were mounted in freshly prepared mounting media and imaged using a ZEISS AXIO examiner D1 microscope (Zeiss) equipped with a 40× oil Plan-APOCHROMAT objective and a Coolsnap HQ2 camera (Photometrics). Fluorescence detection was performed using a conventional DAPI filter set as recommended by the manufacturer (excitation filter 377/50nm and emission filter 447/60 nm). Images were processed and analyzed by CellProfiler (https://cellprofiler.org/)[94] using a customized pipeline. Briefly, images were subtracted from the background, segmented via the Otsu algorithm, then average intensity was collected for each cell per field of view and used as readout of cholesterol content.

Enzymatic cholesterol analysis

2000-3000 sorted NAD(P)H^{Hi} and NAD(P)H^{Lo} CD34^{-} cells were centrifuged at 400 G for 3 min at 4°C, then washed one time in ice-cold PBS. Subsequently, cholesterol was extracted and detected using the Total Cholesterol Assay Kits (Cell Biolabs, Cat# STA-384) according to manufacturer instructions. Final fluorescence reading was normalized based on the number of cells sorted for each sample.

Cholesterol enrichment

To force elevation of cholesterol in HSC plasma membrane, a cholesterol saturated MBCD (MBCD:chol) was prepared as following: MBCD 5 mM was solved in StemSpan SFEM media then incubated with cholesterol at a molar ratio 10:1 for 24 h at 37°C. Sorted HSCs were incubated with MBCD:chol for 60 min at 37°C then washed twice with StemSpan SFEM.

RT-qPCR

RNA from HSCs sorted from two-month-old mouse bone marrow were isolated using Qiagen RNeasy Kit and subjected to cDNA synthesis using Superscript III First-Strand synthesis system (Invitrogen, Cat# 18080051) or QuantiNova Reverse Transcription Kit (Qiagen, Cat# 205413). Real time quantitative PCR for *Slc25a1*, *Cpt1a*, *Ndufv1*, and *ActB* was performed using TaqMan Assay Mix (Applied Biosystems, Cat # 4304437) in QuantStudio 6 Flex Real-Time PCR with the dedicated Taqman probes (*Slc25a1:* Mm00467666_m1; *Cpt1a*: Mm01231183_m1; *Ndufv1:* Mm00504941_m1; *ActB:* Mm02619580_g1). Real time quantitative PCR for *Hsd17b7*, *Msmo1*, *Tm7sf2*, *Scf* and *ActB* was performed using Quantinova SYBR Green PCR Kit (Qiagen, Cat# 208056) in a Rotor-Gene Q (Qiagen, Cat# 9001862) using the following oligonucleotides.

Gene	Sequences
Scf	F- CCTCTCGCAATGCAAAGAAGG R- GAGGTCGGTAGCATATTTGGAAG
Msmo1	F- AAACAAAAGTGTTGGCGTGTTC R- AAGCATTCTTAAAGGGCTCCTG
Tm7sf2	F- GTCGCGGCTTTACTGATCCT R- CAGGCAGATAGGCCGGTAG
Hsd17b7	F- CCTCTCGCAATGCAAAGAAGG R- GAGGTCGGTAGCATATTTGGAAG
ActB	F- GGCTGTATTCCCCTCCATCG R- CCAGTTGGTAACAATGCCATGT

The PCR profile included a 10 min, 95°C hot-start to activate the Taq polymerase, followed by 40 cycles of a two-step program: 15 s at 95°C (denaturation) and 60 s at 60°C (annealing and extension). Relative gene expression level was analyzed by comparative Ct method and was normalized to *ActB*, as mentioned in the figure legends.

EVs isolation

3000 HSC or FKSL or Lin^{-} Nestin^{+} mesenchymal stem cells were sorted and cultured in StemSpan SFEM (STEMCELL Technologies) supplemented with 50 ng/mL stem cell factor (PeproTech, Cat# 250-03) and 50 ng/mL thrombopoietin (PeproTech, Cat# AF-315-14)

48 h. EVs were isolated by a modified PEG based method. EV-enriched media were exposed to 8% PEG 8000 (Merk, Cat# 89510) at 4°C for 24 h, then EVs were centrifuged at 3214 g for 1 h at 4°C. Supernatant was discarded and EV pellet resuspended in 30 μL of particle-free PBS.[104]

Tunable resistive pulse sensing (TRPS)

EVs concentration and size distribution were assessed using a qNano instrument (Izon Science) equipped with an NP150 nanopore (70–420 nm). 35 μL of each sample were loaded in the upper fluid cell, and voltage, pressure and stretch of the system were adjusted accordingly. TRPS (Tunable resistive pulse sensing) measurements as well as data analysis were performed with the Izon Control Suite Software (V3.4).

Nanoparticle tracking analysis

Nanoparticle tracking analysis (NTA) uses laser light scattering and Brownian motion to determine EVs size and concentration. This allows determining the size of particles in a suspension that flows through a focused laser beam. The light scattered by individual particles is recorded over time to visualize and track their movement. The mean square displacement for each particle along its track allows to calculate individual particle sizes using the Stokes-Einstein equation.[105] Measurement of particle size and particle size distribution was performed with Nanosight NS300 (Malvern) instrument equipped with a 488 nm laser. All samples were diluted in filtered PBS to a final volume of 1 mL. Ideal measurement concentrations were found by pre-testing the ideal particle per frame value (20–100 particles/frame). For each measurement, four to five 1-min videos were captured under temperature 25°C and syringe pump speed 30. Data are represented as averaged finite track length adjustment (FTLA) concentration/size.

EV immunomagnetic isolation and flow cytometry

35 μL of EVs suspension was incubated with CD63 magnetic beads (Thermo Fisher Scientific, Cat# 10606D). Isolated CD63-positive EVs were then labeled with an anti-CD63 monoclonal antibody (PE mouse anti-human CD63; eBioscience, Cat# 12-0639-42) or anti-CD9 monoclonal antibody (PerCP/Cyanine5.5 anti-human CD9, BioLegend, Cat# 312109). Negative control was performed by staining PBS (vehicle) instead of EVs. Flow cytometric experiments were conducted with Attune NxT Acoustic Focusing Cytometer (Life Technologies), and data were analyzed using FlowJo 10 (Becton Dickinson, Mountain View, CA, USA).

EV transfer

Sorted $CD34^-$ HSC were stained with 2 μM PKH26 (Sigma-Aldrich, Cat# MINI26-1KT) for 2 min at room temperature, then washed three times with StemSpan SFEM. PKH26-stained cells were plated in a 96 well plate and cultured in StemSpan SFEM medium as described above. After 48 h, the media was collected and EVs isolated as described above. Isolated EVs were administered to freshly isolated $CD34^-$ HSC every 24 h for 48 h.

Super-resolution radial fluctuation imaging of EVs markers

Isolated EVs were seeded on a coverslip cleaned by acid wash and coated with poly-lysine for 60 min at 37C to allow adhesion. EVs were then fixed with filtered 2% PFA for 10 min then blocked with filtered 5% BSA for 60 min at room temperature. Anti-CD63 (Abcam, Cat# ab134045) antibody was diluted 1:100 in filtered 5% BSA and incubated overnight at 4°C. After primary antibody hybridization, samples were washed three time with filtered PBS, then incubated with secondary antibodies goat anti-rabbit conjugated with Alexa 488 (Thermo Fisher Scientific, Cat# A32731). A coverslip containing fluorescent beads (TetraSpeck, Thermo Fisher Scientific, Cat# T7279) or PBS only were used as a positive and negative references for EVs detection.

Imaging was performed using a Nikon ECLIPSE Ti inverted widefield microscope equipped with 60× objective (CFI Plan Apo Lambda 60x/1.4 oil) and an additional 1.5× magnification was used to collect fluorescence onto an EMCCD camera (iXonEM+ 885, Andor), yielding a pixel size of 88 nm. Excitation was provided by a Lambda LS Stand-Alone 175W Xenon Arc Lamp filtered through a FITC excitation filter (FF01-494/20, Semrock) and a neutral density filter (ND8, Nikon). For each field of view was acquired a 200 frames stack with exposure of 164 ms.

Images were processed through the eSRRF plugin on ImageJ (https://github.com/HenriquesLab/NanoJ-eSRRF).[93] Before processing the whole dataset, parameter sweep function was used then radius value was set at 4, sensitivity was set to 4. The processed eSRRF images were then analyzed using Olympus scanR. Briefly, spots were identified in all images using the edge detection function. For each spot, area, circularity and CD63 total intensity were collected. The gating strategy was also applied for analysis using Olympus scanR. Representative gating for Figure S7I was obtained using FlowJo 10 (Becton Dickinson).

nFCM analysis

For each staining reaction, 2×10^8–2×10^9 of purified EVs were incubated with CD63-APC (a15712, life technologies) primary antibodies for 1 h at 37°C under shaking, protected from light. Unbound antibodies were removed by repeated washing (6–8 times) with 500 μL PBS prior to analysis. Samples were next acquired using the NanoAnalyzer (nanoFCM Inc.).

Before each experiment, the NanoAnalyzer was aligned using polystyrene QC beads (nanoFCM Inc.). Size and concentration standard nanospheres (nanoFCM Inc.) were read directly after to calibrate the instrument for EV analysis. Once nFCM was aligned and calibrated, EV samples were diluted in filtered PBS (blank) to the optimal range for measurement (10^8 particles/mL). Samples and blanks (200–800 events) were measured for 1 min, applying a laser power of 15 mW as excitation source, constant pressure of

1 kPa, and at an event rate between 2500 and 12,000 events/min (as recommended by manufacturers). SSC was set as the trigger channel, each particle that generated a signal above the SSC threshold was acquired as an event. For each event that also generated a signal above thresholds set in the fluorescent channels, the fluorescence intensity was registered. Empty staining reactions (without EVs) were performed as a control for all fluorescent reagents and measured under the same conditions as complete reactions (with EVs). Data analysis was performed using FlowJo 10 (Becton Dickinson).

Immunostaining

Sorted cells were resuspended in 30 μL of StemSpan SFEM supplemented with 50 ng/mL SCF and 50 ng/mL thrombopoietin (PeproTech) and then seeded on Lab-Tek II Chamber Slide (Thermo Fisher Scientific, Cat# 154526) coated with Fibronectin (Sigma-Aldrich, Cat# F1141). Samples were then immunostained as described above. Anti-Farnesyl, rabbit polyclonal antibody (Sigma-Aldrich, Cat# 341286, dilution 1:100) or Anti-Ki-67 (D3B5) rabbit monoclonal antibody were used for detection of protein farnesylation or ki67 respectively. After primary antibody hybridization, samples were washed three time with filtered PBS, then incubated with secondary antibodies goat anti-rabbit conjugated with Alexa Fluor 488 (Thermo Fisher Scientific, Cat# A32731) or anti-rabbit conjugated with Alexa Fluor 594 (Thermo Fisher Scientific, Cat# A11037). Images were acquired using a ZEISS AXIO examiner D1 microscope (Zeiss) equipped with a 40× oil Plan-APOCHROMAT objective and a Coolsnap HQ2 camera (Photometrics). Next were processed and analyzed by CellProfiler (https://cellprofiler.org/)[94] using a customized pipeline. Briefly, images were subtracted from the background, segmented via the Otsu algorithm, then average intensity was then collected for each cell per field of view and used as readout of protein farnesylation.

QUANTIFICATION AND STATISTICAL ANALYSIS

For each dataset, the normality assumption was verified with the D'Agostino-Pearson Omnibus Test. Sample sizes and reproducibility for each figure are denoted in the figure legends. For mouse experiments, no statistical method was used to predetermine sample size. Experiments were not randomized, and the investigators were not blinded to allocation during experiments and outcome assessment. All data were collected and analyzed by Prism 7 (GraphPad). Samples that satisfied the normality assumption were evaluated through T-test, one-way or two-way ANOVA, appropriate multiple comparison correction is indicated in the figure legend for each data. When was not satisfied they were tested by Wilcoxon signed rank test or Kruskal-Wallis test. The used test is indicated in the figure legend for each data. All graphs show mean values. Error bars indicate +/− SEM, unless otherwise indicated.

Cell Stem Cell, Volume *31*

Supplemental Information

A mitochondrial NADPH-cholesterol axis regulates extracellular vesicle biogenesis to support hematopoietic stem cell fate

Massimo Bonora, Claudia Morganti, Nick van Gastel, Kyoko Ito, Enrica Calura, Ilaria Zanolla, Letizia Ferroni, Yang Zhang, Yookyung Jung, Gabriele Sales, Paolo Martini, Takahisa Nakamura, Francesco Massimo Lasorsa, Toren Finkel, Charles P. Lin, Barbara Zavan, Paolo Pinton, Irene Georgakoudi, Chiara Romualdi, David T. Scadden, and Keisuke Ito

Figure S1 Bonora et al

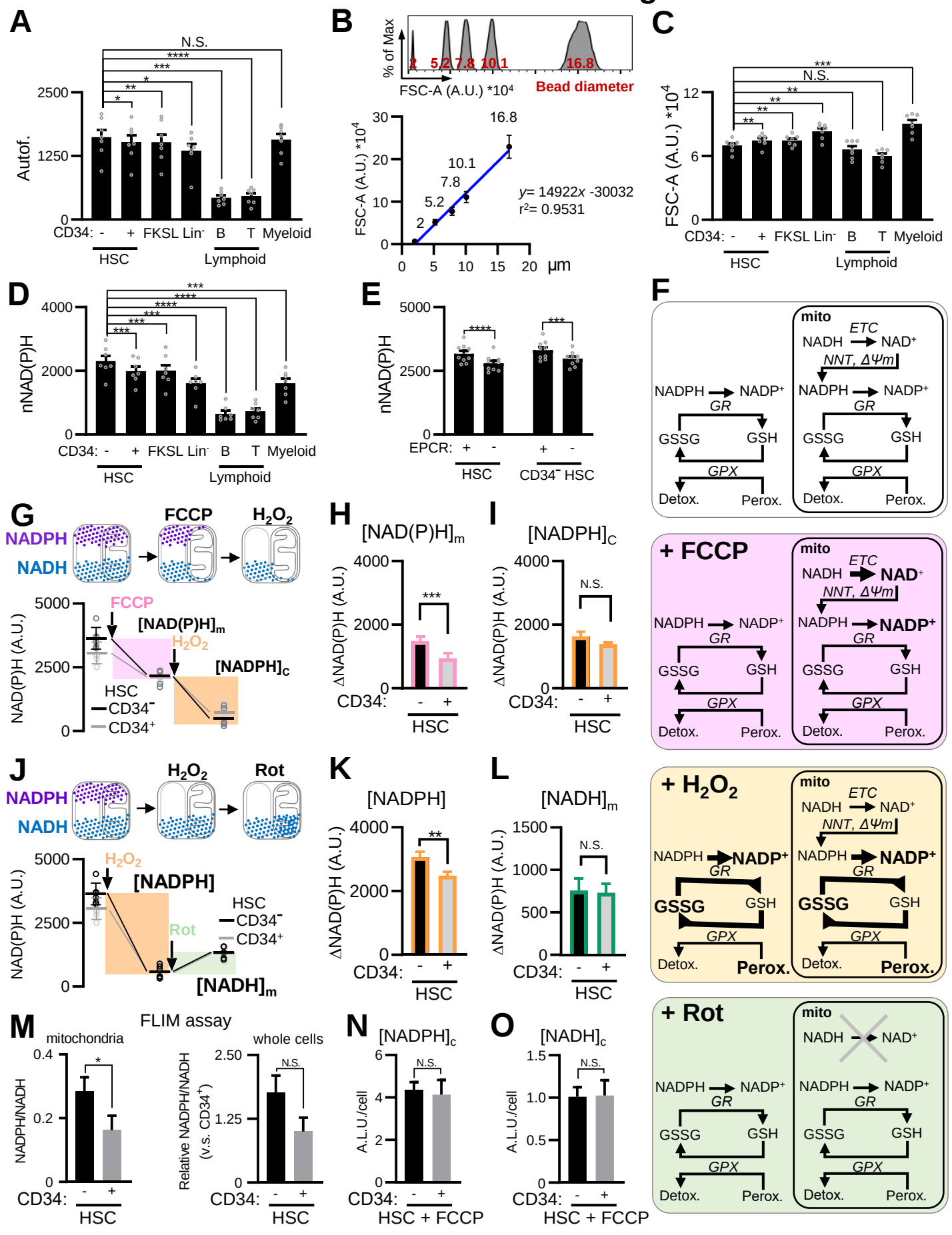

Figure S2 Bonora et al

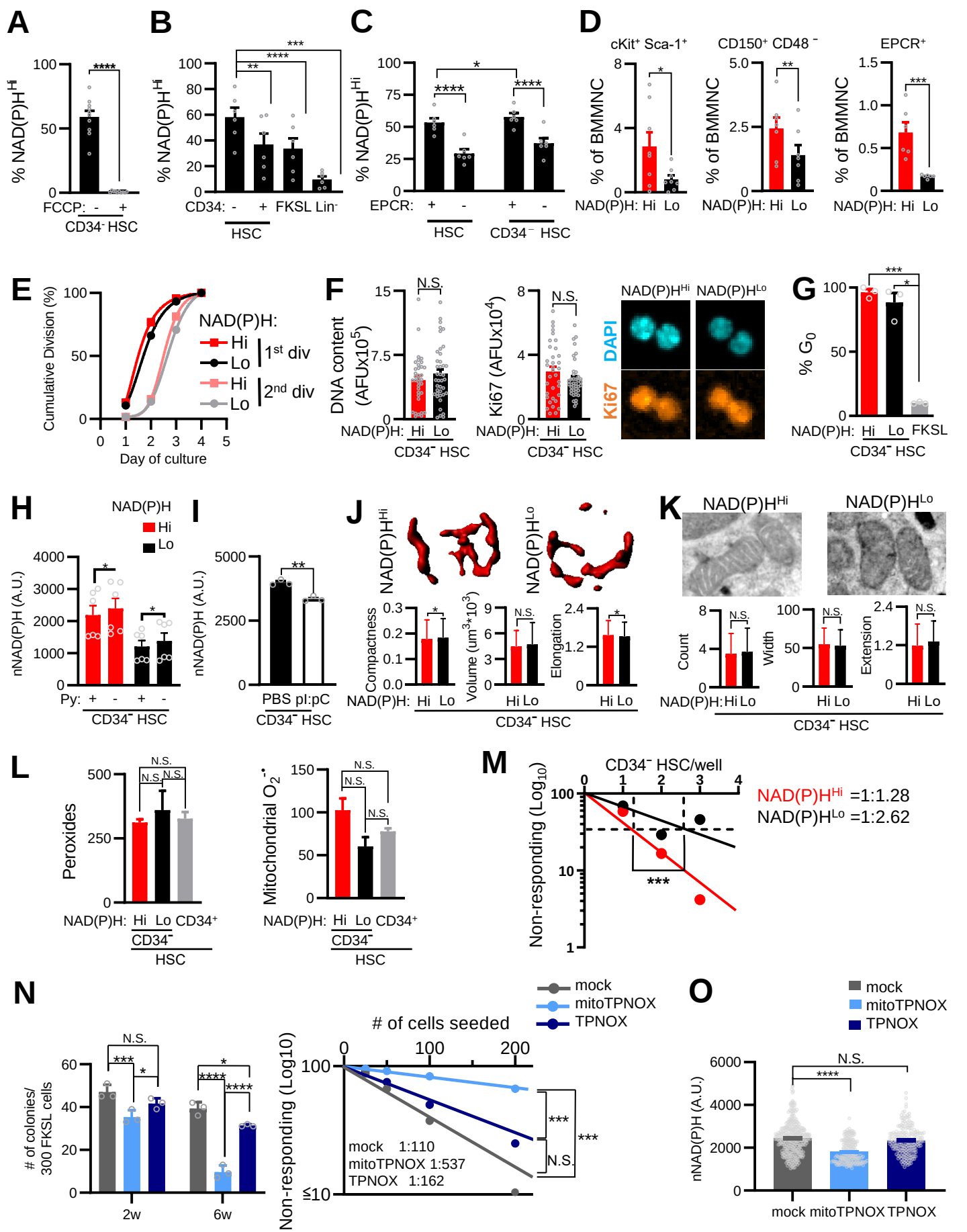

Figure S3 Bonora et al

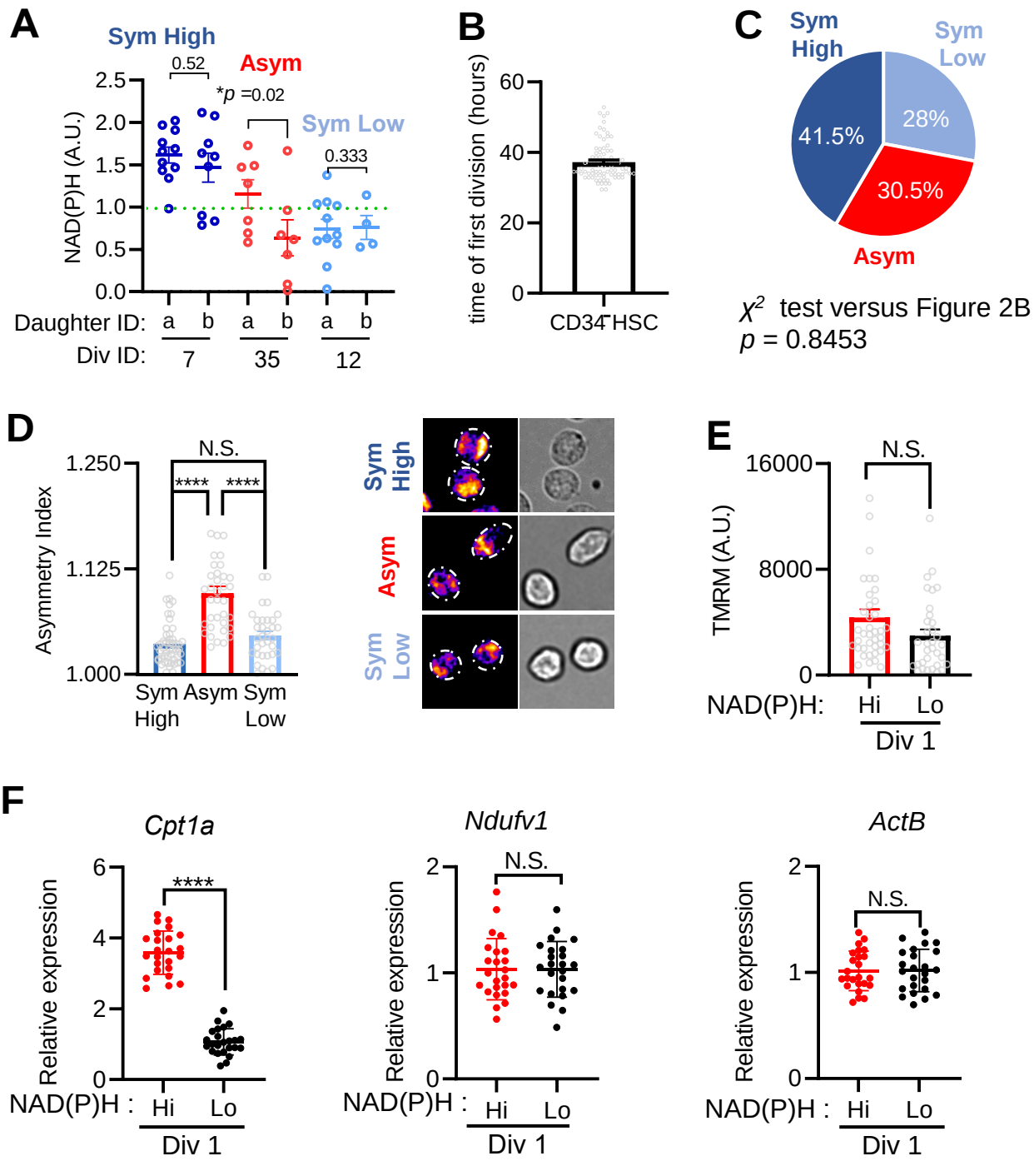

Figure S4 Bonora et al

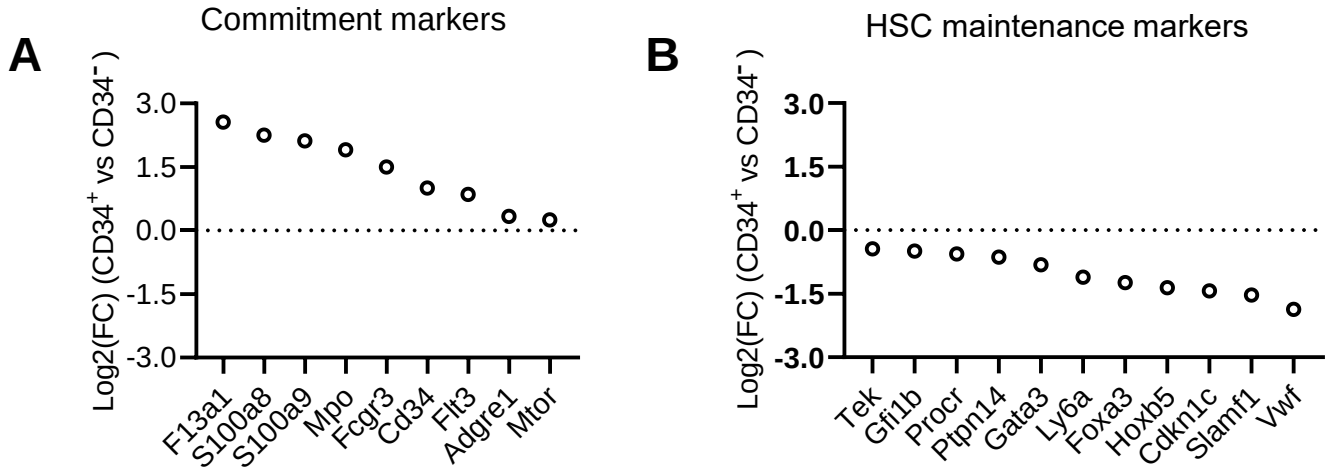

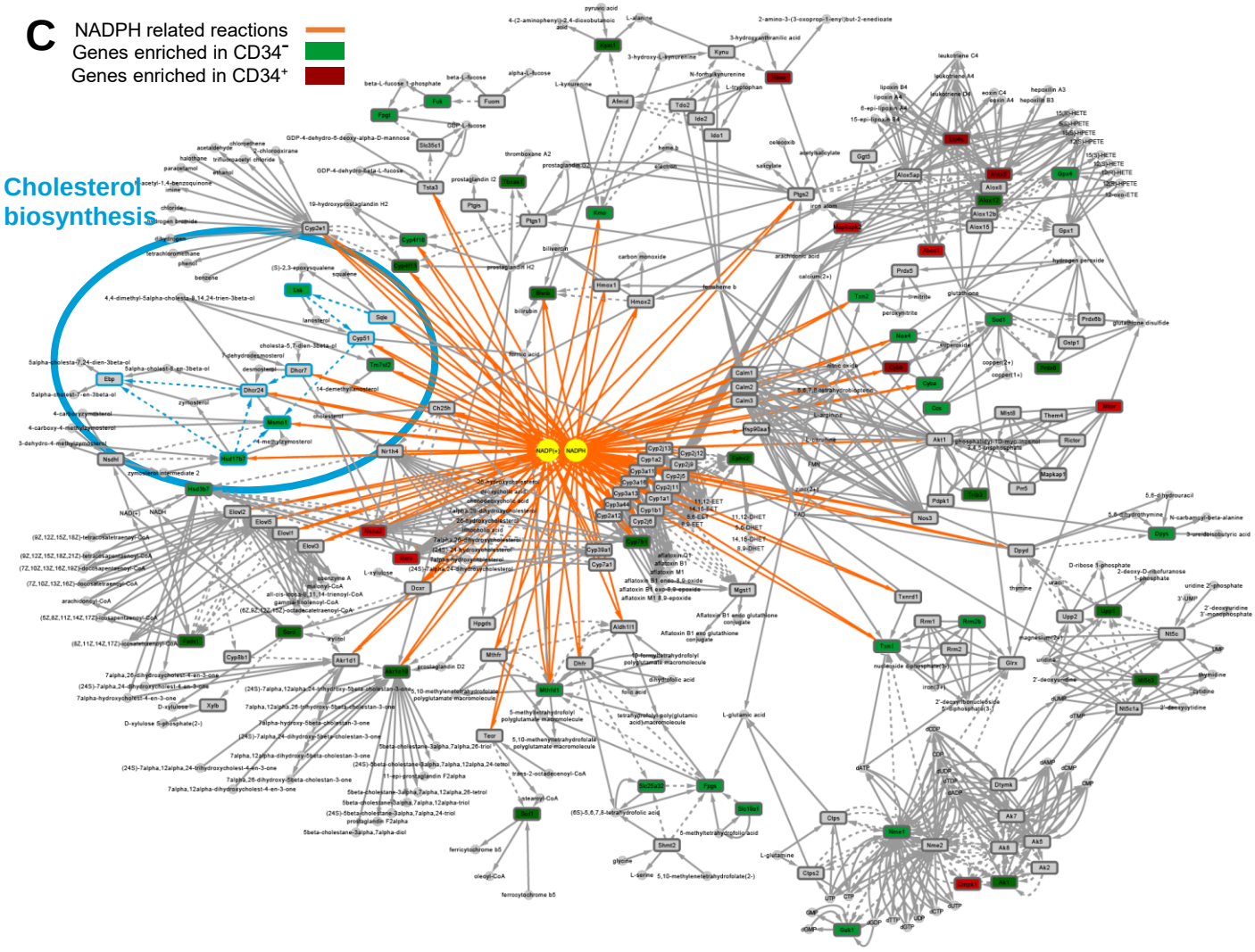

Figure S5 Bonora et al

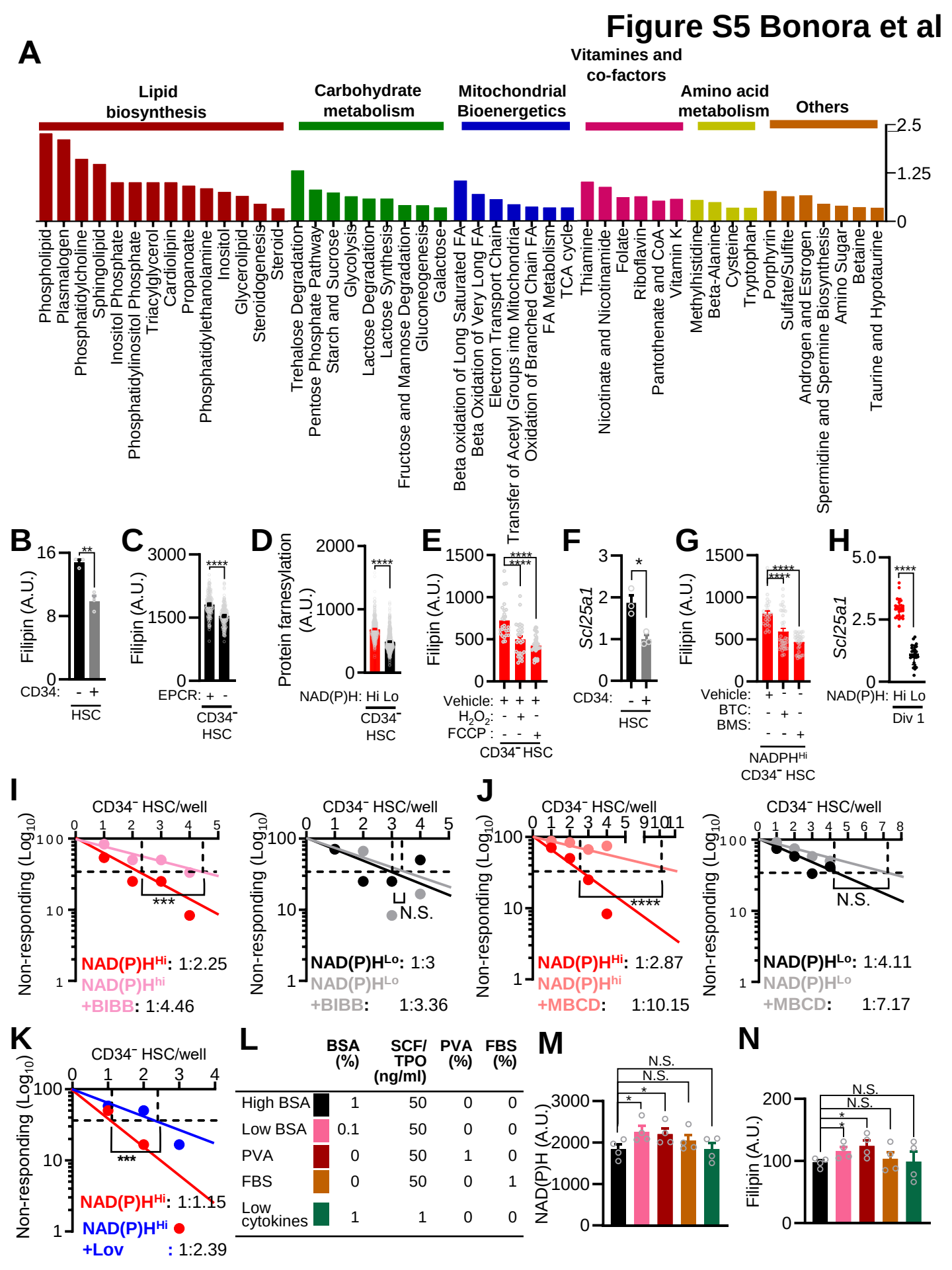

Figure S6 Bonora et al

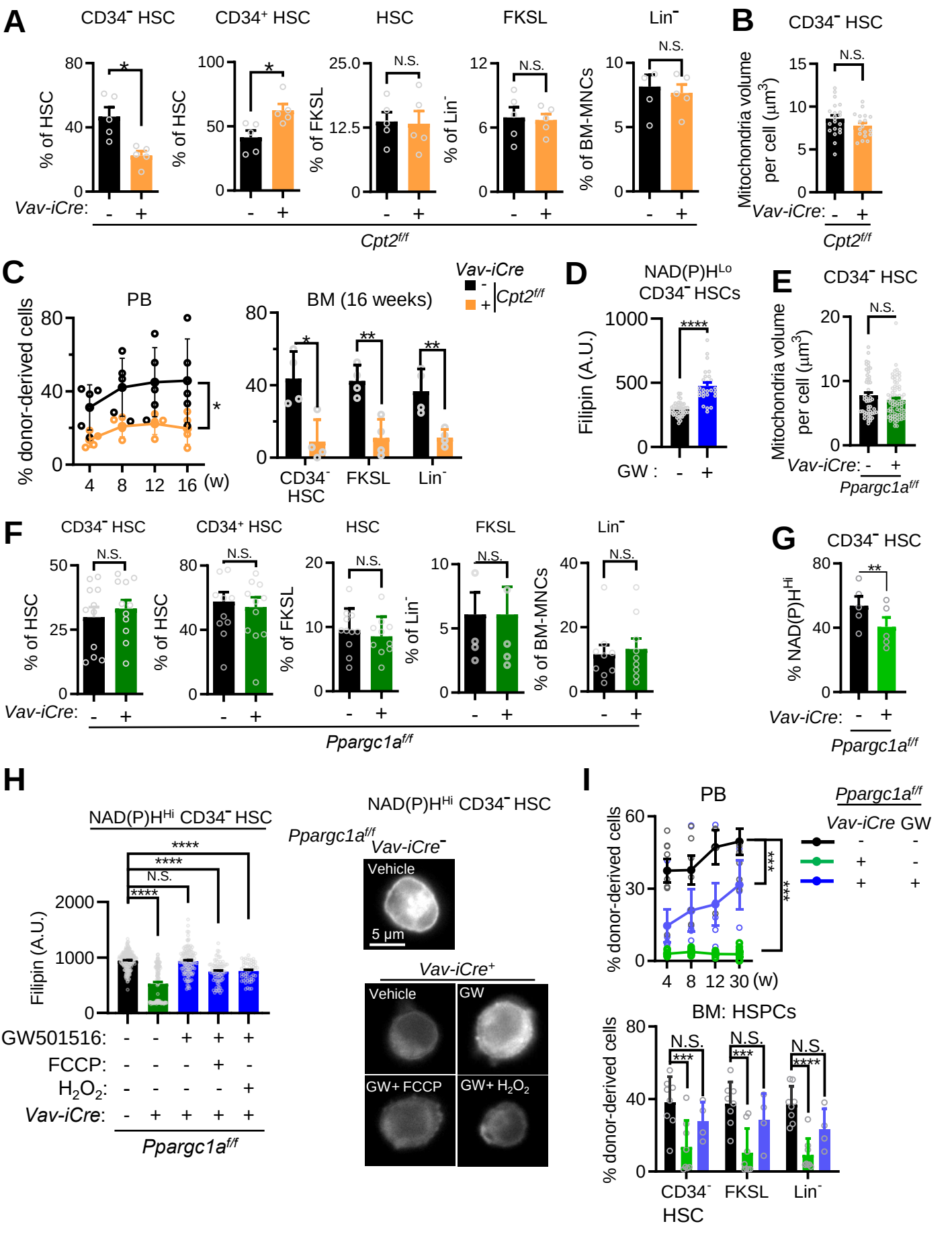

Figure S7 Bonora et al

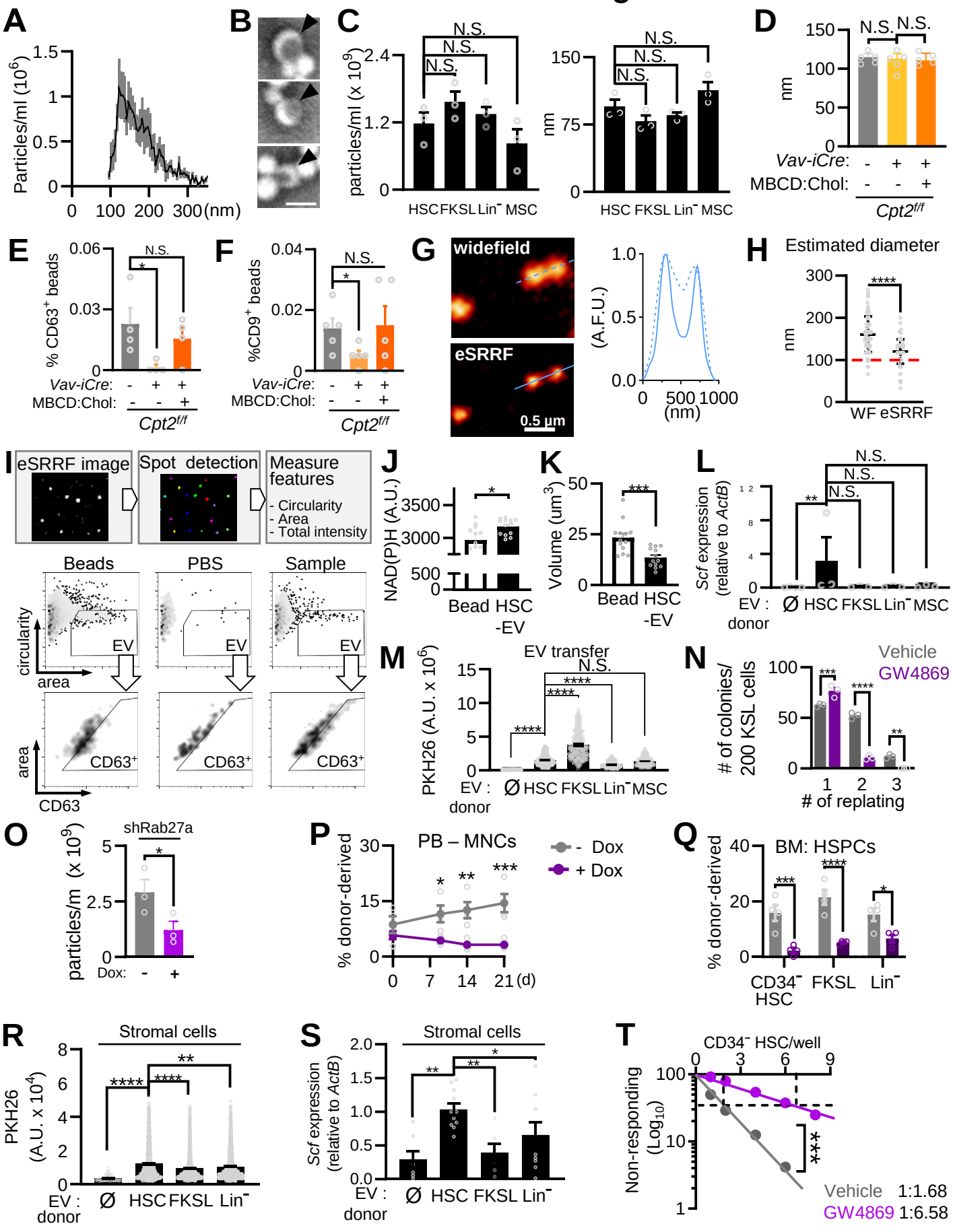

Supplemental Items

Supplemental Figure Titles and Legends

Figure S1. CD34^{-} HSC have high mitochondrial NADPH levels, related to Figure 1

(A) Quantitation of NAD(P)H autofluorescence in the different hematopoietic populations investigated (n = 7 mice, 2 months old). Autofluorescence appeared brighter in CD150+CD48−CD135−Lin−Sca-1+c-Kit+ cells (hereafter, HSCs), and displayed a dimming trend with hematopoietic differentiation (Figures 1A and S1A). Fully differentiated myeloid cells apparently deviate from this trend, and significantly differ from the lymphoid compartment. As these populations dramatically vary in their size, we supposed that cell size might affect the accurate description of the NAD(P)H autofluorescence across differentiation.

(B) Representative flow cytometric histogram (top) and linear regression analysis (bottom) of FSC-A in commercial calibration beads differing for their diameter size, acquired in the same flow cytometer used to investigated NAD(P)H autofluorescence (also see STAR Methods). The use of size calibration beads confirms that the FSC-A can be used as a readout of cell size.

(C) Quantitation of FSC-A, used as a readout of cell size, in the different hematopoietic populations investigated (n = 7 mice, 2 months old). As expected, myeloid cells are larger than other populations investigated.

(D) Quantitation of normalized NAD(P)H (nNAD(P)H) autofluorescence in the different hematopoietic populations investigated (n = 7 mice, 2 months old). Normalization of the autofluorescence is obtained by dividing NAD(P)H intensity on FSC-A to obtain a readout of cellular NAD(P)H density. This readout confirms the dimming trend of NAD(P)H levels with differentiation which reaches the lower levels in fully differentiated cells, especially in the lymphoid compartment.

(E) Flow cytometric analysis of normalized NAD(P)H autofluorescence in $EPCR^+$ and $EPCR^-$ gated in HSC or $CD34^-$ HSC populations (n = 6 mice, 2 month old).

(F) Schematic representation of the rationale for analysis of NAD(P)H composition. Administration of the mitochondrial uncoupler FCCP collapse ΔΨm and the maximization of ETC rates causing the complete oxidation of mitochondrial NADH to NAD^+. This also results in the block of conversion of NAD^+ to NADPH (e.g., by means of NNT activity), ultimately leading to oxidation of mitochondrial NADPH to $NADP^+$. The exposure to H_2O_2 dramatically increases the activity of glutathione peroxidase (GPX) which converts GSH to GSSG in the effort of detoxify peroxides. GSSG is reversed to GSH by the glutathione reductase (GR), the electrons required are obtained from NADPH which is completely oxidized to $NADP^+$. As GPX and GR exist in both mitochondria and cytosol, all NADPH in both compartments is consumed. The administration of rotenone (Rot) blocks NADH consumption at level of respiratory complex I of ETC, inducing the selective accumulation of mitochondrial NADH.

(G) Analysis of NAD(P)H composition by sequential administration of mitochondrial uncoupler FCCP and H_2O_2. FCCP 1 μM causes consumption of mitochondrial NAD(P)H, the difference in NAD(P)H intensity between basal and after FCCP stimulation is a readout of [NAD(P)H]m (pink box). Subsequent administration of H_2O_2 induces the oxidation of residual, cytosolic NADPH but not NADH. Cytosolic NADPH is then calculated by the difference between basal and H_2O_2-exposed cells (orange box).

(H) Mitochondrial NAD(P)H determined by FCCP 1 μM in $CD34^-$ and $CD34^+$ HSCs (n = 6 mice, 2 months old). **(I)** Cytosolic NADPH determined by 100 μM H_2O_2 in $CD34^-$ and $CD34^+$ HSCs (n = 6 mice, 2 months old).

(J) Analysis of NAD(P)H composition by sequential administration of H_2O_2 and the respiratory complex I inhibitor Rot. Exposure to H_2O_2 causes the consumption of cytosolic and mitochondrial NADPH. The difference in NAD(P)H intensity at basal or after H_2O_2 stimulation is a readout of [NAD(P)H] (orange box). Subsequent administration of Rot causes the accumulation of NADH, but not NADPH, due to inhibition of respiratory complex I. The differences in autofluorescence in the presence of H_2O_2 or Rot + H_2O_2 is used as a readout of NADH fueling respiratory chain (green box).

(K) Total NADPH determined by 100 μM H_2O_2-induced in $CD34^-$ and $CD34^+$ HSCs (n = 6 mice, 2 months old). **(L)** Flux of mitochondrial NADH determined by 100 nM Rot-induced accumulation in $CD34^-$ and $CD34^+$ HSCs (n = 6 mice, 2 months old).

(M) Analysis of τ bound (reporter of NADPH/NADH ratio) in mitochondria in the indicated HSC fractions, measured by fluorescence lifetime imaging (FLIM) (n = 10 for $CD34^-$ HSC, 7 for $CD34^+$ HSC, respectively). Sorted HSCs were stained with TMRM to visualize mitochondria then imaged with two-photon laser. A unique excitation at 720 nm was selected to image contemporary both NAD(P)H and TMRM, this allows to minimize chromatic aberration and acquisition time (which improve cell viability). The TMRM signal was used to quantify τ bound in mitochondria (left). Relative τ bound in whole cells in the indicated HSC fractions are also shown in the inset (right).

(N and **O)** Enzymatic determination of levels of cytoplasmic NADPH **(N)** and NADH **(O)** in $CD34^-$ and $CD34^+$ HSCs (n = 5 mice, 2 months old).

EPCR, Endothelial protein C receptor; HSC, $Lin^{-}Sca\text{-}1^{+}c\text{-}Kit^{+}CD135^{-}CD150^{+}CD48^{-}$; Detox, detoxified peroxides; FKSL, $CD135^{-}c\text{-}Kit^{+}Sca\text{-}1^{+}Lin^{-}$; GSH, reduced glutathione; GSSG, Oxidized glutathione; NNT, NAD(P) transhydrogenase; Perox, peroxides; Rot, rotenone.

Bar graphs represent means ± SEM, circles represent each replicate. **(A), (C),** and **(D)** 1-way ANOVA with Dunnet's multiple comparison test. **(E)**, Two-way ANOVA with Sidak's multiple comparison test. **(H)**, **(I)**, **(K)**, **(L)**, **(M)**, **(N)**, and **(O)**: paired Student's T test. ***, $0.0001 \leq p < 0.001$; **, $0.001 \leq p < 0.01$; N.S., not significant, $p \geq 0.05$.

Figure S2. Mitochondrial NADPH levels mark stem cell capacity, related to Figure 1

(A) Percentage of $NAD(P)H^{Hi}$ cells in $CD34^{-}$ HSCs at the steady state (black) and in response to FCCP (grey) (n = 10 mice, 2 month old) (also see **Figure 1H**). $NAD(P)H^{Lo}$ gate was defined as the region containing >95% of cells in presence of 1 μM FCCP, with $NAD(P)H^{Hi}$ as the upper region of the scatterplot and containing <2% of cells exposed to FCCP (top).

(B) Percentage of $NAD(P)H^{Hi}$ cells in the indicated bone marrow fractions (n = 6 mice, 2 month old).

(C) Percentage of $NAD(P)H^{Hi}$ cells in $EPCR^{+}$ and $EPCR^{-}$ gated in HSC or $CD34^{-}$ HSC populations (n = 6 mice, 2 month old).

(D) The frequency of stem cell markers cKit and Sca-1, CD150, and CD48 in the whole BMMNCs gated for $NAD(P)H^{Hi}$ of $NAD(P)H^{Lo}$ (n = 6 mice, 2 month old)**.**

(E) Cell division kinetics. Single NAD(P)H^{Hi} or NAD(P)H^{Lo} CD34^{-} HSCs were isolated and cultured. Cells were counted every 24 h to determine division kinetics (NAD(P)H^{Hi}, n = 75 cells; NAD(P)H^{Lo}, n = 69 cells; 3 independent experiments).

(F) Quantitation (left) and representative images (right) of sorted NAD(P)H^{Hi} or NAD(P)H^{Lo} CD34^{-} HSCs stained with the DNA marker DAPI or the proliferation marker Ki67 (NAD(P)H^{Hi}, n = 35 cells; NAD(P)H^{Lo}, n = 40 cells; 3 independent experiments).

(G) Percentage of G_0 cells in NAD(P)H^{Hi} and NAD(P)H^{Lo} CD34^{-} HSCs (n = 3 mice, 2 month old) determined by Pyronin Y staining in flow cytometry.

(H) Quantitation of normalized NAD(P)H autofluorescence in NAD(P)H^{Hi} and NAD(P)H^{Lo} CD34^{-} HSCs gated in Py^{+} or Py^{-} (n = 6 mice, 2 month old).

(I) Quantitation of normalized NAD(P)H autofluorescence in CD34^{-} HSCs isolated from mice injected with PBS or pI:pC, one week before isolation, to stimulate HSC exit from proliferation *in vivo* (n = 3 mice, 2 month old).

(J) Mitochondrial morphometry of NAD(P)H^{Hi} and NAD(P)H^{Lo} CD34^{-} HSCs (NADPH^{Hi}, n = 1898 mitochondria; NADPH^{Lo}, n = 1340 mitochondria) (right). Representative surface rendering of mitochondria (TMRM-stained) (left).

(K) Representative TEM images of mitochondria of NAD(P)H^{Hi} and NAD(P)H^{Lo} CD34^{-} HSC (top). Descriptors of mitochondrial cristae ultrastructure (NADPH^{Hi}, n = 89; NADPH^{Lo}, n = 65) (bottom).

(L) Analysis of oxidative stress by the peroxides reporter 2',7'-dichlorofluorescein (left) and mitochondrial superoxide reporter MitoSOX (right) in NAD(P)H^{Hi} and NAD(P)H^{Lo} CD34^{-} and CD34^{+} HSC (n = 3 mice, 2 month old).

(M) Long-term culture-initiating cell (LTC-IC) capacity of NAD(P)H^{Hi} and NAD(P)H^{Lo} CD34^{-} HSCs, determined in a limiting-dilution assay (n ≥ 12 replicates, 4 independent experiments).

(N) Sorted FKSL cells were infected with mitoTPNOX (light blue), TPNOX (blue) or empty vector (mock, grey) for 24 hours, then selected with puromycin 1 µg/ml for 48 hours before. Cells were then used for colony-replating capacity at the indicated weeks after *in vitro* culture (n = 3, left) and the LTC-IC capacity (≥ 12 replicates, 3 independent experiments, right) in media supplemented with Dox 300 ng/mL.

(O) Quantitation of mitochondrial NAD(P)H autofluorescence in FKSL cells expressing TPNOX, mitoTPNOX or mock after 2 weeks of culture and exposure to Dox, obtained by fluorescence microscopy (mock, n = 318; TPNOX, n = 202; mitoTPNOX, n = 193 from 3 independent experiments).

Div, division; EPCR, Endothelial protein C receptor; HSC, Lin^{-}Sca-1^{+}c-Kit^{+}CD135^{-}CD150^{+}CD48^{-}; AFU, arbitrary fluorescent unit; Dox, Doxycycline; Py, Pyronin Y, TEM, transmission electron microscopy; w, week. Bar graphs represent means ± SEM, circles represent each replicate. **(A), (D), (M),** and **(N, right)**: Paired Student's t test. **(B)**, **(G)**, **(L)**, and **(O)**: 1-way ANOVA with Dunnet's multiple comparison test. **(F)**, **(I)**, **(J)**, and **(K)**: unpaired Student's t test. **(C)**, **(H)**, and **(N, left)**: Two-way ANOVA with Sidak's multiple comparison test. ****, $p < 0.0001$; ***, $0.0001 \leq p < 0.001$; **, $0.001 \leq p < 0.01$; *, $0.01 \leq p < 0.05$; N.S., not significant, $p \geq 0.05$.

Figure S3. Mitochondrial NADPH level controls HSC fate determination, related to Figure 2

(A) Representative measurements of mitochondrial NAD(P)H intensity in the paired daughter cells obtained as described in **Figure 2A** (also see Methods section). Dotted line represents the

median value of all the dataset and is used as threshold value to distinguish Sym High from Sym Low divisions.

(B) Analysis of time of first division obtained by single-cell *in vitro* tracking in sorted $CD34^-$ HSC imaged as described in **Figure 2D** (n= 84 from 3 independent experiments).

(C) Proportion of the output of the first division cultured $NADPH^{HI}$ $CD34^-$ HSCs investigated by live imaging as described in **Figure 2A-2D** (n = 118 division). The output observed in live imaging were compared with the proportion observed from 3D imaging (**Figures 2A-2B**) using χ^2 test.

(D) Analysis of the NAD(P)H asymmetry index in HSC daughter after first division during interphase. Classification of asymmetry of the division for cells in interphase are determined as in **Figure 2C** and **2D** Representative NAD(P)H and brightfield images for each type of division are also shown (n = 3 experiments).

(E) Analysis of TMRM intensity (indirect reporter of mitochondrial respiration) in the paired daughter cells obtained as described in **Figure 2B** ($NADPH^{Hi}$, n = 39 cells; $NADPH^{Lo}$, n = 33 cells).

(F) Levels of *Cpt1a* (FAO marker), and *Ndufv1* (respiratory complex I marker) in single $NAD(P)H^{Hi}$ and $NAD(P)H^{Lo}$ $CD34^-$ HSCs cells who underwent only one division. Gene expression was quantified by qRT-PCR related to *ActB* (n = 24 cells).

Bar graphs represent means ± SEM, circles represent each replicate. **(A)**: Mann-Whitney U test, **(C)**: χ^2 test, **(D)**: 1-way ANOVA with Dunnet's multiple comparison test, **(E)**, and **(F)**: Unpaired Student's t test. ****, $p < 0.0001$; **, $0.001 \leq p < 0.01$; *, $0.01 \leq p < 0.05$; N.S., not significant, $p \geq 0.05$.

Figure S4. Identification of NAD(P)H dependent pathways in HSC, related to Figure 3

(A) Gene expression fold change of commitment genes identified as described in **Figure 3A** which display their enrichment in the $CD34^+$ HSCs.

(B) Gene expression fold change of HSC maintenance genes identified as described in **Figure 3A** which display their enrichment in the $CD34^-$ HSCs.

(C) Schematic representation of the main NADPH-dependent pathway derived from the analysis described in **Figure 3A**. Green nodes are differentially expressed genes upregulated in $CD34^-$, while red nodes are upregulated in $CD34^+$. NADPH dependent reactions are highlighted by orange arrows. The cholesterol pathway is enlightened in light blue.

Figure S5. NADPH sustains cholesterol biosynthesis in HSCs, related to Figure 4

(A) Summary plot for the metabolite set enrichment analysis between $NAD(P)H^{Hi}$ and $NAD(P)H^{Lo}$ $CD34^-$ HSC, mapped to the small molecule pathway database (SMPDB). Pathways are manually clustered into groups according to the main biochemical species involved, then within each group, ranked by the p-value.

(B) Quantitation of filipin staining in $CD34^-$ and $CD34^+$ HSCs (n = 3 mice, 2 month old).

(C) Quantitation of filipin staining in $EPCR^+$ and $EPCR^-$ gated in $CD34^-$ HSC populations ($NAD(P)H^{Hi}$, n = 1541 cells: $NAD(P)H^{Lo}$, n = 1811 cells).

(D) Quantitation of sorted $NAD(P)H^{Hi}$ and $NAD(P)H^{Lo}$ $CD34^-$ HSCs immunostained with anti-farnesyl antibody [$NAD(P)H^{Hi}$, n = 507; $NAD(P)H^{Lo}$, n = 902).

(E) Quantitation of filipin staining in sorted NAD(P)H^{Hi} and NAD(P)H^{Lo} CD34^{-} HSCs then exposed to 1 μM FCCP and 100 μM H_2O_2 to stimulate oxidation of NAD(P)H [NAD(P)H^{Hi}, n = 141 cells; NAD(P)H^{Hi} + H_2O_2, n = 137 cells; NAD(P)H^{Hi} + FCCP, n = 102 cells; NAD(P)H^{Lo}, n = 107 cells].

(F - **H)** The transport of Acetyl-CoA to the cytosol is permitted by the mitochondrial citrate-malate shuttle.[40,41] The mitochondrial citrate transport protein (CTP) coded by *Slc25a1* transports mitochondrial citrate or isocitrate to the cytosol in exchange for cytosolic malate, which is then converted to acetyl-CoA, by ATP citrate lyase (ACLY). **(F)** Expression levels of Slc25a1 in CD34^{-} and CD34^{+} HSCs quantified by qRT-PCR (n = 3) relative to *ActB*. **(G)** Quantitation of filipin staining in the sorted NAD(P)H^{Hi} CD34^{-} HSCs then exposed to the inhibitor of CTP (5 mM BTC) or ACYL (1 mM BMS) to inhibit citrate/isocitrate shuttling from mitochondria or its conversion to Ac-CoA respectively [Vehicle, n = 26 cells; BTC, n = 37 cells; BMS, n = 33 cells]. **(H)** Expression levels of *Slc25a1*in single NAD(P)H^{Hi} and NAD(P)H^{Lo} CD34^{-} HSCs who underwent only one division. Gene expression was quantified by qRT-PCR relative to *ActB* (n = 24 cells).

(I) LTC-IC capacity of NAD(P)H^{Hi} and NAD(P)H^{Lo} CD34^{-} HSCs exposed to BIBB 515 (n ≥ 12 replicates, 3 independent experiments).

(J) Inhibition of cholesterol biosynthesis can dramatically impact cell proliferation and potentially bias colony detection in the LTC-IC assay. To confirm the effect of BIBB-515, we also utilized an alternative approach for cholesterol deprivation via methyl-β-cyclodextrin (MBCD), a torus-shaped oligosaccharide able to extract cholesterol from the plasma membrane.[43] LTC-IC capacity of NAD(P)H^{Hi} and NAD(P)H^{Lo} CD34^{-} HSCs exposed to MBCD (n ≥ 12 replicates, 3 independent experiments).

(K) LTC-IC capacity of NAD(P)H^{Hi} and NAD(P)H^{Lo} CD34^{-} HSCs exposed to lovastatin (Lov) (n ≥ 12 replicates, 3 independent experiments).

(L) The composition of the culture media has a significant effect on the function of HSC *in vitro.*[45,46,105,106] For example, supplementation of BSA or serum, and high SCF and TPO concentration were proposed to activate HSC metabolism *in vitro.*[45,46,105,106] Different media composition were tested on their impact on NAD(P)H and/or cholesterol. Reference media was supplemented with 1% BSA and 50 ng/ml SCF/TPO (see STAR method section), and we additionally tested low BSA concentration (0.1%), 1% FBS, BSA substitution with polyvinyl alcohol (1% PVA), and cytokine concentration lowered to 1ng/ml SCF/TPO. The table present the summary of media and their main differing components used to test autofluorescence and cholesterol levels in cultured CD34^{-} KSL.

(M) Quantitation of NAD(P)H autofluorescence by fluorescence microscopy in CD34^{-} KSL cultured in the different media as described in **Figure S5L** for one week (n = 4 independent experiments).

(N) Quantitation of filipin staining by fluorescence microscopy in CD34^{-} KSL cultured in the different media as described in **Figure S5L** for one week (n = 4 independent experiments).

BIBB, BIBB 515; BTC, benzenetricarboxylate; Chol, cholesterol; Lov, lovastatin; MBCD, methyl-β-cyclodextrin. Bar graphs represent means ± SEM, circles represent each replicate. **(B), (C), (D), (F),** and **(H)**: unpaired Student's t test. **(E), (G), (M),** and **(N)**: 1-way ANOVA with Dunnet's multiple comparison test. **(I)**, **(J)**, and **(K)**: Paired Student's t test. ****, $p < 0.0001$; **, $0.001 \leq p < 0.01$; N.S., not significant, $p \geq 0.05$.

Figure S6. FAO sustains NADPH and cholesterol axis, related to Figure 5

(A) Bone marrow composition (% of the parent population) of 4-month old *Cpt2*$^{f/f}$ *Vav-iCre*$^{-}$ and *Vav-iCre*$^{+}$ mice (n = 5 mice, 2 month old).

(B) Quantitation of mitochondrial network volume in CD34^{-} HSCs from *Cpt2*$^{f/f}$ *Vav-iCre*$^{-}$ and *Vav-iCre*$^{+}$ mice (n = 20 cells).

(C) Percentages of donor-derived cells in peripheral blood and HSPCs of recipient mice at the indicated weeks after 1st BMT (n = 4 recipients) (also see **Figure 5G -5I**).

(D) Quantitation of filipin staining in NAD(P)H^{Lo} CD34^{-} HSCs exposed to the PPARD agonist 0.1 μM GW501516 (blue) or vehicle control (black) for 24 hours in culture (Vehicle, n = 26 cells: GW, n = 42 cells).

(E) Quantitation of mitochondrial network volume of CD34^{-} HSCs in 4-months old *Ppargc1a*$^{f/f}$ *Vav-iCre*$^{-}$ and *Vav-iCre*$^{+}$ mice (n = 50 cells).

(F) Bone marrow composition (% of the parent population) of 4-months old *Ppargc1a*$^{f/f}$ *Vav-iCre*$^{-}$ and *Vav-iCre*$^{+}$ mice (n = 11 mice, 2 month old).

(G) Proportion of NAD(P)H^{Hi} cells in CD34^{-} HSCs from *Ppargc1a*$^{f/f}$ *Vav-iCre*$^{-}$ and *Vav-iCre*$^{+}$ mice (n = 5 mice, 2 months old).

(H) Quantitation (left) and representative images of filipin (right) in NADPH^{Hi} CD34^{-} HSCs from *Ppargc1a*$^{f/f}$ *Vav-iCre*$^{-}$ and *Vav-iCre*$^{+}$ cultured for 24 hours in the presence or absence of GW501516, and/or after the induction of NADPH consumption by 1 μM FCCP or 100 μM H_2O_2 (*Vav-iCre*$^{-}$, n = 187 cells; *Vav-iCre*$^{+}$, n = 112 cells; *Vav-iCre*$^{+}$ + GW, n = 120 cells; *Vav-iCre*$^{+}$ + GW + FCCP, n = 54 cells; *Vav-iCre*$^{+}$ + GW + H_2O_2, n = 75 cells).

(I) Percentages of donor-derived cells in peripheral blood (the indicated weeks after BMT) and HSPCs of recipient mice at the indicated weeks after BMT (*Vav-iCre*$^{-}$, n = 8 recipients; *Vav-iCre*$^{+}$, n = 8 recipients; *Vav-iCre*$^{+}$ + GW, n = 5 recipients).

Bar graphs represent means ± SEM, circles represent each replicate. **(A)**, **(F)**, and **(G)**: paired Student's t test. **(B)**, **(D)**, and **(E)**: unpaired Student's T test. **(C)** and **(I)**: 2-way ANOVA with Sidak's multiple comparison test. **(H)**: 1-way ANOVA with Dunnet's multiple comparison test. ****, $p < 0.0001$; **, $0.001 \leq p < 0.01$; *, $0.01 \leq p < 0.05$; N.S., not significant, $p \geq 0.05$.

Figure S7. NADPH supports the biogenesis of extracellular vesicles (EVs) in HSCs, related to Figure 6

(A) Particle size distributions of EVs derived from CD34^{-} HSCs, measured by TRPS system. This technique estimate the size of nanoparticles by their capacity to interfere with the electric conductance of a membrane punctuated with nano-sized pores (pore size 100 nm) (n = 3 independent experiments). CD34^{-} HSCs were cultured in the medium for 48 hours to allow the release of EVs. EV-enriched media was collected and processed for EVs isolation via polyethylene glycol and centrifugation.[89] EVs were then analyzed as described in the Methods section.

(B) Transmission electron microscopic images from NAD(P)H^{Hi} CD34^{-} HSC-derived EVs confirming the specific characteristics for exosomes, including a round morphology with a central depression (black arrows). Scale bar, 100nm. EVs were isolated via polyethylene glycol and centrifugation.[89]

(C) Quantitation of particle concentration (left) and diameter (right) of EVs derived from the indicated BM populations and determined by NTA (n = 3 mice, 2 months old). EV-enriched media was collected and processed for EV isolation via polyethylene glycol and centrifugation.[89]

(D) TRPS system analysis of particle size of CD34$^-$ HSC-derived EVs isolated from *Cpt2*$^{f/f}$ *Vav-iCre*$^-$ and *Vav-iCre*$^+$ mice and cultured for 48 hours in presence or not of MBCD:Chol (n = 5 independent experiments; also see **Figure 6D**).

(E and **F)** HSC-derived EVs were enriched with immunomagnetic beads and then stained with antibodies against EV-surface markers CD63 or CD9. **(E)** Quantification of CD63 positive beads in EVs obtained from CD34$^-$ HSCs (from 2-month-old *Cpt2*$^{f/f}$ *Vav-iCre*$^-$ or *Cpt2*$^{f/f}$ *Vav-iCre*$^+$) exposed to MBCD:Chol to restore intracellular cholesterol levels or vehicle control (n = 4 independent replicates). The same volume of isolated EVs was used for each replicate. Gating strategy is also shown (bottom). **(F)** Quantification of CD9 positive beads in EVs obtained from CD34$^-$ HSCs (from 2-month-old *Cpt2*$^{f/f}$ *Vav-iCre*$^-$ or *Cpt2*$^{f/f}$ *Vav-iCre*$^+$) exposed to MBCD:Chol to restore intracellular cholesterol levels or vehicle control (n = 5 independent replicates). The same volume of isolated EVs was used for each replicate.

(G and **H)** Performance analysis of eSRRF microscopy conducted on commercial fluorescent beads (expected diameter 100 nm). For each sample, 200 frames stack were obtained with a pixel size of 88 nm to generate the eSRRF image (see STAR methods). Representative images of fluorescent beads obtained by widefield fluorescence microscopy or eSRRF **(G)** emphasize the increase in resolution of the eSRRF image as also displayed by the profile of intensity (right) measured along the blue line (widefield = dotted; eSRRF = continuous). Analysis of beads diameter on the same set of fluorescent beads imaged by widefield or eSRRF microscopy **(H).**

The red dashed line indicates the predicted diameter. Average and standard deviation of the mean are plotted (n = 113 beads).

(I) Experimental design (left) and representative gating strategy (right) used for the analysis of eSRRF images on HSC-derived EVs. All spots were detected using an edge-detection algorithm from the eSRRF image then measured for morphometric parameters and CD63 intensity. Spots were then gated for size, shape and intensity using the positive control (100 nm fluorescent beads) as reference. Next, the gates were adjusted to exclude spots found in the negative control (PBS) to minimize the possible contamination caused by image noise or aggregates of the fluorescent antibody. The remaining spots were considered bona fide EVs and their CD63 intensity compared across samples.

(J) Quantitation of NAD(P)H autofluorescence obtained by fluorescence microscopy in $CD34^-$ HSCs exposed to HSC-derived EV (HSC-EV) or negative control (Bead) (HSC-EV, n = 13 cells; Bead, n = 11 cells). EVs were isolated via polyethylene glycol and centrifugation.[89]

(K) Analysis of mitochondrial volume in $CD34^-$ HSCs exposed to HSC-derived EV (HSC-EV) or negative control (Bead) (HSC-EV, n = 13 cells; Bead, n = 13 cells). EVs were isolated via polyethylene glycol and centrifugation.[89]

(L) Expression levels of SCF in HSC exposed to EVs isolated from HSC, FKSL cells, Lin^- cells, MSC or empty (Ø) and obtained by qPCR relative to *ActB* (n = 3). Stem cell factor (SCF) is an essential hematopoietic cytokine that interacts with other cytokines to preserve the function of hematopoietic stem and progenitor cells. We thus evaluated the expression of SCF in HSC exposed *in vitro* for 48 hours to HSC-derived EVs or vehicle. While SCF expression was barely detectable in HSCs maintained in basal conditions (**Figures S7L**), it significantly increased upon

administration of EVs, corroborating the positive effect of HSC-derived EVs in supporting HSC function. Interestingly, EVs derived from committed progenitor (FKSL or Lin$^-$) cells or MSCs could not stimulate SCF expression.

(M) Quantitation of PKH26 signal transferred to HSC from EVs isolated from HSC, FKSL cells, Lin$^-$ cells, MSC or empty (Ø) and stained with PKH26 before administration to HSC (Ø, n = 499 cells; HSC, n = 380 cells; FKSL, n = 282 cells; Lin$^-$, n = 288 cells; 3 independent experiments).

(N) KSL cells were exposed to GW4869 or vehicle in the absence of stromal cells, and their serial-replating ability was determined. Colony counts (reported for each replating) were performed in independent littermate pairs (n = 3).

(O) Quantitation of particle concentration of EVs derived from FKSL cells after 2 weeks of culture in the presence or absence of Dox to induce shRNA for Rab27a, and obtained by qPCR (**-** Dox, n = 3; + Dox, n = 3). EV-enriched media was collected and processed for EVs isolation via polyethylene glycol and centrifugation.[89]

(**P** and **Q**) Short-term analysis of bone marrow reconstitution potential in HSCs with downregulation of Rab27a. (**P**) Percentages of donor-derived cells in various lineages of peripheral blood of recipient mice after Rab27a interfering. Isolated FKSL cells were infected with lentiviral particles carrying inducible shRNA for Rab27a. After 48 hours of culture in StemSpan® SFEM, cells were exposed to G418 for selecting cells integrating the plasmid. Surviving cells were then sorted and 2000 live FKSL cells were transplanted into lethally irradiated Ly5.1 recipient mice together with $1x10^6$ competitor BMMNCs. To induce shRNA expression, Doxycycline was supplemented in water starting at week 2 after BMT, supporting that shRab27a affects hematopoietic reconstitution stage. The hematopoiesis of the recipient mice was followed during

the first 21 days of Doxycycline supplementation (a total of 5 weeks after BMT). The x-axis represents days after Doxycycline administration. (+ Dox, n = 4 recipient; **-** Dox, n = 4 recipient). (**Q**) Percentages of donor-derived cells in the indicate fractions of the bone marrow of the recipient mice 23 days after Doxycycline administration (+ Dox, n = 4 recipient; **-** Dox, n = 4 recipient).

(R) Quantitation of PKH26 signal transferred to BM stromal cells from EVs isolated from HSC, FKSL cells, Lin^- cells or empty (Ø) and stained with PKH26 before administration to BM stromal cells (Ø, n = 55 cells; HSC, n = 1160 cells; FKSL, n = 1659 cells; Lin^-, n = 2187 cells; 3 independent experiments).

(S) Expression levels of SCF in BM stromal cells exposed to EVs isolated from HSC, FKSL cells, Lin^- cells or empty (Ø). Data were obtained by qPCR relative to *ActB* (Ø, n = 7 replicates; HSC, n = 11 replicates; FKSL, n = 6 replicates; Lin^-, n = 9 replicates).

(T) Long-term culture-initiating cell (LTC-IC) capacity of $CD34^-$ HSCs exposed to EV synthesis inhibitor GW4869 or vehicle (co-culture with OP-9 stromal cells, n ≥ 12 replicates, 4 independent experiments).

GEMM, Colony-forming unit-granulocyte, erythroid, macrophage, and megakaryocyte; GM, Colony-forming unit-granulocyte and macrophage; M, Colony-forming unit-macrophage; Dox, Doxycycline; eSRRF, enhanced Super-Resolution Radial Fluctuations; KSL, $Lin^-Sca\text{-}1^+c\text{-}Kit^+$ cells; FKSL, $CD135^-$ KSL cells; MSC, $CD45^-Ter119^-CD31^-Nestin^+$ mesenchymal stem cells. Bar graphs represent means ± SEM, circles represent each replicate. **(C)**, **(D)**, **(E)**, **(F)**, **(L)**, **(M)**, **(R)**, and **(S)**: one-way ANOVA with Dunnet multiple comparison test. **(H)**, **(J)**, **(K)**, **(O)**, and **(Q, left)**: Unpaired Student's T test. **(N)**, and **(Q, right)**: 2-way ANOVA with Sidak's multiple comparison

test. **(T)**: paired Student's t test. ****, $p < 0.0001$; **, $0.001 \leq p < 0.01$; *, $0.01 \leq p < 0.05$; N.S., not significant, $p > 0.05$.

Supplemental references

105. Ema, H., Takano, H., Sudo, K., and Nakauchi, H. (2000). In vitro self-renewal division of hematopoietic stem cells. J Exp Med *192*, 1281-1288. 10.1084/jem.192.9.1281.

106. Oedekoven, C.A., Belmonte, M., Bode, D., Hamey, F.K., Shepherd, M.S., Che, J.L.C., Boyd, G., McDonald, C., Belluschi, S., Diamanti, E., et al. (2021). Hematopoietic stem cells retain functional potential and molecular identity in hibernation cultures. Stem Cell Reports *16*, 1614-1628. 10.1016/j.stemcr.2021.04.002.